8-12-2014

"Coarse Grained" Bead Modeling of Macromolecules Transport in Free Solution and in a Gel

Hengfu Wu

“COARSE GRAINED" BEAD MODELING OF MACROMOLECULES TRANSPORT IN FREE SOLUTION AND IN A GEL

by

HENGFU WU

Under the Direction of Dr. Stuart Allison

ABSTRACT

The modeling of transport behavior of charged particles carried out in our laboratory is based on classical continuum electro kinetic theory. It is applied to a variety of systems from small electrolyte ions to macromolecules including peptides, DNA and nanoparticles. Systems range from weakly charged particles to highly charged ones. Transport properties studied include conductance, electrophoresis, and diffusion.

In this dissertation, the conductance of polyvalent electrolytes ions is studied both by a “small ion” model [R.M. Fuoss, L. Onsager, J. Phys. Chem. 61 (1957) 668] and “large ion”

model [R.W. O'Brien, L.R. White, J. Chem. Soc. Faraday Trans. 2 (74) (1978) 1607)]. Also, the coarse-grained continuum primitive model is developed and used to characterize the titration and electrical conductance behavior of aqueous solutions of fullerene hexa-malonic acid, which is a highly charged electrolyte with an absolute valence charge as high as 12.

Free solution electrophoresis is closely related to conductance and a coarse-grained bead modeling methodology, BMM, developed in the Allison's laboratory starting in 2006, is generalized to characterize peptide systems with respect to the charge, conformation, and possibly specific interactions with components of the BGE. For weakly charged peptides, the electrostatic potential is treated at the level of linear Poisson-Boltzmann equation, which predicts the electrophoretic mobility with considerable accuracy [S. Allison, H. Pei, U. Twahir, H. Wu, J. Sep. Sci., 2010, 33(16):2430-2438], but fails for highly charged systems. A new nonlinear Poisson-Boltzmann, NLPB-BM procedure is developed and applied to the free solution electrophoretic mobility of low molecular mass oligolysines. The difficulty of highly charged systems is twofold: more complex handeling of electrostatics and accounting for the relaxation effect. Both issues are addressed in this dissertation.

A related problem we investigated deals with the retarding influence of a gel on the rotational motion of a macromolecule. This is investigated within the framework of the Effective Medium (EM) model and is applied to examine the electric birefringence decay of a 622 base pair DNA fragment in an agarose gel. Modeling is also compared with experiment.

INDEX WORDS: Electrophoresis, Conductance, Diffusion, Coarse-Grained, Effective Medium, Relaxation Correction, Complex formation, Gel

“COARSE GRAINED" BEAD MODELING OF MACROMOLECULES TRANSPORT IN FREE SOLUTION AND IN A GEL

by

HENGFU WU

A Dissertation Submitted in Partial Fulfillment of the Requirements for the Degree of

Doctor of Philosophy

in the College of Arts and Sciences

Georgia State University

2014

"COARSE GRAINED" BEAD MODELING OF MACROMOLECULES TRANSPORT IN FREE SOLUTION AND IN A GEL

by

HENGFU WU

Committee Chair: Stuart Allison

Committee: Donald Hamelberg

Jenny Yang

Electronic Version Approved:

Office of Graduate Studies

College of Arts and Sciences

Georgia State University

August 2014

DEDICATION

To my wife, my parents, and my sister

ACKNOWLEDGEMENTS

The work described in this Dissertation has been accomplished with the assistance and support of many people. First and foremost, I would like to express my sincere appreciation and gratitude to my advisor, Dr. Stuart Allison. He taught me how to start academic pursuits from the very beginning. From him I have learned a lot, particulary in the area of Computational Chemistry. Without his encouragement and help, I could not have completed my PhD work.

I would also like to thank my committee members: Dr. Donald Hamelberg, and Dr. Jenny Yang for their helpful advice on my Dissertation, and I would also like to thank Dr. Dabney White Dixon for her great concern for me and her help to me all the time.

I would like to thank the Department of Chemistry at Georgia State University for offering me the opportunity to pursue the Ph.D. degree, for offering great classes and the opportunity to teach undergraduate students in laboratories and tutorials. All of these provided me good training in academic matters. Specially, I would like to thank Dr. Stuart Allison, Dr. Markus Germann, Dr. David Wilson, Dr. Jerry Smith, Dr. Dabney Dixon, Dr. Kathryn Grant, Dr. Jenny Yang, Dr. Donald Hamelberg, Dr. Ivaylo Nikolaev Ivanov and Dr. Aimin Liu for their interesting classes. I would also like to thank my previous group members, Hongxia Pei, Umar Twahir, and other group members, and my friends for discussions and help. Last but not least, I would like to express my gratitude to my family. Thanks to my parents' great love and support and my sister, Sheling Hao's encouragement all the time. Special thanks go to my wife, Kun Tang, for her love and companionship. She has always taken good care of me.

TABLE OF CONTENTS

LIST OF TABLES

LIST OF FIGURES

CHAPTER 1

INTRODUCTION

1.1 Brief Introduction of Electrophoresis

Charged particles, under the influence of electric fields, migrate toward the electrode with the opposite charge, and this phenomena is called electrophoresis. Electrophoretic mobility depends on particle size and charge, or the ratio of charge over size. The higher the ratio, the faster the particle moves subjected to the same electric field for a period of time. Particles of different size and charge travel different distances. Electrophoretic techniques have been widely used in chemistry, molecular biology, microbiology, and colloid science, etc. Macromolecules, like proteins, peptides and nucleocapsids, as well as small molecules, like amino acid, nucleotides, and organic ions can migrate in an electric field. The simplest possible case is illustrated in Figure 1-1. When immersed in a neutral solvent of viscosity, η, applied electric field of strength E, a spherical particles of charge +Q, and radius a, migrates at a constant velocity due to the influence of two forces.

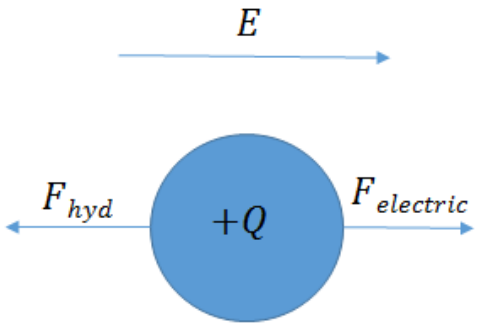

Figure 1-1: A spherical charged particle in free solution with applied electric field

$F_{eletric}$ is the electrical force acting on the charged particles due to the electric field, and F_{hdy} is the hydrodynamic force acting on the particle due to the surrounding viscous solvent. The magnitude of the forces can be written

$$F_{eletric} = QE \qquad (1-1)$$

$$F_{hyd} = 6\pi\eta a v \qquad (1-2)$$

Where v is the particle moving velocity, Q is the effective charge of particle, E is the electric field strength, η is the solution viscosity, and a is the hydrodynamic radius of particle.

Under steady state, both forces equal to each other,

$$QE = 6\pi\eta a v \qquad (1-3)$$

Rearrange equation (1-3) to derive the electrophoretic mobility, μ

$$\mu = \frac{v}{E} = \frac{Q}{6\pi\eta a} \qquad (1-4)$$

The main problem of electrophoresis theory is to determine both forces for model systems, which, however, are not as simple as a spherical particles in the idealized system described above. In actual cases, the presence of the background electrolyte ions affects the migration of "guest" particles. As shown in Figure 1-2, an irregular shaped particle migrates in a free solution with applied electric field, E, and the other ions of the background electrolyte must be accounted for.

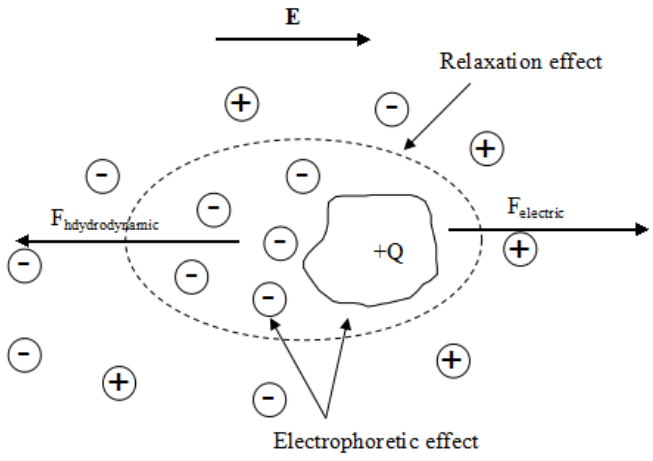

Figure 1-2: An irregular shaped charged particle in neutral solution surrounded by electrolyte ions in the presence of electric field

For the case shown in Figure 1-2, the positively charged particle is surrounded by negatively charged electrolyte ions, which form an ion atmosphere, called double layer around the "guest" particle. Under the influence of an electric field, positively charged ions move toward the cathode, and negative ions toward the anode. During the migration, the counter ions, which migrate in the opposite direction from the guest ion, cause a hydrodynamic drag force to act on the guest particle, slowing down its motion. This effect is called the "electrophoretic effect". Also, the surrounding ion atmosphere is distorted under the influence of an external electric field, which gives rise to another force on the guest particle. This effect is called the "relaxation effect". The "relaxation effect" can be ignored for weakly charged particles, but becomes significant for highly charged particles. Both effects slow down the migration of particles, and make the theoretical treatment of electrophoresis complicated and difficult.

1.2 The Modeling Methodologies of the Transport of Charged Particles

One of the early successes of atomic scale continuum transport modeling concerned the electrical conductance of dilute solutions of strong electrolytes [1-3]. It is based on equilibrium theory of strong electrolytes by Debye and Huckel [4], and the electrolyte ions were modeled as point charges, and then extended to account for the finite size of the ions, and also for higher electrolyte concentrations [5-7]. It was subsequently extended to general electrolyte solutions with an arbitrary number of ions of arbitrary valence [8]. Such an approach is collectively called the "small ion" model. Despite the successes of the "small ion" model, few applications were made to electrolyte solutions containing polyvalent ions or mixtures of electrolytes containing more complex ionic species. One shortcoming of the "small ion" model is that electrostatics are treated at the level of linear Poisson-Boltzmann equation, and this makes it applicable to only weakly charged particles. The Allison group has applied the "small ion" model to a number of

binary electrolytes and also polyvalent salts for which experimental conductance data is available. This is the subject of Chapter 2.

A transport phenomenon closely related to electrical conductivity is the free solution electrophoretic mobility. Free solution electrophoresis and related techniques play a vital role in separation and characterization of peptides as discussed in a number of reviews [9-14]. Understanding the electrophoresis at the fundamental level of continuum electrodynamics and hydrodynamics can provide information about peptide charge and possibly conformation [13-20]. The peptide mobility in the limit of low concentration is influenced by a variety of factors, including the composition of BGE, temperature, solvent viscosity, and pH. These factors are critical in defining optimal experimental conditions for separation. Generally, two different approaches have emerged in modeling peptide mobility, μ. The first is based on the work of Offord [22], which is semi empirical.The mobility is written [9-13, 17-19, 21,23]

$$\mu \cong \frac{c_1 Z}{M^{\alpha}} \qquad (1-5)$$

or

$$\frac{c_2 \log(Z + c_3)}{M^{\alpha}} \qquad (1-6)$$

Where, Z is the effective peptide charge, M the molecular mass, c_1, c_2, c_3 and α are empirical constants, depending on solvent, temperature, and BGE. However, these models fail for highly charged or hydrophobic peptides [21]. The second approach is grounded on continuum electro hydrodynamic theory, which has its origin in the electrophoresis and conductivity of spherical ions [3, 5, 24-30]. This continuum theory accounts in more detail for the distribution of the peptide charge and its primary and secondary structure [21, 31, 32]. It enables the investigator to quantitatively predict mobility once solvent, temperature, BGE, particle size,

shape and charge are defined. Continuum theory has also been applied to long [33] and finite [34] rods, axi-symmetric ellipsoids [35-37] and rigid particles of arbitrary shape and charge distribution [38-40]. To deal with the problem of flexible structures, a bead modeling methodology (BMM) has been developed and applied to peptides [41-45]

Until recently, the applications were largely restricted to weakly charged peptides, such as oligoglycines [42]. By "weakly charged", we mean the absolute surface or "ζ" potential does not exceed about 25 mV [46], or equivalently, the electrophoretic mobility does not exceed approximately 0.20 ($cm^2/(kV\ s)$) [47]. For large or highly charged particles, a "large ion" model, grounded on very similar continuum electro-hydrodynamic principles, is relevant since it accounts for the "relaxation effect" [26-30, 48]. The "relaxation effect" becomes significant for highly chared particles including pepetides and it is essential to accurately account for its influence on electrophoretic mobility. Careful accounting of the relaxation effect greatly improves agreement between modeling and experiment, as illustrated in Chapter 4.

1.3: Outline of the Dissertation

In this Dissertation, the transport behavior of small binary electrolytes ions, DNA molecules, highly charged peptides, and nanoparticles are modeled based on classic electro kinetic theory. The effects from BGE, pH, and temperature on the electrophoretic mobility are examined. Chapter 2 examines the equivalent conductance of binary electrolytes with two complimentary continuum theories of electro kinetic transport. The main objective is to bridge the gap between the "small ion" and "large ion" models by modifying the O'Brien and White ("large particle" model) procedure. In Chapter 3, the retarding influence of a gel on the rotational motion of a macromolecules is investigated within the framework of the Effective Medium (EM) model, which is compared with rotational diffusion in agarose gel measured by electric

birefringence. This chapter does not involve the electrokinetics, but the closely related problem of continuum hydrodynamics. In chapter 4, bead modeling methodology is generalized to treat electrostatic at the level of the nonlinear Poisson-Boltzmann equation, which makes it more applicable to the important class of highly charged macroions and highly charged peptides in particular. In chapter 5, the "coarse-grained" continuum primitive model is developed and used to characterize the titration and electric conductance behavior of aqueous solutions of fullerene hexa malonic acid, FHMA. This involves numerical solution of the non-linear Poisson-Boltzmann equation for all possible charge states of the "host" model FHMA particle.

CHAPTER 2

CONDUCTIVITY AND ELECTROPHORETIC MOBILITY OF DILUTE IONIC SOLUTIONS

2.1 Introduction

One of the early successes of atomic scale continuum transport modeling concerned the electrical conductance of dilute solutions of strong electrolytes [1-3]. This work, in turn, was grounded on equilibrium theory of strong electrolytes by Debye and Huckel [4]. The early theory, which was restricted to very dilute solutions of ions modeled as point charges, was subsequently extended to account for the finite size of the ions and also higher electrolyte concentrations [5-7]. For monovalent binary aqueous electrolyte solutions up to a concentration of about 0.10 mol/dm^3 or M, experimental and model equivalent conductance are in excellent agreement [5-7] for reasonable choices of model parameters. Refs. [5-7] are restricted to binary electrolytes. This was subsequently extended to general electrolyte solutions made up of an arbitrary number of ions of arbitrary valence [8]. In the present work, this approach shall collectively be called the ‘‘small ion” model. Despite the successes of the ‘‘small ion” model, there have been few attempts to apply it directly to electrolyte solutions containing polyvalent ions or mixtures of electrolytes containing more complex ionic species. One of its shortcomings is that electrostatics are treated at the level of the linear Poisson– Boltzmann equation which limits it to weakly charged particles. The theory has been generalized to go beyond the use of the linear Poisson–Boltzmann equation in representing the ionic potential of mean force [49,50].

A transport phenomenon closely related to electrical conductivity is the free solution electrophoretic mobility. In recent years, capillary zone electrophoresis [9–14] has become a widely used separation technique for a broad array of ionic species including peptides [19-21，

51-53], organic anions [54, 55], proteins [40, 56, 57], and nanoparticles [58, 58]. Although the conductance theories discussed in the previous paragraph [3,5–7] have been applied to mobility studies of small and weakly charged ions [54, 55, 60, 61], they are not appropriate for large or highly charged particles including nanoparticles [58, 59] or metal oxide colloidal particles [62]. For large and/or highly charged particles, there is a long established alternative that is grounded on very similar continuum electro-hydrodynamic principles, but has its origin in the electrophoresis of large colloidal particles [26-30, 48]. In this work, it shall be called the ‘‘large ion” model. Of particular relevance to the ‘‘large ion” model is the numerical procedure of O’Brien and White [30] that has come into widespread use and can be applied to the electrophoresis of a spherical particle of arbitrary size containing a centrosymmetric charge distribution of arbitrary net charge. One factor that may limit the application of the ‘‘large ion” model to treat the mobility or conductivity of small ions is that it ignores the Brownian motion of the ion of interest. This may only be a reasonable approximation if the ion of interest is much larger than the ions comprising the surrounding electrolyte. The ‘‘small ion” model, on the other hand does account for the Brownian motion of all ions present [3, 5-8, 49, 50].

The principle objective of the present work is to bridge the gap between the ‘‘small ion” and ‘‘large ion” models discussed above by applying both to the conductivity of a number of binary electrolytes for which experimental conductance data is available. Polyvalent salts shall also be considered in order to test the models under conditions of larger ‘‘zeta” potential. In the course of this work, it has been necessary to modify the O’Brien and White (‘‘large particle” model) procedure in three ways. The first is to include an ‘‘ion free” layer of solvent just outside the surface of hydrodynamic shear. In addition to the distance of hydrodynamic shear from the center of ion j, a_j, an ion exclusion distance, a_{ex}, is also defined. The second modification

concerns hydrodynamic boundary conditions. In both ‘‘small ion” and ‘‘large ion” models, hydrodynamic boundary conditions have been handled somewhat differently and it is important to consider how this influences the results. Currently, ‘‘stick” boundary conditions are employed in the ‘‘large ion” model, and this means the particle velocity and fluid velocity match at the surface of hydrodynamic shear. In addition to the conventional ‘‘stick” hydrodynamic boundary conditions, we also consider ‘‘slip”. As shall be shown, both ‘‘stick” and ‘‘slip” models are capable of explaining the experimental conductance data equally well for about the same a_{ex} values, but different a_j values must be chosen on the basis of limiting ionic conductivities. Third, although the ‘‘large ion” model does not account explicitly for the Brownian motion of the central ion of interest, we present a simple way of doing so that involves adding a correction term to the mobile ion mobilities. When this is done, the ‘‘small ion” and ‘‘large ion” model conductivities with the same or similar model parameters are comparable with each other and yield excellent agreement with experiment.

2.1 Modeling

2.2.1 Conductance and Mobility of Small Ion Electrolytes

The original Onsager [2] and Onsager–Fuoss [3] theory treats the equivalent conductivity, Λ, or electrophoretic mobility of ionic species j, of dilute strong electrolyte;

$$\Lambda_p = \Lambda_0 - (\alpha\Lambda_0 + \beta)\sqrt{m_0} \qquad (2-1)$$

In Eq. (2-1), the ‘‘p” subscript denotes the original Onsager–Fuoss model mobility, Λ_0 is the equivalent conductance of the solution in limit of zero ionic strength, α is the ‘‘relaxation coefficient”, β is the ‘‘electrophoresis coefficient”, and m_0 would be the concentration of

electrolyte in moles/dm^3 or M if it did not dissociate into ions. The physical basis of α is ion relaxation, the distortion of the ion atmosphere around a particular ion from equilibrium due to the imposition of an electric and/or flow field. The physical basis of β is the additional hydrodynamic backflow produced in the vicinity of a particular ion produced by the presence of nearby ions. The coefficients α and β depend on: temperature, T, the properties of the solvent including relative dielectric constant, ε_r, and viscosity, η, and the valence charges of the ionic species present in solution, $\{z_j\}$. They are, however, independent of ionic size. Ionic size, however, does enter through Λ_0 or equivalently, the electrophoretic mobility of individual ions in the limit of zero ionic strength, I. Underlying Eq. (2-1) is a model in which the ions are treated as point charges. The Onsager–Fuoss, OF, theory [2,3] starts with a general equation of continuity which specifies the concentration of ions of one species in the vicinity of ions of other species in an electrolyte solution which has reached a steady state under the influence of a weak, constant external electric field, $\underline{e}_0$. Account is taken of the Brownian motion of the various ionic species of which an arbitrary number may be present. Electrostatics are treated at the level of the linear Poisson–Boltzmann equation. This is true not only for the ‘‘point ion” model discussed here, but the more general finite ion case considered at the end of this section. For the ‘‘point ion” model, the boundary conditions on the fluid velocity are that it remain finite at the center of an ion and vanish, on average, at a large distance away from it. The general OF mobility expression of an ionic species can be written [3]

$$\mu_j = \mu_{j0} - \left(B_1 z_j \mu_{j0} \sum_{n=0}^{\infty} c_n r_j^{(n)} + B_2 z_j \right) \sqrt{I} \qquad (2-2)$$

Where I is the ionic strength of the electrolyte, c_n and $r_j^{(n)}$ discussed below,

$$B_1 = \frac{\sqrt{2}F^3}{12\pi N_{AV}}(\varepsilon_0\varepsilon_r RT)^{-3/2} = \frac{2.806\times10^6}{(\varepsilon_r T)^{3/2}}(M^{-1/2}) \qquad (2-3)$$

$$B_2 = \frac{\sqrt{2}F^2}{6\pi\eta N_{AV}}(\varepsilon_0\varepsilon_r RT)^{-1/2} = \frac{4.275\times10^{-6}}{\eta(\varepsilon_r T)^{1/2}}(\frac{m^2}{V\sec M^{1/2}}) \qquad (2-4)$$

In the present work, SI units shall be followed for the most part, but g in Eq. (2-4) is in centipoise and I is in moles/ dm^3 = M. For the remaining terms, F is the Faraday constant (=9.645 *10^4 C/mole), N_{Av} is Avogadro number, ε_0 is the permittivity of free space, R is the gas constant, and other quantities (except for c_n and $r_j^{(n)}$) have been described in the previous paragraph. Also, the physical basis of the B_1 term in Eq. (2-2) is ion relaxation and the physical basis of the B_2 term is the electrophoretic effect.

Consider a single strong electrolyte, A_aB_b or binary electrolyte, that undergoes complete dissociation according to

$$A_aB_b \rightarrow aA^{z_+} + bB^{z_-} \qquad (2-5)$$

Where a and b, z_+ and z_- are stoichiometries and valences of the two ions. If m_0 is the initial concentration of undissociated electrolyte, then the condition of electrical neutrality requires

$$am_0z_+ + bm_0z_- = 0 \qquad (2-6)$$

And

$$I = \frac{m_0}{2}(az_+^2 + bz_-^2) = (\frac{az_+}{2}(z_+ - z_-))m_0 = \phi^2 m_0 \qquad (2-7)$$

The conductivity, Λ, of a solution of this strong electrolyte can be written

$$K = am_0\lambda_+ + bm_0\lambda_- = am_0 \mid z_+ \mid \Lambda_+ + bm_0 \mid z_- \mid \Lambda_-$$
$$= am_0 Fz_+\mu_+ + bm_0 Fz_-\mu_- = am_0 Fz_+ \mid \mu_+ - \mu_- \mid = am_0 z_+ \Lambda \qquad (2-8)$$

The λ_j terms appearing in the first equality on the right hand side of Eq. (2-8) are molar conductivities of specific ions. The Λ_j values appearing in the second equality on the right hand side of Eq. (2-8) correspond to equivalent conductivities of specific ions. Most, but not all, of the specific ion conductivities reported in the modern literature and in handbooks are Λ_j's and in SI units are in S m^2/mole or m^2/ (ohm mole). The third equality follows from the relationship between equivalent ionic conductance and ion mobility, which will be positive for + ions and negative for - ions, $\Lambda_j = F \mid \mu_j \mid$. The fourth equality follows from the electro neutrality condition, Eq. (2-6). The fifth equality gives the equivalent conductance of the binary electrolyte, Λ. Dividing various equalities on the right hand side of Eq. (2-8) by $am_0 z_+$ gives

$$\Lambda = \Lambda_+ + \Lambda_- = F(\mu_+ - \mu_-) = F(\mid \mu_+ \mid + \mid \mu_- \mid) \qquad (2-9)$$

For a strong binary electrolyte of the form A_aB_b, the ‘‘relaxation” term in Eq. (2-2) according to the OF theory can be written (3)

$$S_j \equiv z_j \sum_{n=0}^{\infty} c_n r_j^{(n)} = \frac{\mid z_+ z_- \mid q}{1+\sqrt{q}} \qquad (2-20)$$

$$q = \left(\frac{\mid z_+ z_- \mid}{\mid z_+ \mid + \mid z_- \mid}\right)\left(\frac{\mid \mu_{+0} \mid + \mid \mu_{-0} \mid}{\mid z_-\mu_{+0} \mid + \mid z_+\mu_{-0} \mid}\right)$$
$$= \left(\frac{\mid z_+ z_- \mid}{\mid z_+ \mid + \mid z_- \mid}\right)\left(\frac{\Lambda_{+0} + \Lambda_{-0}}{\mid z_- \mid \Lambda_{+0} + \mid z_+ \mid \Lambda_{-0}}\right) \qquad (2-11)$$

If the binary electrolyte is also a symmetric electrolyte ($|z_+| = |z_-|$), then q = 1/2. Using Eqs. (2-2), (2-7), and (2-10) in (2-9), we have for a general binary electrolyte

$$\Lambda = \Lambda_0 - [B_1(\Lambda_{+0}S_+ + \Lambda_{-0}S_-) + B_3(|z_+| + |z_-|)]\phi\sqrt{m_0} \qquad (2-12)$$

$$\Lambda_0 = \Lambda_{+0} + \Lambda_{-0} \qquad (2-13)$$

$$B_3 = FB_2 = \frac{0.4125}{\eta(\varepsilon_r T)^{1/2}}\left(\frac{m^2}{ohm\,mole\,M^{1/2}}\right) \qquad (2-14)$$

It should be emphasized that g in Eq. (2-14) is in centipoise. Comparing Eqs. (2-12) with (2-1), and equating Λ with Λ_p, we can now identify the relaxation and electrophoresis coefficients,

$$\alpha = \frac{B_1(\Lambda_{+0}S_+ + \Lambda_{-0}S_-)\phi}{\Lambda_0} \qquad (2-15)$$

$$\beta = B_3(|z_+| + |z_-|)\phi \qquad (2-16)$$

The expression for α simplifies further within the framework of the OF theory. From Eq. (2-10) we have $S_+ = S_- = S$ and Eq. (2-15) then reduces to

$$\alpha = \beta S\phi \qquad (2-17)$$

In order to make contact with different relaxation theories, however, we have chosen to distinguish the relaxation terms for the different ions, S_j, defined by Eq. (2-10).

For an electrolyte consisting of more than two ionic species, the relaxation effect is more complex than discussed in the previous paragraph, which is strictly valid only for a binary electrolyte. The OF theory can also be applied to ionic solutions containing an arbitrary number

of distinct ions. Assume we have N ions present and let m_j denote the concentration (in M) of species j. For this more general case, the S_j terms are given by the first equality on the right hand side of Eq. (2-10). We have [3]

$$c_0 = (2-\sqrt{2})/2 = 0.2928932 \qquad (2-18)$$

$$c_1 = -0.3535534 \qquad (2-19)$$

$$c_n = c_{n-1}(\frac{3}{2n}-1)\ (n>1) \qquad (2-20)$$

$$\underline{r}^{(n)} = (2\underline{\underline{H}} - \underline{\underline{I}})\cdot \underline{r}^{(n-1)} \qquad (2-21)$$

$$(r^{(0)})_j = r_j^{(0)} = z_j - (\frac{\sum_{k=1}^{N} u_k z_k}{\sum_{k=1}^{N} u_k / w_k})(\frac{1}{w_j}) \qquad (2-22)$$

$$u_j = \frac{m_j z_j^2}{\sum_{k=1}^{N} m_k z_k^2} \qquad (2-23)$$

$$w_j = \Lambda_{j0} / |z_j| \qquad (2-24)$$

$$H_{ij} = \delta_{ij}(\sum_{k=1}^{N} \frac{u_k w_k}{w_i + w_k}) + \frac{u_j w_j}{w_i + w_j} \qquad (2-25)$$

In Eq. (2-21), $\underline{r}^{(0)}$ is a N by 1 column vector and $\underline{\underline{H}}$ and $\underline{\underline{I}}$ are N by N matrices. Also, $\underline{\underline{I}}$ is the identity matrix and d_{ij} is the Kronecker delta. In general, it is necessary to solve for S_j iteratively. One begins by determining $\underline{r}^{(0)}$ from Eq. (2-22) and known input parameters. The same input parameters are used to determine the components of $\underline{\underline{H}}$. Then Eq. (2-21) is used to generate $\underline{r}^{(n)}$ for higher order terms in n. These along with c_n defined by Eqs. (2-18) - (2-20) are used in Eq. (2-10) to compute S_j. In most cases, the series converges rapidly with n. Despite its apparent complexity, this procedure is actually quite simple and straightforward to implement in a computer program or an Excel spreadsheet, which will be shared with interested investigators upon request to the corresponding author. In terms of the dimensionless relaxation terms, S_j, generated by the above procedure, Eq. (2-2) can be written

$$\mu_j = \mu_{j0} - (B_1 \mu_{j0} S_j + B_2 z_j)\sqrt{I} \qquad (2-26)$$

In the 1950s, Fuoss and Onsager generalized this theory to extend its range of validity to terms of order in m_0^1 electrolyte concentration and also account, to lowest order, for the finite sizes of the ions [6,7]. This work was restricted to binary electrolytes and specific applications in this and subsequent work [63-65] were further restricted to monovalent (binary) electrolytes. Quint and Vaillard [8] did generalize this to an arbitrary electrolyte and included terms to order $m_0^{3/2}$ although some contributions at the level of $m_0^{3/2}$ are missing [66]. In these studies [6–8, 63–66] a single ion exclusion distance, a_{ex}, is defined and the assumption is made that the center-to-center distance, r, between any two ions cannot be smaller than a_{ex}. The assumption is also made that the normal component of the relative fluid velocity vanishes at $r = a_{ex}$ (see Eq. (2-3, 2-4) of (2-7)). Closely related work was also carried out by Pitts [5] on symmetric binary electrolytes, but the assumption was made that the relative fluid velocity as a whole, and not just the normal component, vanishes at $r = a_{ex}$. Within the framework of the more general Fuoss–Onsager theory [6, 7], the equivalent conductance of a binary electrolyte can be written

$$\Lambda = \Lambda_{nr}(1-\xi) \qquad (2-27)$$

$$\Lambda_{nr} = \Lambda_0 - \beta\sqrt{m_0}\,/(1+\kappa\alpha_{ex}) \qquad (2-28)$$

$$\kappa = \mathrm{B}\phi\sqrt{m_0} \qquad (2-29)$$

$$\mathrm{B} = \frac{\sqrt{2}F}{\sqrt{\varepsilon_0 \varepsilon_r RT}} = \frac{5.028\times10^{11}}{\sqrt{\varepsilon_r T}}\frac{1}{\mathrm{M}^{1/2}m} \qquad (2-30)$$

$$\xi = \alpha\sqrt{m_0}(1-\Delta_1+\Delta_2)+\frac{\beta\Delta_3^{'}}{\Lambda_0}\sqrt{m_0} \qquad (2-31)$$

The term Λ_{nr} is the equivalent conductance in the absence of ion relaxation, n denotes the relaxation correction, and j is the Debye–Huckel screening parameter. In Eq. (2-31), the terms Δ_1, Δ_2, and $\Delta_3^{'}$ represent higher order correction terms and depend on concentration to leading order $m_0^{1/2}$. Explicit expressions are given in Section 7 of Ref. [7] specific to symmetric binary electrolytes. More general expressions (making minor corrections for sign errors) can be deduced from equations in Section 6 of Ref. [7] for general binary electrolytes. In subsequent work by Fuoss and coworkers, additional corrections were made to Δ_2, and $\Delta_3^{'}$ [63-65, 67]. However, these changes were minor and do not alter the relaxation corrections significantly. In addition, expressions not limited to binary electrolytes can be found in references [8, 66] and include terms to order $m_0^{3/2}$. Since the 1957 paper by Fuoss and Onsager [7] carries out the most thorough comparison between theoretical and experimental conductance and subsequent applications are mostly restricted to monovalent binary electrolytes, we shall use the equations from the 1957 paper [7] in the present work when considering the ‘‘small ion” model. The ‘‘small ion” theory pioneered by Fuoss and Onsager [2, 3] remains in widespread use to this day not only for fully dissociated electrolytes, but undissociated electrolytes as well [68]. With few exceptions [66], the over-whelming majority of applications involve symmetric binary electrolytes [68-70]. The limiting assumptions of the ‘‘small ion” theory are: (1) solvent and mobile ions are treated as a continuum, (2) electrostatics are described by the linear Poisson–Boltzmann equation, (3) a single ion exclusion distance, a_{ex}, is included in modeling, (4) κa_{ex} is small (small ion sizes and low electrolyte concentration). In addition to Eq. (2-27), we shall also

consider a simpler model that includes finite ion size effects in Λ_{nr} as given by Eq. (2-28), but restricts the relaxation term to $m_0^{1/2}$ and this allows us to ignore Δ_1, Δ_2, and $\Delta_3^{'}$ altogether. Define

$$\Lambda_1 = \Lambda_{nr}(1-\alpha\sqrt{m_0}) \qquad (2-32)$$

As demonstrated in the main body of this work, Eq. (2-32) works almost as well as Eq. (2-27) for binary electrolytes for $m_0 \leq 0.005$ M.

Finally, consider the ion electrophoretic mobilities within the framework of the Onsager-Fuoss theory restricted to a binary electrolyte. We can write

$$\mu_j = \mu_{j,nr}(1-\xi_j) \qquad (2-33)$$

$$\mu_{j,nr} = \mu_{j0} - \mathrm{B}_2 \mathrm{Z}_j \phi\sqrt{m_0}\,/(1+\kappa\alpha_{ex}) \qquad (2-34)$$

Where ξ_j is the same for both ions and the j subscript is omitted in Eq. (2-27) and (2-31). As Eq. (2-31) shows, higher order concentration effects (via the Δ_1, Δ_2, and $\Delta_3^{'}$ terms) can be accounted for in binary electrolytes. However, it would be useful if we could also consider ternary and higher order electrolyte solutions. This would be relevant if we were interested in the mobility of a ‘‘guest” ion in the presence of a binary electrolyte, for example. Eq. (2-26) makes it possible to consider such cases, where the relaxation term depends on the particular ion and we can write

$$\xi \cong \mathrm{B}_1 S_j \sqrt{\mathrm{I}} \qquad (2-35)$$

$$\mathrm{I} = \frac{1}{2}\sum_{\kappa} m_\kappa z_\kappa^2 \qquad (2-36)$$

Where S_j is given by the first term on the right hand side of Eq. (2-10) and the sum in Eq. (2-36) extends over all ions present in solution. For ternary and higher order electrolyte solutions, we can approximate n_j appearing in Eq. (2-33) with Eq. (2-35). This is equivalent to ignoring terms higher than order $I^{1/2}$ in the relaxation correction. The same approximation is made in arriving at Eq. (2-32) for the conductivity of a binary electrolyte and Eq. (2-32) therefore gives us a way of determining how accurate this approximation is in specific cases.

2.2.2 Mobility of Large Spherical Ions

It shall be assumed that our model particle is spherical and contains a centrosymmetric charge distribution within a surface of hydrodynamic shear located at a distance r = a from the center of the particle. At the shear surface, ‘‘stick” or ‘‘slip” boundary conditions may prevail. In the case of ‘‘stick”, it is assumed that fluid and particle velocities match at r = a. In the case of ‘‘slip” boundary conditions, it is assumed that only the outward normal component, $\underline{n}$, of particle and fluid velocities match at r = a. Also, if $\underline{\underline{\sigma_H}}$ denotes the hydrodynamic stress tensor of the fluid, then $\underline{\underline{\sigma_H}}$ is parallel to $\underline{n}$ at the shear surface [71, 72]. Outside of the shear surface, the fluid is treated as a hydrodynamic continuum that obeys the linearized Navier–Stokes and solvent incompressibility equations.

$$\eta\nabla^2\underline{v} - \underline{\nabla}\rho = \underline{\nabla}\cdot\underline{\underline{\sigma}}_{\mathrm{H}} = -\underline{s} \qquad (2-37)$$

$$\underline{\nabla}\cdot\underline{v} = 0 \qquad (2-38)$$

Where g is the fluid viscosity, $\underline{v}$ is the local fluid velocity, p is the local fluid pressure, and $\underline{s}$ is the local external force/volume on the fluid. If we had an uncharged particle ($\underline{s} = \underline{0}$)

translating with velocity $\underline{u}^*$ through a fluid that is at rest far from the particle, the solution of Eqs. (2-37) and (2-38) for the fluid velocity, $\underline{v}^0(\underline{r})$ can be written for r > a,

$$\underline{v}^0(\underline{r}) = \underline{\underline{T}}(\alpha, \underline{r}) \cdot \underline{u}^* \qquad (2-39)$$

Where for ‘‘stick” boundary conditions, the tensor, $\underline{\underline{T}}(a, \underline{r})$ is [74]

$$\underline{\underline{T}}(\alpha, \underline{r}) = \frac{3\alpha}{4r}(\underline{\underline{I}} + \underline{\underline{nn}}) + \frac{\alpha^3}{4r^3}(\underline{\underline{I}} - 3\underline{\underline{nn}}) \qquad (2-40)$$

$$\underline{\underline{nn}} = \underline{\underline{rr}} / r^2 \qquad (2-41)$$

And for "slip" boundary conditions,

$$\underline{\underline{T}}(a, \underline{r}) = \frac{a}{2r}(\underline{\underline{I}} + \underline{\underline{nn}}) \qquad (2-42)$$

In Eqs. (2-40) and (2-42), $\underline{\underline{I}}$ denotes the 3 by 3 identity matrix. The zero superscript on $\underline{v}^0$ is a reminder that this refers to the special case of an uncharged spherical particle.

Extending from r = a to r = a_{ex}, where a_{ex} is the ion exclusion distance, it is assumed that no ions are present. In this region of the fluid adjacent to the particle, $\underline{s} = \underline{0}$. The fluid, however, obeys Eqs. (2-37) and (2-38). For r > a_{ex}, the ion atmosphere is treated as a continuum. Let $n_j(\underline{r})$ denote the local concentration of mobile ion species j in M and let z_j denote the valence charge of a single ion. The charge distribution, $\rho(\underline{r})$, obeys the Poisson equation in general,

$$\underline{\nabla} \cdot (\varepsilon(\underline{r}) \underline{\nabla} \Psi(\underline{r})) = -\rho(\underline{r}) / \varepsilon_0 \qquad (2-43)$$

$$\rho(\underline{r}) = \rho_f(\underline{r}) + F\sum_J z_j n_j(\underline{r}) \qquad (2-44)$$

where ε_0 is the permittivity of free space, ε is the local relative dielectric constant, Ψ is the electrodynamics potential, ρ_f is the fixed charge density (within the particle) and the sum in Eq. (2-44) extends over all mobile ion species present. If it is assumed $\varepsilon(\underline{r}) = \varepsilon_i$ for r $< a$ and $\varepsilon(\underline{r}) = \varepsilon_r$ for r $> a$, we also have the boundary condition

$$\varepsilon_i\left(\frac{\partial\psi}{\partial r}\right)_{r=\alpha_-} = \varepsilon_r\left(\frac{\partial\psi}{\partial r}\right)_{r=\alpha_+} \qquad (2-45)$$

Where $a_{\pm}$ denotes a point just outside or inside the particle surface. To proceed, we use the notation and many of the protocols of O'Brien and White [30]. Due to the presence of a constant external electric, $\underline{e_0}$, or flow field, the steady state electrodynamics potential is written

$$\psi(\underline{r}) = \psi_0(\underline{r}) + \psi_1(\underline{r}) - \underline{e_0}\cdot\underline{r} \qquad (2-46)$$

Where Ψ_0 is the local equilibrium electrostatic potential and Ψ_1 is a perturbation potential that vanishes far from the particle. The local ion densities are also perturbed from their equilibrium values, $n_{j0}(\underline{r})$, which are related to a new potential, $\phi_j(\underline{r})$, defined by

$$n_j(\underline{r}) = n_{j0}(\underline{r})e^{-ez_j(\phi_j(\underline{r})+\psi_1(\underline{r}))/\kappa_B T} \cong n_{j0}(\underline{r})\left[1 - ez_j(\phi_j(\underline{r})+\psi_1(\underline{r}))/k_B T\right] \qquad (2-47)$$

$$n_{jo}(\underline{r}) = m_j e^{-z_j y_0(\underline{r})} \qquad (2-48)$$

$$y_0(\underline{r}) = \frac{e\psi_0(\underline{r})}{k_B T} \qquad (2-49)$$

Where k_B is the Boltzmann constant. It is assumed that the perturbing electric or flow field is sufficiently small that only terms to first order in those perturbing fields are significant. This justifies the expansion of the exponential in Eq. (2-47). In addition to Eqs. (2-37), (2-38), and (2-43), an ion

$$\underline{\nabla} \cdot \underline{J}_j = 0 \qquad (2-50)$$

$$\underline{J}_j = n_{j0}\underline{\nu} + Fz_j n_{j0} D_j \left(\underline{\nabla}\Phi_j + \underline{e_0}\right) \Big/ R\mathrm{T} \qquad (2-51)$$

Above, $\underline{J}_j$ is the local current density of species j and D_j is the translational diffusion constant. Other quantities have been defined previously. The boundary condition on j arises as a result of the constraint that mobile ions cannot approach the particle closer than a distance a_{ex}. Setting $\underline{J}_j \cdot \underline{n} = 0$ in Eq. (2-51) then yields

$$\left(\frac{\partial \Phi_j(\underline{r})}{\partial r}\right)_{r=\alpha_{ex}} = -\underline{e_0} \cdot \underline{n} \qquad (2-52)$$

For a spherical particle, the solution of the equilibrium electrostatic potential is a special case of Eq. (2-43). The reduced potential depends only on the distance from the center of the particle, r.

For $r > a$,

$$\frac{1}{r^2}\frac{d}{dr}\left(r^2 \frac{dy_0(r)}{dr}\right) = -\frac{Fe}{\varepsilon_0 \varepsilon_r \kappa_B \mathrm{T}} \sum_j m_j z_j \omega(r) e^{-z_j y_0(r)} \qquad (2-53)$$

$$\left(\frac{\partial y_0}{\partial r}\right)_{r=\alpha_+} = -\frac{\alpha_1}{\alpha} \qquad (2-54)$$

In Eq. (53), $\omega(r)$ is a step function which equals 0 for r < a_{ex} and 1 for r > a_{ex}. In Eq. (54), $\alpha_1 = e^2 Z/(4\varepsilon_0\varepsilon_r k_B T a)$ (dimensionless) and Z is the net valence charge of the particle. For a weakly charged particle, the exponential in Eq. (53) can be expanded and the resulting linear equation can be solved analytically. This is the linear Poisson–Boltzmann equation and the reduced (dimensionless) potential for the present problem for r > a can be written

$$y_0^{LPB}(r) = \begin{cases} \alpha_1\left(\dfrac{\alpha}{r} - \dfrac{\kappa\alpha}{1+\kappa\alpha_{ex}}\right) & \alpha < r < \alpha_{ex} \\ \dfrac{\alpha_1\alpha}{r(1+\kappa\alpha_{ex})} e^{-\kappa(r-\alpha_{ex})} & \alpha_{ex} < r \end{cases} \qquad (2-55)$$

The ‘‘LPB” superscript on y_0 denotes the linear Poisson Boltzmann reduced potential. In the present work, however, the general non-linear for of Eq. (2-53) is solved numerically subject to the boundary condition imposed by Eq. (2-54).

For the nonequilibrium problem, we follow the strategy of carrying out two separate transport cases (30). In Case 1, the particle is translated with constant velocity, $\underline{u}_0$, in a fluid that is otherwise at rest. In Case 2, the particle is held stationary, but it is subjected to a constant external electric field, $\underline{e}_0$. Although the potentials, $\Phi_j^{(i)}(\underline{r})$ are not spherically symmetric (the (i) superscript has been added to distinguish the two transport cases), they can be written in terms of related functions that are [30],

$$\Phi_j^{(i)}(\underline{r}) = \frac{1}{r}\phi_j^{(i)}(r)\underline{\underline{b}}^{(i)} \cdot \underline{r} \qquad (2-56)$$

Where $\underline{b}^{(1)}$ and $\underline{b}^{(2)} = \underline{e}_0$. As discussed in detail previously [30], the coupled equations for the fluid velocity and ion transport are cast into the form of 1 dimensional differential equations

in the radial variable r. These are then solved numerically for the two transport cases. Let N denote the number of mobile ions species present (which is two for a binary electrolyte). For each transport case, N + 2 homogeneous and one inhomogeneous set of differential equations are solved subject to different distant boundary conditions. The overall solution for Case 1 or 2 is then taken to be a particular linear combination of the above mentioned N + 3 ‘‘distant” solutions that satisfy appropriate boundary conditions at r = a_{ex}. The overall solution of $\phi_j(r)$ for case i (i = 1 or 2), is

$$\phi_j^{(i)}(r) = \sum_{\kappa=0}^{N+2} d_\kappa^{(i)} \phi_j^{(i-\kappa)}(r) \qquad (2-57)$$

Where the sum over k extends over the inhomogeneous (k = 0) and different homogeneous (j = 1 to N + 2) ‘‘distant” solutions, $\Phi_j^{(i-k)}(x)$ is the k-th ‘‘distant” solution for case i and ion j, and the $d_k^{(i)}$ are the lin-ear coefficients that are determined from boundary conditions on or near the particle as discussed later. For k = 0 or N + 1 or N + 2, the outer boundary condition on $\Phi_j^{(i-k)}(x)$ is set to 0. For k = 1 to N,

$$\phi_j^{(i-\kappa)}(r) = \frac{\delta_{j,\kappa}}{r^2} \quad (\kappa r >> 1) \qquad (2-58)$$

Where $\delta_{j,k}$ is the Kronecker delta.

The remaining two homogeneous ‘‘distant” solutions (k = N + 1 or N + 2) are associated with the distant behavior of a scalar field, $g^{(i)}(r)$, from which the fluid velocity, $\underline{v^{(1)}}(\underline{r})$, is derived (30). It is defined by

$$\underline{v^{(i)}}(\underline{r}) = \underline{curl}\left[\underline{curl}\left[g^{(i)}(r)\underline{b^{(i)}}\right]\right] + \underline{u_\infty^{(i)}} \qquad (2-59)$$

Where $\underline{\underline{b^{(i)}}}$ is defined following Eq. (2-55) and $\underline{\underline{u_{\infty}^{(1)}}} = -\underline{u_0}$, and $u_{\infty}^{(2)} = 0$. The ‘‘distant” solutions of $g^{(i-j)}$ are set to zero except for j = N+ 1

$$g^{(i-\mathrm{N}+1)}(r) = r \qquad (2-60)$$

$$g^{(i-\mathrm{N}+2)}(r) = \frac{1}{r} \qquad (2-61)$$

The final expression for $g^{(i)}(r)$ can be written that is identical to Eq. (2-57) above with $g^{(i-k)}$ replacing $\phi j^{(i-k)}$. The $d_k^{(i)}$ coefficients appearing in Eq. (2-57) and an analogous relation involving $g^{(i)}(r)$ and $g^{(i-k)}(r)$ are determined from ‘‘inner” boundary conditions. These are discussed in reference [30] for the special case of ‘‘stick” boundary conditions when a = a_{ex}, but the more general conditions of interest here must be handled differently. The boundary conditions on $\phi_j^{(i)}(r)$ follow from Eq. (2-52) and are simply $\phi_j^{(1)'}(a_{ex}) = 0$ and $\phi_j^{(2)'}(a_{ex}) = 0$, where the prime superscript denotes first derivative with respect to r. These are the same for both ‘‘stick” and ‘‘slip” hydrodynamic boundary conditions. The boundary conditions on $g^{(i)}$ are evaluated at r = a and are different for ‘‘stick” and ‘‘slip”. For ‘‘stick”; $g_j^{(1)'}(a) = -a/2$, $g_j^{(1)''}(a) = -1/2$ and $g_j^{(2)''}(a) = 0$ where the double prime denotes second derivative with respect to r. For ‘‘slip”; careful analysis leads to the conditions: $g_j^{(1)'}(a) = -a/2$, $g_j^{(1)'''}(a) = 0$, and $g_j^{(2)''}(a) = 0$ where the triple prime denotes third derivative with respect to r. With minor modifications in Eq. (7.7) of reference [30] that incorporate these modified boundary conditions, the $d_k^{(i)}$ coefficients can be uniquely determined for Cases 1 and 2. The overall solution is then

taken to be the linear superposition of both Cases 1 and 2 fields that gives a net force exerted by the particle on the fluid of zero [30].

At this point, it is appropriate to discuss how the results of Case 1 and Case 2 transport studies can be used to obtain a general expression for the electrophoretic mobility, l, and then reduce that to more recognizable forms in special cases. It is possible to obtain a general expression of the electrophoretic mobility starting from the differential form of the Lorentz reciprocal theorem [73, 74],

$$\underline{s}^0 \cdot \underline{v}^{(i)} + \underline{\nabla} \cdot \left(\underline{v}^{(i)} \cdot \underline{\underline{\sigma}}_{\mathrm{H}}^0 \right) = \underline{s}^{(i)} \cdot \underline{v}^0 + \underline{\nabla} \cdot \left(\underline{v}^0 \cdot \underline{\underline{\sigma}}_{\mathrm{H}}^{(i)} \right) \qquad (2-62)$$

Where quantities with superscript (i) denote the actual fields around a charged spherical particles (i = 1 or 2) and quantities with superscript 0 denote an arbitrary flow field that obeys Eqs. (2-37) and (2-38) subject to appropriate hydrodynamic boundary conditions. For the arbitrary fields, choose an uncharged sphere of radius a (same as the radius of our charged particle) where $\underline{v}^0$ is given by Eqs. (2-39)– (2-42). Integrate Eq. (2-62) over the fluid domain, Ω, exterior to a single isolated particle enclosed by surface S_p with outward normal (into the fluid), $\underline{n}$. Applying the divergence theorem yields

$$-\int_{S_\rho} \underline{v}^{(i)} \cdot \underline{\underline{\sigma}}_{\mathrm{H}}^0 \cdot \underline{n} dS = -\int_{S_\rho} \underline{v}^0 \cdot \underline{\underline{\sigma}}_{\mathrm{H}}^{(i)} \cdot \underline{n} dS + \underline{u}^* \cdot \int_\Omega \underline{\underline{\mathrm{T}}} \cdot \underline{S}^{(i)} dV \qquad (2-63)$$

The total hydrodynamic force exerted by the particle on the fluid is

$$\underline{F}_{\mathrm{H}}^{(i)} = -\int_{S_\rho} \underline{\underline{\sigma}}_{\mathrm{H}}^{(i)} \cdot \underline{n} dS \qquad (2-64)$$

And an entirely analogous expression can be written for $\underline{F}_H^0$. For ‘‘stick” boundary conditions, the fluid velocities inside the surface integrals are constant and can be moved outside

the integral directly. For the ‘‘slip” case, first recognize that we can write $\underline{\underline{\sigma_H}} \cdot \underline{n} = (\underline{\underline{nn}}) \cdot (\underline{\underline{\sigma_H}} \cdot \underline{n})$. Since the normal component of the fluid velocity matches that of the particle on S_p in the slip case and since only the normal component contributes to the surface integrals, we can move them out of the integrals also. The total force exerted by the particle on the fluid is the sum of hydrodynamic and external (electrical) forces [30, 38, 75]

$$\underline{F_{\mathrm{T}}^{(i)}} = \underline{F_{\mathrm{H}}^{(i)}} + \int_{\Omega} \underline{s}^{(i)} dV \qquad (2-65)$$

Using Eqs.(2-64) in Eq.(2-63)

$$\underline{u^*} \cdot \underline{F_{\mathrm{T}}^{(i)}} = \underline{u^{(i)}} \cdot \underline{F_{\mathrm{H}}^{0}} + \underline{u^*} \cdot \int_{\Omega} \left(\underline{\underline{\mathrm{I}}} - \underline{\underline{\mathrm{T}}}\right) \cdot \underline{s}^{(i)} dV \qquad (2-66)$$

In Eq. (2-66), $\underline{u^*}$ is the velocity of our uncharged particle and $\underline{u^{(i)}}$ the velocity of our charged particle (Case 1 or 2). The external force term can be written [38, 75]

$$\underline{s}^{(i)} = F \sum_j z_j n_{j0} \left(\underline{\nabla} \Phi_j^{(i)} + \underline{e_0} \delta_{i2}\right) + R\mathrm{T} \sum_j \underline{\nabla} n_j^{(i)} \qquad (2-67)$$

Using Eqs. (2-40), (2-42), (2-56)–(2-58), and (2-67) in (2-66), it is straightforward to carry out the angular integrations. Also, the divergence theorem is applied to the second term on the right hand side of Eq. (2-67). Without loss of generality, we can also assume the electric/ flow fields are along the x direction with $(\underline{u^*}) = 1$ and only concern ourselves with the x components of the overall forces. Eq. (2-66) can

$$F_{\mathrm{T}}^{(i)} = u^{(i)} f_0 - \frac{4}{3} \pi F b^{(i)} \sum_j z_j m_j d_j^{(i)} + 4\pi F \sum_j z_j \int_{\alpha}^{\infty} r^2 dr n_{j0}(r) g_j^{(i)}(r) \qquad (2-68)$$

$$g_j^{(i)} = \left(1 - \frac{4}{3} h_1\right) e^{(i)} + \frac{2}{3}(1 - h_1 - h_2) \frac{\phi_j^{(i)}}{r} b^{(i)} + \frac{1}{3}(1 - 2h_1 + 2h_2) \phi_j^{(i)\prime} b^{(i)} \qquad (2-69)$$

$$f_0 = 6\pi\eta\alpha(stick);\quad 4\pi\eta\alpha(slip) \qquad (2-70)$$

$$h_1 = \frac{3\alpha}{4r}(stick);\quad \frac{\alpha}{2r}(slip) \qquad (2-71)$$

$$h_2 = \frac{1}{4}\left(\frac{\alpha}{r}\right)^3(stick);\quad 0(slip) \qquad (2-72)$$

$$\mu = \frac{4\pi F\sum_j z_j\left(m_j d_j^{(2)}/3-\rho_j^{(2)}\right)}{\left(f_0 - 4\pi F\sum_j z_j\left(m_j d_j^{(1)}/3-\rho_j^{(1)}\right)\right)} \qquad (2-73)$$

$$\rho_j^{(i)} = \int_\alpha^\infty r^2 dr n_{j0}(r)\left[\left(1-\frac{4}{3}h_1\right)\delta_{i2} + \frac{2}{3}(1-h_1-h_2)\frac{\phi_j^{(i)}}{r} + \frac{1}{3}(1-2h_1+2h_2)\phi_j^{(i)'}\right] \qquad (2-74)$$

Eqs. (2-73) and (2-74) are general expressions for the mobility of a sphere and simplify in limiting special cases.

Consider the special case where ion relaxation is neglected. This is a reasonable approximation when the particle is weakly charged and the solution of the linear Poisson Boltzmann equation, Eq. (2-55), is appropriate. Under these conditions, $\phi_j^{(1)} = 0$, $d_j^{(1)} = 0$, $\phi_j^{(2)} = ca^3/r^2$, $d_j^{(2)} = ca^3$, where $c = (\varepsilon_r - \varepsilon_i)/(2\varepsilon_r + \varepsilon_i)$ All of the terms with superscript (1) vanish in Eq. (2-73) and the $d_j^{(2)}$ term also drops out when we sum over j and impose the condition of charge neutrality. Under these conditions, Eq. (2-73) reduces to

$$\mu_{nr} = \frac{eZ}{f_0} + \frac{4\pi}{f_0}\int_\alpha^\infty r^2 dr\rho_0(r)\left[\frac{4}{3}h_1 - \frac{2c\alpha^3}{3r^3}(h_1-3h_2)\right] \qquad (2-75)$$

The ‘‘nr” subscript denotes the ‘‘no relaxation” limiting case and ρ_0 is the equilibrium charge density. For the ‘‘stick” and ‘‘slip” cases, Eq. (75) reduces to

$$\mu_{nr}^{stick} = \frac{eZ}{6\pi\eta\alpha} + \frac{2}{3\eta}\int_{\alpha}^{\infty} r dr \rho_0(r)\left[1 - \frac{c}{2}\left(\frac{\alpha}{r}\right)^3 - \left(\frac{\alpha}{r}\right)^5\right] \qquad (2-76)$$

$$\mu_{nr}^{slip} = \frac{eZ}{4\pi\eta\alpha} + \frac{2}{3\eta}\int_{\alpha}^{\infty} r dr \rho_0(r)\left[1 - \frac{c}{2}\left(\frac{\alpha}{r}\right)^3\right] \qquad (2-77)$$

It is straightforward to reduce these equations further. The charge

$$\rho_0(r) = F\sum_j z_j m_j^{'} e^{-z_j y_0(r)} \cong -2F\mathrm{I}^{'} y_0^{\mathrm{LPB}}(r) \qquad (2-78)$$

where $I^{'} = (\sum_j m_j^{'} z_j^2)/2$ is the ionic strength in moles/m^3, $m_j^{'}$ is the ambient concentration of species j in moles/m^3, the exponential has been expanded and only the linear term in y_0 has been retained. Furthermore, y_0 has been approximated by its linear form given by Eq. (2-55). Making use of Eqs. (2-55) and (2-78) in (2-76) and (2-77),

$$\mu_{nr}^{stick} = \frac{eZ}{6\pi\eta\alpha} - \frac{4\alpha F\mathrm{I}^{'}\alpha_1}{3\eta(1+\kappa\alpha_{ex})}\int_{\alpha_{ex}}^{\infty} dr e^{-\kappa(r-\alpha_{ex})}\left[1 - \frac{c}{2}\left(\left(\frac{\alpha}{r}\right)^3 - \left(\frac{\alpha}{r}\right)^5\right)\right] \qquad (2-79)$$

$$\mu_{nr}^{slip} = \frac{eZ}{4\pi\eta\alpha} - \frac{4\alpha F\mathrm{I}^{'}\alpha_1}{3\eta(1+\kappa\alpha_{ex})}\int_{\alpha_{ex}}^{\infty} dr e^{-\kappa(r-\alpha_{ex})}\left[1 - \frac{c}{2}\left(\frac{\alpha}{r}\right)^3\right] \qquad (2-80)$$

The first term in brackets within the integrand on the right hand sides of Eqs. (2-79) and (2-80) can be integrated directly and the c-terms can be reduced to exponential integrals. This shall not be done here. Eqs. (2-79) and (2-80) provide a straightforward way of estimating the effect of hydrodynamic boundary conditions and ion exclusion on electrophoretic mobility of

weakly charged spherical particles. One example shall be given. Consider $a = a_{ex}$ and c = 1/2, Eq. (79) reduces to the Henry law mobility [26, 74]. The ratio of ‘‘slip” to ‘‘stick” mobilities increases from 1.50, 1.56, 1.77, 2.07, and 3.30 for κa = 0, 0.12, 0.52, 1.10, and 3.39, respectively.

2.2.3 Analysis of Conductance Data

Both the ‘‘small ion” and ‘‘large ion” theories described in the previous two sections offer advantages and disadvantages and the principle objective of this work is to bridge these two approaches and show how they complement each other. The greatest advantage of the ‘‘small ion” approach is that it accounts for the Brownian motion of the principle ion of interest whereas the ‘‘large ion” approach does not. The greatest advantage of the ‘‘large ion” approach is that it accounts more accurately for the finite size of the ion and is not restricted to weakly charged ions. (The ‘‘small ion” theories always employ the linearized form of the Poisson– Boltzmann equation.) From Eq. (2-9), we have the relationship be-tween equivalent ionic conductance, Λ_j, and absolute mobility, $|\mu_j|$. In the limit of zero electrolyte, relaxation and electrophoretic, the greatest advantage of the ‘‘small ion” approach is that it accounts for the Brownian motion of the principle ion of interest whereas the ‘‘large ion” approach does not. The greatest advantage of the ‘‘large ion” approach is that it accounts more accurately for the finite size of the ion and is not restricted to weakly charged ions. (The ‘‘small ion” theories always employ the linearized form of the Poisson– Boltzmann equation.) From Eq. (2-9), we have the relationship be-tween equivalent ionic conductance, Λ_j, and absolute mobility, $|\mu_j|$. In the limit of zero electrolyte, relaxation and electrophoretic

$$\Lambda_{j0} = F \mid \mu_{j0} \mid = \frac{Fe \mid z_j \mid}{\alpha_2 \pi \eta \alpha_j} \qquad (2-81)$$

where z_j is the valence charge on ion j and α_2 equals 6 for ‘‘stick” and 4 for ‘‘slip” boundary conditions. In the present work, Λ_{j0} are used as input data and a_j will depend on the hydrodynamic boundary condition assumed. In water at $25^\circ C$ with Λ_{j0} given in 10^{-4} m^2/ (ohm mole) and a_j in nm,

$$\alpha_j(nm) = \frac{55.28 \mid z_j \mid}{\alpha_2 \Lambda_{j0}\left(10^{-4}\, m^2/(ohm\, mole)\right)} \qquad (2-82)$$

When the ‘‘slip” boundary condition is used, the a_j values must be scaled by a factor of 3/2 relative to the ‘‘stick” condition. In the ‘‘small ion” theory [2, 3, 5–8, 63–70], size enters implicitly through the Λ_{j0} terms and explicitly through the ion exclusion distance, a_{ex}. The effect of a_{ex} on conductance becomes significant at higher electrolyte concentration. Also, hydrodynamic boundary conditions are usually dealt with by assuming ‘‘slip” boundary conditions hold on the ion exclusion surface at r = a_{ex}, and not at r = a_j. (In the theory of Pitts [5], ‘‘stick” boundary conditions are assumed to hold at r = a_{ex}.) In the ‘‘large ion” theories, the ion hydration radius does enter directly. With regard to the ion on interest, it enters through the hydrodynamic boundary condition on g(r) at r = a as discussed fol-lowing Eq. (2-59). Ionic hydration radii also enter indirectly for all ions making up the background electrolyte in the solution of the ion transport equation, Eq. (2-51). The ion diffusion constant, D_j, appearing in Eq. (2-51) are related to a_j and Λ_{j0} by the Einstein relation [76]

$$D_j = \frac{\mathrm{K_B T}}{\alpha_2 \pi \eta a_j} = \frac{k_\mathrm{B} \mathrm{T} \Lambda_{j0}}{Fe \mid z_j \mid} \qquad (2-83)$$

However, availability of limiting ionic conductance data makes explicit reference to a_j unnecessary with regard to the relaxation correction.

A shortcoming of the ‘‘large ion” theories is that it ignores the Brownian motion of the ion of interest, call it ion k. Provided this ion is much larger than the other ions making up the background electrolyte, that assumption is a reasonable approximation since $D_k \propto 1/a_k$. However, if ion k is comparable in size the other ions, the approximation is expected to break down and a comparison of experimental conductances with both ‘‘small ion” and ‘‘large ion” theories shall give us an opportunity to evaluate this assumption. In the theory of diffusion controlled reactions, it is well known that the mutual diffusion constant of two species is simply the sum of the individual diffusion constants of the two species [77–79]. A simple way of correcting the ‘‘large ion” theory to ac-count for the Brownian motion of the central ion is to replace D_j or a_j appearing in the ion transport equation with (D_j + D_k) or

$$\alpha_j^{eff} = \left(\frac{1}{\alpha_j} + \frac{1}{\alpha_\kappa} \right)^{-1} \qquad (2-84)$$

Since the relaxation process is dominated by the counterion, a single a_j^{eff} is used for binary electrolytes, where a_j and a_k in Eq. (2-85) are coion and counterion radii. Both uncorrected and corrected applications of ‘‘large ion” theory to conductance data shall be reported below.

In the analysis of experimental conductance data below, which is all in aqueous media at $25^\circ C$, we shall use data summarized in the Handbook of Chemistry and Physics [80] covering the concentration range $0.0 \le am_0 z \le 0.02$. We shall first examine the simple monovalent salt, KCl, since it has been extensively studied in the past using the ‘‘small ion” theory [6,7]. Using the ‘‘small ion” theory and treating a_{ex} as an adjustable parameter, we shall attempt to obtain good agreement between theory and experiment as well as confirm the conclusions of past work [6,7]. For a mono-valent salt like KCl, we expect the ‘‘small ion” theory to work as well as it possibly can since the ions are both small and weakly charged. Then using this a_{ex}, the ‘‘large ion” theory will be applied to KCl for both ‘‘stick” and ‘‘slip”, and ‘‘uncorrected” and ‘‘corrected” (according to Eq. (2-85)) cases. The full numerical approach outlined in the previous section shall be applied in these cases. It should be emphasized that once a_{ex} is fixed, once ‘‘stick” or ‘‘slip” hydrodynamic boundary conditions are assumed, and once uncorrected or corrected mobile ion radii are selected, there are no further adjustable parameters in the ‘‘large ion” theory.

2.3 Results

2.3.1 Application to KCl

For KCl, we use [55] Λ_0 = 149.79×10^4 m^2/(ohm mole), T = $25^\circ C$, η = 0.89 cp, and ε_r = 78.53 in the small ion theory for a bin-ary symmetric electrolyte. The relative error of the equivalent conductance of this salt falls in the range of several hundredths of one percent [81]. For this case, α = 0.22940 and β = 60.575×10^4 m^2/ (ohm mole). It is straightforward to show that a_{ex} = 0.350 nm yields best agreement between theory and experiment which confirms the finding of Fuoss and Onsager [7]. Experimental and ‘‘small ion” model conductances are

summarized in Table 1, where Λ_p , Λ_1 and Λ are given by Eqs. (2-1), (2-32), and (2-27), respectively. The ‘‘point ion” model for conductance, Λ_p , clearly does not work well at higher concentrations, but the full model, Λ , and the approximate finite ion model, Λ_1 , work quite well, Shown in the last two columns of Table 1 is the relative percent error defined by

$$\Delta = 100\left(\frac{\Lambda - \Lambda_{ex\rho}}{\Lambda_{ex\rho}}\right) \qquad (2-85)$$

For Δ_1 , Λ_1 replaces Λ in Eq. (2-86). Both Λ and Λ_1 reproduce experimental conductances to well within an accuracy of several tenths of 1% although the full model is slightly better at the highest ionic strength considered. This serves to demonstrate that the approximate finite ion model works quite well in reproducing the experimental equivalent conductance of KCl. This is useful since the approximate finite ion model is much simpler than the full finite ion model and can also be applied directly to ternary and higher order electrolytes as discussed in Section 2.

The corresponding results for the ‘‘large ion” model studies are summarized in Table 2-2. Full numerical calculations are carried out for each ion. Mobilities are computed for both K^+ (a_+ = 0.125 nm (stick), 0.1875 nm (slip)) and Cl^- (a_- = 0.121 nm (stick), 0.1815 nm (slip)) and a_{ex} = 0.350 nm. In the ‘‘uncorrected” cases, the ion of interest (K^+ or Cl^-) is translated with constant velocity (Case 1) or held stationary (Case 2). Diffusion constants, D_j, used in the ion transport equation are obtained from Eq. (84). In the ‘‘corrected” cases, the ion of interest is also held constant, but effective ion radii defined by Eq. (85) are used in Eq. (84). The third and fourth columns

$m_0(M)$	Λ_{exp}	Λ_p	Λ_1	Λ	Δ_1	Δ
0.0005	147.74	147.67	147.71	147.68	-0.02	-0.04
0.001	146.88	146.79	146.87	146.82	-0.01	-0.04
0.005	143.48	143.08	143.46	143.41	-0.01	-0.05
0.01	141.2	140.3	141.05	141.07	-0.01	-0.09
0.02	138.27	136.36	137.8	138.07	-0.34	-0.14

Table 2-1: Comparison of KCl equivalent conductance between experiment and small ions theory.[a]

[a] All Λ values are in 10^{-4} m^2/(ohm mole).

$m_0(M)$	Λ_{exp}	$\Lambda(stick,u)^b$	$\Delta(stick,u)$	$\Lambda(stick,u)^c$	$\Delta(stick,c)$	$\Lambda(stick,u)^d$	$\Delta(stick,d)$
0.0005	147.74	147.26	-0.32	147.82	0.054	147.88	0.095
0.001	146.88	146.22	-0.45	146.99	0.075	147.02	0.095
0.005	143.48	142.09	-0.97	143.61	0.091	143.61	0.091
0.01	141.2	139.36	-1.3	141.28	0.057	141.31	0.078
0.02	138.27	135.96	-1.67	138.33	0.043	138.41	0.101

Table 2-2: Comparison of equivalent conductance between experiment and large ion theory. [a]

[a] All Λ values are in 10^{-4} m^2/(ohm mole).

[b] Stick boundary conditions and not corrected for Brownian motion of the ion of interest.

[c] Stick boundary conditions and corrected for Brownian motion of the ion of interest.

[d] Slip boundary conditions and corrected for Brownian motion of the ion of interest.

Of Table 2-2 summarize the ‘‘uncorrected” model mobilities with stick boundary conditions. These model studies underestimate the equivalent conductance by 0.3-1.7% and the discrepancy increases with increasing salt. The physical basis of this discrepancy is that the relaxation effect is overestimated here as a consequence of ignoring the Brownian motion of the ion of interest. The corresponding ‘‘corrected” conductance are shown in columns 5 and 6 and here we are clearly doing much better. As in the case of the ‘‘small ion” model studies, we are now able to reproduce experimental conductance’s to an accuracy that is better than 0.1%. In

columns 7 and 8, the corresponding ‘‘corrected” model conductance with ‘‘slip” boundary conditions are presented. As mentioned previously, we have had to scale the ionic hydration radii by 1.5 relative to the ‘‘stick” model values in order to properly account for Λ_{+0} and Λ_{-0}. As in the case of the corrected ‘‘stick” model conductance, the corrected ‘‘slip” conductance reproduce experimental values to an accuracy of better than 0.1%. Provided the hydrodynamic radii of the two ions are scaled in the manner discussed previously, the resulting model conductivities are very similar for ‘‘stick” and ‘‘slip” models.

2.3.2 Application to $MgCl_2$ and $LaCl_3$

As in the case of KCl, conductivity data for $MgCl_2$ and $LaCl_3$ is taken from reference [56]. Specifically, Λ_0 ($MgCl_2$/2) = 129.34 (in 10^{-4} m^2/(ohm mole)), Λ_0 ($LaCl_3$/3) = 145.9, Λ_0(Mg^{+2}/2) = 53.0, Λ_0(La^{+3}/3) = 69.7. $K_0(Cl^-)$ = 76.31. The ion radii, a_j, are derived from the limiting equivalent conductance using Eq. (2-83). With regard to the ‘‘small ion” model, the only remaining adjustable parameter is a_{ex}. For both $MgCl_2$ and $LaCl_3$, this parameter is varied in an attempt to get as good agreement as possible between experimental conductivities and full model conductivities from Eqs. (2-27)–(2-31). For $MgCl_2$, Eqs. (2-9), (2-11), (2-10), (2-15), and (2-16) give: ϕ = 1.732, q = 0.4199, S = 0.5096, α = 0.6913, and $\beta = 157.38\times10^4$ m^2/(ohm mole). For we have found a_{ex} = 0.52 nm for $MgCl_2$ and 0.60 nm for $LaCl_3$ give model conductivities in best agreement with experiment. Results of the ‘‘small ion” model fits with experiment are summarized in Table 2-3. As in the case of KCl, fits accurate to within several tenths of one percent are possible for both salts. The corresponding fits for K_1 (using a_{ex} optimized in matching Λ_{exp} and Λ) are not as good, but still fall below a relative error of 1%.

We next consider the ‘‘large ion” model. In computing the relaxation correction, Eq. (2-85) is used to account for the Brownian motion of both ions. Tables 2-4 and 2-5 summarize the model results and their comparison with experiment for $MgCl_2$ and $LaCl_3$, respectively. The y_0 values represent the reduced equilibrium electro-static potential (Eq. (2-49)) at a_{ex} equal to 0.52 nm (for $MgCl_2$) and 0.60 nm (for $LaCl_3$). These come from numerical solution of the non-linear Poisson Boltzmann equation. For $y_0(Mg^{+2}, a_{ex})$ the central ion has a valence charge of +2 and for $y_0(Cl^-, a_{ex})$, the central ion has a valence charge of -1, etc. For Mg^{+2} or La^{+3}, $|y_0|$ ranges from 2.14 to 3.37. For monovalent Cl^-, it lies closer to 1.0. The large absolute electrostatic potentials near Mg^{+2} and La^{+3} illustrate the importance of going beyond the linear Poisson Boltzmann equation when polyvalent ions are present.

$z_+m_0(M)$					
	0.0005	0.001	0.005	0.01	0.02
$MgCl_2$					
Λ_{exp}	125.55	124.15	118.25	114.49	109.99
Λ_p	125.31	123.64	116.59	111.31	103.85
Λ_1	125.58	124.09	118.25	114.26	109.09
Λ	125.44	123.9	118.04	114.33	109.94
Δ_1	0.024	-0.048	0	-0.201	-0.818
Δ	-0.088	-0.201	-0.178	-0.14	-0.045
$LaCl_3$					
Λ_{exp}	139.6	137	127.5	121.8	-
Λ_p	138.9	136	123.77	114.6	-
Λ_1	139.88	137.54	128.64	122.42	-
Λ	139.45	136.92	127.64	122.12	-
Δ_1	0.201	0.394	0.776	0.525	-
Δ	-0.107	-0.058	0.11	0.263	–

Table 2-3 Conductance Data for $MgCl_2$, and $LaCl_3$ (small ion model)

$m_0(M)$	0.00025	0.0005	0.0025	0.005	0.01
Λ_{exp}	125.55	124.15	118.25	114.49	109.99
Stick					
$y_0(Mg^{2+}, a_{ex})$	2.62	2.58	2.4	2.28	2.14
$y_0(Cl^{-1}, a_{ex})$	1.31	1.28	1.17	1.1	1.02
$E_+(nr)$	4.018	3.972	3.794	3.678	3.532
$-E_-(nr)$	5.83	5.803	5.696	5.628	5.544
$E_+(r)$	4.028	3.979	3.784	3.656	3.498
$-E_-(r)$	5.705	5.629	5.346	5.191	5.019
ξ_{s+}	-0.0025	-0.0018	0.0026	0.006	0.0096
ξ_{s-}	0.0214	0.03	0.0614	0.0776	0.0947
$\Lambda(nr)$	127.23	126.29	122.62	120.22	117.27
$\Lambda(r)$	125.74	124.13	117.97	114.3	110.04
$\Delta(r)$	0.151	-0.016	-0.236	-0.166	0.045
Slip					
$E_+(nr)$	4.018	3.973	3.799	3.686	3.547
$-E_-(nr)$	5.83	5.803	5.697	5.628	5.544
$E_+(r)$	4.029	3.981	3.793	3.67	3.52
$-E_-(r)$	5.708	5.629	5.352	5.193	5.027
ξ_{s+}	-0.0027	-0.002	0.0016	0.0043	0.0076
ξ_{s-}	0.0209	0.03	0.0606	0.0773	0.0932
$\Lambda(nr)$	127.24	126.3	122.69	120.34	117.47
$\Lambda(r)$	125.8	124.17	118.16	114.5	110.42
$\Delta(r)$	0.199	0.016	-0.076	0.009	0.391

Tables 2-4 Conductance/mobility data on $MgCl_2$ (large ion model)

$m_0(M)$	0.000167	0.000333	0.001667	0.0033
Λ_{exp}	125.55	124.15	118.25	114.49
Stick				
$y_0(La^{+3}, a_{ex})$	3.37	3.31	3.03	2.85
$y_0(Cl^{-1}, a_{ex})$	1.11	1.07	0.95	0.87
$E_+(nr)$	5.199	5.127	4.853	4.679
$-E_-(nr)$	5.814	5.779	5.654	5.58
$E_+(r)$	5.27	5.195	4.879	4.674
$-E_-(r)$	5.559	5.429	4.988	4.78
ξ_+	-0.0135	-0.0132	-0.0054	0.0011
ξ_-	0.0443	0.0617	0.1179	0.1435
$\Lambda(nr)$	142.28	140.91	135.76	132.55
$\Lambda(r)$	139.86	137.17	127.48	122.14
$\Delta(r)$	0.186	0.124	0.016	-0.278
Slip				
$E_+(nr)$	5.205	5.134	4.867	4.7
$-E_-(nr)$	5.828	5.792	5.66	5.582
$E_+(r)$	5.279	5.206	4.906	4.716
$-E_-(r)$	5.557	5.409	4.932	4.702
ξ_+	-0.0141	-0.014	-0.0081	-0.0034
ξ_-	0.0464	0.0661	0.1287	0.1576
$\Lambda(nr)$	142.54	141.16	136.01	132.83
$\Lambda(r)$	140	137.14	127.11	121.67
$\Delta(r)$	0.286	-0.102	0.306	-0.107

Table 2-5 Conductance /mobility data on $LaCl_3$ (large ion model)

Mobility, μ_j, of both positive and negative ions are computed in the absence, nr, and presence, r, of ion relaxation. Presented in the table are dimensionless reduced mobilities defined by

$$\mathrm{E}_j = \frac{3\eta e}{2\varepsilon_0 \varepsilon_r \mathrm{K_B T}} \mu_j \qquad (2-86)$$

The relaxation correction is then obtained from

$$\xi_j = 1 - \frac{\mathrm{E}_j(r)}{\mathrm{E}_j(nr)} \qquad (2-87)$$

2.4 Discussion

In this work, we have examined two complementary continuum theories of electrokinetic solutions that are called collectively the "small ion" [1-3, 5-8, 63-70] and "large ion" [26-30, 48, 62, 75] models. Conductance data of dilute binary electrolyte solutions is readily available, fairly extensive, and accurate [80, 81] models. This is true not only for monovalent binary electrolytes, but electrolytes made up of polyvalent ions as well. This coupled with the relative simplicity of these systems makes them ideal for evaluating the accuracy and "goodness" of the theory and modeling strategy. This approach was taken more than 50 years ago in the pioneering studies of Pitts [5], Fuoss, and Onsager [6, 7] on the conductance of monovalent binary electrolytes. Their work is the basis of the "small ion" model in the present study. These early investigators were justifiably cautious about extending their modeling to polyvalent electrolytes due to the largely unknown limitations of the linear Poisson-Boltzmann equation that they employed. The "small ion" theory has been generalized to an electrolyte consisting of more than two ions of arbitrary valence. [8, 66], but the linear Poisson-Boltzmann equation is employed. Independently and later, progress was made in modeling the electro kinetic transport of large highly charged particles and numerical procedures made possible by computers played a vital role in these developments. First, was the development of numerical procedures to solve the non-linear Poisson Boltzmann equation around a spherical particle with a centrosymmetric charge distribution [82]. More complicated numerical procedures to solve electro kinetic transport were developed later [29,30,48]. These numerical procedures are the basis of the ‘‘large ion” modeling of the present study. Given the focus of the present study, the ‘‘large ion” model was generalized

to include an ion exclusion distance and also to option of considering ‘‘stick” or ‘‘slip” hydrodynamic boundary conditions. A simple corrective procedure was also developed to account for the Brownian motion of all ions in the determination of the relaxation correction.

In an attempt to bridge the ‘‘small ion” and ‘‘large ion” modeling methodologies, the conductance of dilute binary electrolytes made up of both monovalent and polyvalent ions represent ideal test cases for study. The high electrostatic potential around polyvalent ions tests the limits of the ‘‘small ion” model and their small size tests the limits of the ‘‘large ion” model. Both models are applied to the binary salt solutions KCl, $MgCl_2$, and $LaCl_3$ and these results, in turn, compared with experiment. In both ‘‘small ion” and ‘‘large ion” models, the only remaining adjustable parameter is the ion exclusion distance, a_{ex} For a_{ex} equal 0.35, 0.52, and 0.60 nm for KCl, $MgCl_2$, and $LaCl_3$ both ‘‘small ion” and ‘‘large ion” models are able to reproduce experimental conductivities to an accuracy of several tenths of one percent or better. For the ‘‘large ion” model with ‘‘slip” hydrodynamic boundary conditions, an a_{ex} of 0.55 nm was necessary to get good agreement with experiment for $LaCl_3$. Also, it is necessary to correct the ‘‘large ion” model for Brownian motion of both ions using Eq. (2-85). The fact that the ‘‘small ion” model works as well as it does for $MgCl_2$, and $LaCl_3$ is surprising given the limitations of the electrostatic model upon which it is based. The results of the present work indicate that the ‘‘small ion” theory can be applied to polyvalent electrolytes provided $|z_j| \leq 3$. It is not possible to distinguish whether or not a ‘‘large ion - stick” or ‘‘large ion-slip” model takes better account of conductance data since both are capable of comparable accuracy.

Fig. 2-1 summarizes the reduced conductivity data for data KCl, $MgCl_2$, and $LaCl_3$ for both experiment and ‘‘large ion-stick” models. Squares, diamonds and triangles correspond to

experimental data for KCl, $MgCl_2$, and $LaCl_3$, respectively. The solid line, widely spaced dashed line, and short spaced dashed line correspond to model data for KCl, $MgCl_2$, and $LaCl_3$, respectively. The other model studies considered, ‘‘small ion”, and ‘‘large ion-slip” are very similar to this.

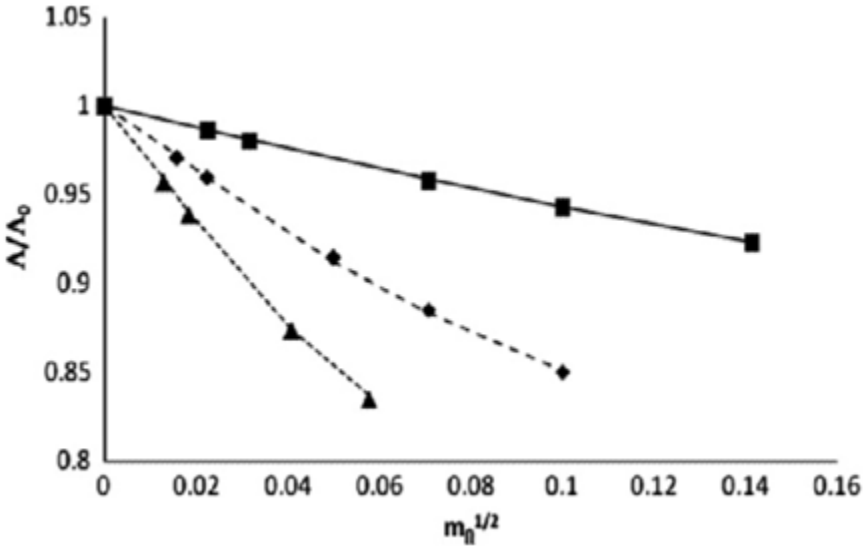

Figure 2-1: Experimental and model equivalent conductance for KCl, $MgCl_2$, and $LaCl_3$. Symbols are from experimental [80] and lines are from “large ion” model with “stick boundary conditions. Other model studies are very similar. Squares, diamonds and triangles correspond to experimental data for KCl, $MgCl_2$, and $LaCl_3$, respectively. The solid line, widely spaced dashed line, and short spaced dashed line correspond to model data for KCl, $MgCl_2$, and $LaCl_3$, respectively.

2.5 Summary and Conclusions

In both the ‘‘small ion” and ‘‘large ion” models considered in this work, solvent and mobile ions are treated as a continuum, and a single ion exclusion distance, a_{ex}, is included in modeling. Particle transport is also being considered in an infinite domain. For the ‘‘small ion” model, it is also assumed that electrostatics are described by the linear Poisson–Boltzmann equation (which strictly limits it to weakly charged ions) and that κa_{ex} is small (limiting it to low

concentration and small size). These latter two assumptions are avoided in the ‘‘large ion” model making it more appropriate for large, highly charged particles. However, the Brownian motion of the central ion is ignored in the ‘‘large ion”, but not the ‘‘small ion” model. In the present work, however, we have proposed an approximate but simple way of correcting for this assumption in the ‘‘large ion” model. Despite these differences in the two models, both are able to reproduce experimental conductivities of dilute binary electrolytes made up of monovalent or polyvalent ions to an accuracy of several tenths of a percent. Minor modifications in the ‘‘large ion” model to include an ion exclusion layer along with the above mentioned correction for Brownian motion allows us to effectively bridge the gap between the two models. These results serve to reinforce both ‘‘small ion” and ‘‘large ion” methodologies as far as application to the electrophoretic mobility and conductivity of small (spherical) ions is concerned. Despite the large absolute electrostatic potentials present when polyvalent ions are present, the use of the linear Poisson-Boltzmann equation in the ‘‘small ion” theory [2, 3, 5–8, 63–70] does not lead to significant errors in conductivity for ions of absolute valence less than or equal to 3. The ‘‘large ion” approach [62,27-30, 48, 75] also works well provided account is taken of the Brownian motion of all ions present. The ‘‘large ion” model can be applied to larger, more highly charged, and also ‘‘structured” particles [37, 38, 40, 53]. As far as small ion studies are concerned, which approach an investigator chooses to use is largely a matter of personal convenience. A more exhaustive comparison of experimental and model conductivities of binary electrolytes shall be presented in future work. The principle objective of the present work has been to present a complete outline of the two approaches and demonstrate their application to three different binary electrolytes of different (cationic) valence.

This work will hopefully stimulate research in several areas. First, both ‘‘small ion” and ‘‘large ion” models have a broader range of applicability than has previously been recognized. Both can be used to study conductivities of not only binary electrolytes, but ternary and more complex solutions. Second, with the growing and widespread use of capillary electrophoresis, both ‘‘small ion” and ‘‘large ion” models can be applied to studies of electrophoretic mobilities. Third, more realistic accounting of the interionic potential of mean force may be considered. Progress in this direction has already been made with regard to the ‘‘small ion” approach [49, 50]

CHAPTER 3

ROTATIONAL DIFFUSION OF MACROMOLECULES AND NANOPARTICLES MODELED AS NON-OVERLAPPING BEAD ARRAYS IN AN EFFECTIVE MEDIUM

3.1 Introduction

The subject of biomolecular transport in congested media is of vital interest in such diverse subjects as drug delivery across membranes and the sieving action of a gel in electrophoresis. In particular, diffusion (translational and rotational) has been studied in a wide range of environments including the cytoplasm of cells [83], concentrated suspensions [84], gels or hydrogels [85-95], and mucus [96]. The diffusion of a host particle through a rigid gel matrix is reduced, relative to diffusion in "free solution", by long range hydrodynamic interaction and short range steric effects. For translational diffusion, these two effects can be considered separately [75, 85, 97, 98]. A simple way of dealing with the contribution of long range hydrodynamic interaction makes use of the Effective Medium (EM) model originally developed by Brinkman [99], and Debye and Bueche [100].

In the EM model, the "fluid" surrounding the particle is treated as a hydrodynamic continuum, and includes both solvent and the "gel" support medium. A special screening term is added to the external force/volume on the fluid in the low Reynolds number Navier-Stokes equation that accounts for the presence of a gel. The resulting equation is what we call the Brinkman equation. Starting from a microscopic model, Felderhof and Deutch were able to derive the Brinkman equation as a mean field approximation [101]. The EM model has been

applied to translational diffusion [85, 86, 97,102], rotational diffusion [101], electrophoresis [76,104], and the electrophoretic stretch of duplex DNA in gels [104,105].

The principle objective of the present work is to extend our earlier study of the translational diffusion of a macromolecule modeled as an array of non overlapping beads in an EM to the case of rotational diffusion. In Section 2.1, the Brinkman equation is introduced and the rotation of a single sphere in an EM is discussed. This is then extended to the more complex problem of an array of non-overlapping beads. In Section 2.2, we focus first on the parameterization of a linear string of touching beads and later extend that to a wormlike chain model. The wormlike chain model is relevant to modeling the electric birefringence or dichroism decay of duplex DNA [94] which is also discussed in Section 2 and again in Section 4. In Section 3.1, the rotational diffusion of some simple bead arrays in the presence and absence of a gel to illustrate the accuracy of the methodology employed as well the influence long range hydrodynamic interaction has rotational diffusion. In Section 3.2, this is applied to the rotational diffusion of a 622 bp DNA fragment in a gel [94]. Here, we are able to compare EM modeling with rotational diffusion in agarose gel measured by electric birefringence. For dilute gels ($\leq$0.01 gm dry gel/ mL solvent), we obtain good agreement between modeling and experiment for reasonable values of model parameters. For more concentrated gels, model rotational relaxation times substantially underestimate experimental relaxation times. This, however, is believed to be due to the neglect of steric interactions in modeling that become important at high gel concentration. In Section 4, the principle conclusions of the present work are summarized.

3.2 Results and Discussion

3.2.1 Transport Theory of Bead Arrays in an Effective Medium

In the Effective Medium, EM, model, the fluid is assumed to obey the Brinkman [77] and solvent incompressibility equations defined by

$$\eta\nabla^2\underline{v}(\underline{r})-\underline{\nabla}p(\underline{r})=\eta\lambda^2\underline{v}(\underline{r}) \qquad (3-1)$$

$$\underline{\nabla}\cdot\underline{v}(\underline{r})=0 \qquad (3-2)$$

Where η is the solvent viscosity, $\underline{v}(\underline{r})$ is the local fluid velocity at point $\underline{r}$, p is the local pressure, and λ (units of 1/length) is the gel screening parameter. This parameter can be related to the gel concentration, M, (in gm dry gel material per gm of solvent) and gel fiber radius, r_f, by the relation [97, 105]

$$\frac{1}{\lambda^2}=\frac{3\rho_g\omega_s r_f^2}{20\mathrm{M}}\left[\ln\left(\frac{\mathrm{M}}{\rho_g\omega_s}\right)+0.931\right] \qquad (3-3)$$

In Equation (3), ρ_g denotes the mass density of dry gel (which equals 1.64 gm/mL for agarose [107]), and ω_s denotes the ratio of dry gel volume to hydrated gel volume (which equals 0.625 for agarose [108]). The term on the right hand side of Equation (3-1) represents an external force/unit volume due to the viscous drag on the fluid produced by the presence of the gel. In general, other external forces on the fluid may be present as well. This is particularly true in modeling the transport of macroions in external electric fields (electrophoresis) [109]. However, the cases of interest in the present work involve rotational relaxation in the absence of an

external electric field. Under these conditions, the additional external force terms can be ignored for a good approximation.

For later reference, it will be useful to consider the local fluid velocity and pressure of a spherical particle of radius "*a*" rotating about its center with angular velocity $\underline{\omega}$ in an EM that is at rest far from the particle. In this case it is straightforward to solve Equations (3-1) and (3-2) and obtain $p(\underline{r})$ = constant and

$$\underline{v}(\underline{r}) = \left(\frac{a}{r}\right)^3 \left(\frac{1+\lambda r}{1+\lambda a}\right) e^{-\lambda(r-a)} (\underline{\omega} x \underline{r}) \qquad (3-4)$$

$$\underline{\underline{\sigma}}(\underline{r}) = -p(\underline{r})\underline{\underline{I}} + \eta\left(\underline{\underline{\nabla v}} + \underline{\underline{\nabla v}}^T\right) \qquad (3-5)$$

In Equation (3-4), "*x*" denotes the vector cross product. Note that the fluid velocity falls off rapidly moving from the rotating sphere. The local stree tensor, $\sigma(\underline{r})$, is related to the velocity and pressure by [73,74]. Where $\underline{I}$ is the 3 by 3 identity tensor ($(\underline{I})_{jk} = \delta_{jk}$ (δ_{jk} is the Kronecker delta)), $(\underline{\nabla v})_{jk} = \nabla_j v_k(\underline{r})$, and $(\underline{\nabla v^T})_{jk} = \nabla_k v_j(\underline{r})$.

For a point $\underline{r} = a\,\underline{n}(\underline{r})$ on the surface of the sphere ($\underline{n}(\underline{r})$ is a local outward (into the fluid) normal to the sphere), the local force/area exerted by the sphere of the fluid,f(r), is related to the local stress by

$$\underline{f}(\underline{r}) = -\underline{\sigma}(\underline{r}) \cdot \underline{n}(\underline{r}) = \eta\gamma(\lambda a)(\underline{\omega} x \underline{n}(\underline{r})) \qquad (3-6)$$

$$\gamma(\lambda a) = \frac{\left(3 + 3\lambda a + \lambda^2 a^2\right)}{(1+\lambda a)} \qquad (3-7)$$

If the sphere were rotating as a rigid body about some point different from its center, then $f(\underline{r})$ would be different. Let $\underline{r}^*$ denote the position of the center of the sphere relative to the center of rotation. For a good approximation, we can write

$$\underline{f}(\underline{r}) \cong \frac{F}{S} + \eta\gamma(\lambda a)(\underline{\omega} x \underline{n}(\underline{r})) \qquad (3-8)$$

In Equation (3-8), $\underline{F}$ denotes the net instantaneous force exerted by the bead on the fluid and $S = 4\pi a^2$ is the surface area of the bead. The net force, in turn, equals $6\pi\eta a(\underline{\omega} x \underline{r}^*)$.

In a recent analysis employing the Boundary Element method, a general expression was derived for the local fluid velocity of an array of non overlapping beads translating with uniform velocity through an Effective Medium that obeys Equations (3-1,3-2) [97]. It is straightforward to extend that analysis to the rotation of a bead array. As illustrated in Figure 1, the macromolecule is modeled as an array of N non overlapping beads in which their radii, $\{a_j\}$, and relative positions are arbitrary. Let $\underline{r}^*$ denote the center of rotation of the rigid body bead array, $\underline{\omega}$ the angular velocity of the bead array, and $\underline{x}_J$ and aJ the centroid position vector and radius of bead J. The fluid is assumed to be at rest far from the array. It shall also be assumed that for a point,

$$\underline{f}(\underline{r}) \cong \frac{\underline{F}_J}{S_J} + \eta\gamma(\lambda a_J)(\underline{\omega} x \underline{n}(\underline{r})) \qquad (3-9)$$

Where $\underline{F}_J$ is the net force exerted by bead J on the fluid andSJ is the corresponding surface area. The second term on the right hand side of Equation (3-9) is similar to the "Volume Correction" approach of Garcia de la Torre and Rodes [110].

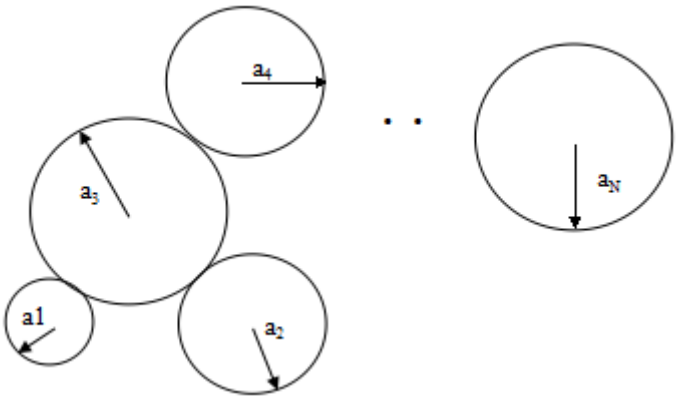

Figure 3-1. Array of N Non Overlapping Beads.
The bead radii, {aj}, and the position of the bead centers is arbitrary.

It is worthwhile to briefly discuss the physical basis of Equation (9). Hydrodynamic interaction, HI, between two beads arises as a consequence of their relative motion through a viscous fluid. In the absence of a gel, the disturbance of the fluid velocity produced by one bead, *J*, centered at $\underline{r}_J$, at the site of a second bead, *K*, centered at $\underline{r}_k$ separated by distance $\underline{r}_{Jk} = |\underline{r}_{Jk}| = |\underline{r}_J - \underline{r}_k|$, falls off as $1/\underline{r}_{Jk}$ if their centers are in relative motion [73,74]. On the other hand, if their centers are not in relative motion, but if one or both beads are rotating about their centers, then the disturbance falls off as $1/\underline{r}_{Jk}^3$, which is clear from Equation (3-4). The presence of a gel modifies these distance dependent interactions, but the important point is that long range HI is determined primarily by the relative translational motion of the bead centers. The dominant long range HI between the beads is contained implicitly in the first term on the right hand side of Equation (3-9). The second term reflects the fluid stress arising from the rotation of bead *J* itself relative to the fluid. It should be emphasized that Equation (3-9) is approximate and ignores shorter range HI interactions.

Following our earlier analysis [97] of a translating bead array, the corresponding results for a rotating bead array can be written

$$\underline{\omega} x\left(\underline{r}_K - \underline{r}^*\right) = \sum_{J=1}^{N}\left[\underline{\underline{C}}_{KJ}\cdot\left(\underline{r}_J - \underline{r}^*\right) + \frac{1}{\zeta_J}\underline{\underline{H}}_{KJ}\cdot\underline{F}_J\right] + \sum_{J=1}^{N}\underline{\omega} x\,\underline{p}_{KJ} \qquad (3-10)$$

$$Where \zeta_J = 6\pi\eta a_J$$

$$\underline{\underline{C}}_{KJ} = \begin{cases} \dfrac{1}{3\lambda a_K}\left[\left(\lambda a_K - 1\right) + e^{-2\lambda a_K}\left(\lambda a_K + 1\right)\right]\underline{\underline{\mathrm{I}}} & (K = J) \\ \dfrac{2}{9}\lambda^3 a_J^3 i_0\left(\lambda a_K\right)\left[i_0\left(\lambda a_J\right)k_0\left(\lambda r_{KJ}\right)\underline{\underline{\mathrm{I}}} + 3 i_2\left(\lambda a_J\right)k_2\left(\lambda r_{KJ}\right)\left[\dfrac{1}{r_{KJ}^2}\underline{\underline{r_{KJ} r_{KJ}}} - \dfrac{1}{3}\underline{\underline{\mathrm{I}}}\right]\right] - \\ \left[\dfrac{1}{3}a_J^3\left(3v_3 - \left(1 + \lambda^2\left(\dfrac{a_K^2}{6} + \dfrac{a_J^2}{10}\right)\right)\right)\left(3w_3 + 3\lambda w_2 + \lambda^2 w_1\right)\right]\left[\dfrac{1}{r_{KJ}^2}\underline{\underline{r_{KJ} r_{KJ}}} - \dfrac{1}{3}\underline{\underline{\mathrm{I}}}\right] & (K \neq J) \end{cases}$$

$$\underline{\underline{\mathrm{H}}}_{KJ} = \begin{cases} i_0\left(\lambda a_K\right)e^{-\lambda a_K}\underline{\underline{\mathrm{I}}} & (K = J) \\ \lambda a_J i_0\left(\lambda a_K\right) i_0\left(\lambda a_J\right)k_0\left(\lambda r_{KJ}\right)\underline{\underline{\mathrm{I}}} + \\ \dfrac{3a_J}{2\lambda^2}\left[3v_3 - \left(1 + \dfrac{\lambda^2\left(a_J^2 + a_K^2\right)}{6}\right)\left(3w_3 + 3\lambda w_2 + \lambda^2 w_1\right)\right]\left[\dfrac{1}{r_{KJ}^2}\underline{\underline{r_{KJ} r_{KJ}}} - \dfrac{1}{3}\underline{\underline{\mathrm{I}}}\right] & \left(K \neq J\right) \end{cases} \qquad (3-12)$$

$$w_n = \frac{e^{-\lambda r_{KJ}}}{r_{KJ}^n} \qquad (3-13)$$

$$v_n = \frac{1}{r_{KJ}^n} \qquad (3-14)$$

$$\underline{\underline{p}}_{KJ} = i_0\left(\lambda a_K\right)\left(\frac{a_J}{r_{KJ}}\right)^3 e^{-\lambda\left(r_{kj} - a_J\right)}\left(\frac{1 + \lambda r_{KJ}}{1 + \lambda a_J}\right)\left(\underline{r}_K - \underline{r}_J\right) \qquad (3-15)$$

In equations (3-11,3-12), i_n and k_n are modified spherical Bessell functions. Specifically, $i_0(z) = \sinh(z)/z$, $i_2(z) = \sinh(z)/z - 3\cosh(z)/z^2 + 3\sinh(z)/z^3$, $k_0(z) = e^{-z}/z$, $k_2(z) = e^{-z}(1/z+3/z^2 + 3/z^3)$. Also, $(r_{KJ}\, r_{KJ})_{jk} = (\underline{r}_K - \underline{r}_J)_j\,(\underline{r}_K - \underline{r}_J)_k$.

The typical procedure followed in a resistance problem [73,754 111-1143], as applied to the more general problem in an EM, is to compute the elements of $\underline{\underline{C}}_{KJ}$ and $\underline{\underline{H}}_{KJ}$ once the geometry of a bead array and conditions of the EM are defined. The bead array is then rotated about three orthogonal axes with unit angular velocity,

$$\underline{\omega}^{(p)} = \underline{e}_p \qquad (3-16)$$

Where $\underline{e}_p$ is a unit vector along axis p (p = 1, 2, or 3) in some convenient frame of reference. Let $\underline{F}_J^{(P)}$ denote the net force exerted by bead J on the fluid when the array is rotated about axis p. Then Equation (10) can be written

$$\sum_{J=1}^{N} \frac{1}{\zeta_J} \underline{\underline{H}}_{KJ} \cdot \underline{F}_J^{(P)} = \underline{A}_K^{(P)} \qquad (3-17)$$

$$\underline{A}_K^{(p)} = \underline{e}_p x\left(\underline{r}_K - \underline{r}^*\right) - \sum_{T=1}^{N}\left[\underline{\underline{C}}_{KJ} \cdot \left(\underline{e}_p x\left(\underline{r}_J - \underline{r}*\right)\right) + \underline{e}_p x \underline{p}_{KJ}\right] \qquad (3-18)$$

It is helpful to view $\underline{F}_J^{(P)}$ and $\underline{A}_K^{(P)}$ as 3 by 1 column vectors. From these, we can define 3N by 3 super matrices, $\underline{\underline{F}}$ and $\underline{\underline{A}}$, by

$$\underline{\underline{F}} = \begin{pmatrix} \underline{F}_1^{(1)} & \underline{F}_1^{(2)} & \underline{F}_1^{(3)} \\ \underline{F}_2^{(1)} & \underline{F}_2^{(2)} & \underline{F}_2^{(3)} \\ \vdots & \vdots & \vdots \\ \underline{F}_N^{(1)} & \underline{F}_N^{(2)} & \underline{F}_N^{(3)} \end{pmatrix} \qquad (3-19)$$

The super matrix, $\underline{\underline{A}}$, has a very similar form to Equation (3-19) above. Also, the $\underline{\underline{\underline{\underline{H}}}}_{KJ}$ terms defined by Equation (3-12) are known 3 by 3 matrices. We can define a 3*N* by 3*N* super matrix, $\underline{\underline{G}}$, by

$$\underline{\underline{G}} = \begin{pmatrix} \underline{\underline{H}}_{11}/\zeta_1 & \underline{\underline{H}}_{12}/\zeta_2 & \cdots & \underline{\underline{H}}_{1N}/\zeta_N \\ \underline{\underline{H}}_{21}/\zeta_1 & \underline{\underline{H}}_{21}/\zeta_2 & \cdots & \underline{\underline{H}}_{2N}/\zeta_N \\ \vdots & \vdots & \ddots & \vdots \\ \underline{\underline{H}}_{N1}/\zeta_1 & \underline{\underline{H}}_{N2}/\zeta_2 & \cdots & \underline{\underline{H}}_{NN}/\zeta_N \end{pmatrix} \qquad (3-20)$$

In compact notation, Equation (3-16) can be written

$$\underline{\underline{G}} \cdot \underline{\underline{F}} = \underline{\underline{A}} \qquad (3-21)$$

The matrix, $\underline{\underline{G}}$, is invertible and let $\underline{\underline{\underline{\underline{G}}}}^{-1}$ denote the inverse. Then

$$\underline{\underline{F}} = \underline{\underline{G}}^{-1} \cdot \underline{\underline{A}} \qquad (3-22)$$

A very similar relation was derived previously for a bead array translating with uniform velocity, before it is possible to compute various resistance tensors from modeling, it is necessary to compute the total force, $\underline{F}_{tot}$, and total torque, $\underline{T}_{tot}(\underline{r}^*)$, exerted by the bead array on the fluid if it is translated with velocity , $\underline{u}$, and rotated with angular velocity, $\underline{\omega}$, about some point, $\underline{r}^*$, in the fluid which is at rest far from the array. In the present work, $\underline{r}^*$ is chosen as the center of mass of the bead array. The total force and torque can be written [114]

$$\underline{F}_{tot} = \underline{\underline{\Xi}}_T \cdot \underline{u} + \underline{\underline{\Xi}}_C^T(\underline{r}^*) \cdot \underline{\omega} \qquad (3-23)$$

$$\underline{T}_{tot}(\underline{r}^*) = \underline{\underline{\Xi}}_C(\underline{r}^*) \cdot \underline{u} + \underline{\underline{\Xi}}_R(\underline{r}^*) \cdot \underline{\omega} \qquad (3-24)$$

Where Ξ_r $\Xi_R(r^*)$ and $\Xi_c(\underline{r}^*)$ denote translation, rotation, and coupling resistance tensors, respectively. Quantities with argument "r", depend on the choice of r^*. Also, the "T" superscript on the coupling tensor in Equation (3-23) denotes transpose. $\underline{F}_{tot}$ and $\underline{T}_{tot}(\underline{r}^*)$ can be obtained by the relationship.

$$\underline{F}_{tot} = \sum_{J=1}^{N} \int_{S_J} dS_r \underline{f}(\underline{r}) = \sum_{J=1}^{N} \underline{F}_J \qquad (3-25)$$

$$\underline{T}_{tot}(\underline{r}*) = \sum_{J=1}^{N} \int_{S_J} dS_r (\underline{r} - \underline{r}*) x \underline{f}(\underline{r}) \qquad (3-26)$$

For a bead array that is not translating (u=0), but is rotating with angular velocity, e_p about r^*

$$\underline{T}^{(p)}(\underline{r}*) = \sum_{J=1}^{N} \left[(\underline{r}_J - \underline{r}*) x \underline{F}_j^{(p)} + \frac{8\pi a_j^3}{3} \eta\gamma(\lambda a_J) \underline{e}_p \right] \qquad (3-27)$$

From Equations (3-23, 3-24), the net force and net torque give the p-th row of $\underline{\Xi}_C$ ($\underline{r}$*) , and *p*-th column of $\underline{\Xi}_R$ ($\underline{r}$*) , respectively. The components of $\underline{\Xi}_T$ are obtained by translating the array along three orthogonal axes, computing the net forces, and then using Equation (3-23).

The connection between the resistance tensors and corresponding mobility or diffusion tensors is well known [73,74,114,115]. The origin dependent translational diffusion tensor, $\underline{D}_T(\underline{r}^*)$, and origin independent rotational diffusion tensor, $\underline{D}_R$, are given by

$$\underline{D}_T(\underline{r}^*) = k_B T \left[\underline{\Xi}_T - \underline{\Xi}_C^T(\underline{r}^*) \cdot \underline{\Xi}_R^{-1}(\underline{r}^*) \cdot \underline{\Xi}_C(\underline{r}^*) \right]^{-1} \qquad (3-28)$$

$$\underline{\underline{D}}_R = k_B T \underline{\underline{\Xi}}_R^{-1} \qquad (3-29)$$

$$\underline{\underline{\Xi}}_R = \left[\underline{\underline{\Xi}}_R\left(\underline{r}^*\right) - \underline{\underline{\Xi}}_C\left(\underline{r}^*\right) \cdot \underline{\underline{\Xi}}_T^{-1} \cdot \underline{\underline{\Xi}}_C^T\left(\underline{r}^*\right)\right] \qquad (3-30)$$

In modeling, the origin independent rotational friction tensor, $\underline{\underline{\Xi}}_R$, can be diagonalized and let Λ_n' (n = 1, 2, or 3) denote the n-th eigenvalue. We shall define the eigenvalues such that $\Lambda_1' \geq \Lambda_2' \geq \Lambda_3'$. Also define the reduced dimensionless eigenvalue for an array of N identical beads of radius a,

$$\Lambda_n = \frac{\Lambda_n}{8\pi\eta a^3 N} \qquad (3-31)$$

The denominator in Equation (3-31) represents the rotational friction factor of a sphere of volume equal to that of our bead array.

The modeling results of the present work shall be given in terms of these dimensionless eigenvalues. These, in turn, can be related to the eigenvalues of $\underline{\underline{\Xi}}_R$ and $\underline{\underline{D}}_R$ through Equations (3-48,3-87). We also want to relate these to the longest lifetime, τ_1, of the "off-field" electric birefringence decay of a dilute solution of macromolecules. We can write [94,116]

$$\tau_1 = \frac{1}{6D_{R1}} = \frac{4\pi\eta a^3 N}{3k_B T}\Lambda_1 \qquad (3-32)$$

3.2.2 Modeling the Rotation of Linear Macromolecules as Strings of Identical Touching, but Non-Overlapping Beads

A key element in the parameterization of the bead radii of our "coarse grained" models is to find arrays of identical beads that are able to reproduce the rotational friction, $\underline{\underline{\Xi}}_R$, or diffusion, $\underline{\underline{D}}_R$, tensor of the actual structure to considerable accuracy. From Section 2.1, this is equivalent to matching the reduced eigenvalues, $\{\Lambda_n\}$. Furthermore, since experiments such as electric birefringence [95, 117] or dichroism [117,118] are sensitive to particular eigenvalues (Λ_1 for example), then we can focus on matching that particular eigenvalue.

This shall be illustrated for the special case of a right circular cylinder of length L and axial radius, R. For the right circular cylinder in an EM with $\lambda = 0$ [119]

$$\Lambda_1^{rod}(L,R) = \frac{L^2}{18R^2\left[\ln(p) + \delta_\perp(p)\right]} \qquad (3-33)$$

$$p = \frac{L}{2R} \qquad (3-34)$$

$$\delta_\perp(p) = -0.662 + 0.917/p - 0.050/p^2 \qquad (3-35)$$

For the corresponding array made up of a linear string of N touching beads of radius a, we shall set

$$L = 2a(N - c) \qquad (3-36)$$

In Equation (36), a and c are left as adjustable parameters but it is assumed that a is proportional to R. For an array made up of N beads, Λ_1 from Equation (31) is independent of η

and a, and is computed by the procedure described in Section 2.1. The quantity Λ_1^{rod} from Equation (33) is independent of η and only depends on the ratio, L/R, or equivalently L/a. For assumed values of a and c, Equation (36) then gives us a direct correspondence between L, N, a, and c. It is straightforward to construct an Excel spreadsheet in which a and c are defined as input parameters. Λ_1^{rod} and Λ_1 are compared for a range of N values. (In the present work, we are interested in long rods and N is varied from 20 to 100). In the fitting procedure, we start by setting c equal to 0 and then vary a until the sum of the square of the differences, SR, between Λ_1^{rod} and Λ_1 is minimized. Then, c is incremented by a small amount and the procedure is repeated. This process is continued until that combination of a and c is found that minimizes SR overall. For a good approximation, this is given by $c = 0.20$ and $a/R = 1.20$. We can apply this duplex DNA made up of n_{bp} base pairs and L (in nm) = $0.34\, n_{bp}$. Also, R is 1.0 ± 0.1 [120] and this parameter shall be set equal to 1.0 nm in the present work. This model is very similar to that of Hagerman and Zimm [121] and involves minor corrections in the choice of the a and c parameters. Unless the duplex DNA is very short, however, it is better to model the DNA as a wormlike chain of persistence length P (contour length equal to L and axial radius equal to R) rather than a right circular cylinder. For DNA, P is typically in the 50 nm size range, but this varies with ionic strength [122,123]. As an illustrative example, $L = 211.5$ nm for 622 bp DNA which is more than 4 persistence lengths long. Also, for $a = 1.206$ and $c = 0.20$, Equation (36) requires N be set to 88. For DNA fragments of this size, a rigid rod model is inadequate. Fortunately, it is straightforward to generalize the "linear string" model of the previous paragraph to a "discrete wormlike chain" model that has been widely used in the past [121,124]. Let $\langle \cos\theta \rangle = \langle \underline{e}_J \cdot \underline{e}_{J+1} \rangle$ where $\underline{e}_J$ denotes the unit vector along the J-th virtual bond of our

discrete wormlike chain model and brackets denote an ensemble or long time average. If the distance between adjacent beads is $2a$, then [121,122,124]

$$P = \frac{2a}{1 - \langle \cos\theta \rangle} \qquad (3-37)$$

Using random number generators, it is straightforward to generate chains that satisfy this condition [121,124]. Since overall conformational features, such as end to end distances, vary greatly from one randomly generated chain to another (when L is significantly larger than P), it is necessary to average transport results over many different chains in order to obtain good statistics.

At this point, we can ask whether or not it is reasonable to equate average transport properties, such as $<\Lambda_1>$, derived from model studies of ensembles of chains "frozen" in their starting configuration, to the actual transport properties of flexible particles. The answer to this question depends, in part, on what is actually measured in a particular experiment. Considerable attention to this point has been given to the "off field" electric birefringence or dichroism decay of duplex DNA [94,116,117,121]. In general, the decay is multi-exponential and consists of end over end tumbling as well as more complex "internal" decay processes [125]. However, provided we are interested in the *slowest* decay process, which is also the decay process of greatest amplitude for comparatively short DNA fragments, equating Λ_1 in Equation (32) to the average, $<\Lambda_1>$, obtained from an ensemble of "frozen" chains, is expected to be an accurate approximation [125].

3.2.2 End-Over-End Rotation of Rods

Figure 3.2 illustrates the equivalence between the "end-over-end" reduced rotational friction coefficient, Λ_1, of a right circular cylinder and a linear string of touching beads in the absence of a gel ($\lambda = 0$). The solid line represents the right circular cylinder of length L and axial radius R and is computed from Equation (33) [119]. The filled squares, computed using the procedure described in Section 2.1, are for a linear string of N touching beads of radius a with $a/R = 1.207$. The length, L is related to a and N by Equation (36) with $c = 0.20$.

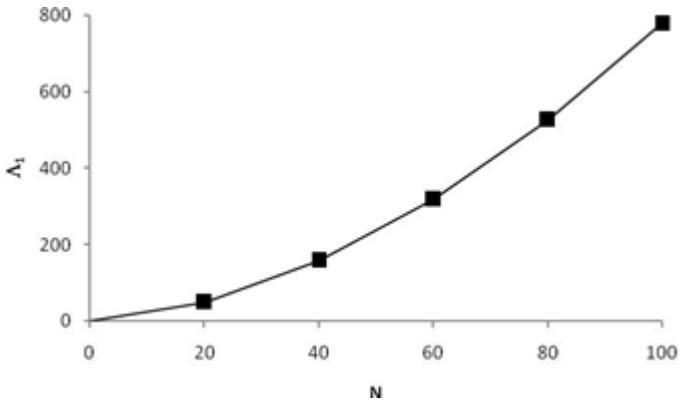

Figure 3-2. Λ_1 for a right circular cylinder and linear string of touching beads versus length. The solid line is for a right circular cylinder of axial radius R and comes from Equation (33) [95]. The filled squares are for a linear string of touching beads of radius a and $a/R = 1.207$. The length of the right circular cylinder, L, is related to N and a by Equation (36) with $c = 0.20$. The gel screening parameter, □, is set to zero (no gel).

We would next like to consider the effect of the gel on Λ_1. For a sphere of radius a in an EM, it is straightforward to show (using Equations (65,66,82,84)), that

$$\frac{\Lambda_1}{\Lambda_1^{ng}} - 1 = \frac{\lambda^2 a^2}{3(1+\lambda a)} \qquad (3-38)$$

where Λ_1^{ng} is the reduced friction factor for a rotating sphere in the absence of a gel (which equals $8\pi\eta a^3$). For a linear string of touching beads (radius = a), we computed Λ_1 for N ranging from 20 to 100 and λa ranging from 0 to 0.604 using the procedure described in Section 3.2.1. To within an accuracy of ±2% over the entire range of N and λa, the data can be fit with the following simple semi-empirical form:

$$\frac{\Lambda_1}{\Lambda_1^{ng}} - 1 = d_1 x^2 + d_2 x^3 \qquad (3-39)$$

$$x = \ln(1+\gamma) \qquad (3-40)$$

$$\gamma = \lambda R_e = \lambda a\left(N\Lambda_1^{ng}\right)^{1/3} \qquad (3-41)$$

$$d_1 = 0.534 - 0.049\ln(N) - 0.004(\ln(N))^2 \qquad (3-42)$$

$$d_2 = -0.001 \qquad (3-43)$$

Above, Λ_1^{ng} represents the reduced eigenvalue of the bead array in the absence of a gel (λ = 0), and R_e is the radius of a sphere that has the same reduced rotational friction coefficient as the bead array in the absence of a gel.

3.3 Experimental Section: Rotational Relaxation of DNA in a Dilute Agarose Gel

Stellwagen [94] has reported longest lifetime, τ_l, "off field" electric birefringence decays of 622 base pair DNA in dilute agarose gels with M varying from 0 to 0.015 gm "dry" gel/mL. The experiments were carried out at 20 °C in 0.2 mM aqueous Tris buffer at a pH of around 8.0. A discrete wormlike chain model consisting of 88 touching beads was used to model 622 bp

DNA following the procedure discussed in Section 3.2.2. Figure 3-3 shows a representative discrete wormlike chain comprised of 88 beads with P = 65 nm. For structures such as these, reduced rotational eigenvalues, Λ_1^{exp}, corresponding to reported lifetimes, τ_1, can be determined using Equation (3-32). The relative uncertainty in these experimental numbers is estimated to be approximately 3%. For each simulation, 300 wormlike chain configurations were generated at random and an average Λ_1 was computed. We chose 300 configurations in order to obtain relative model uncertainties in $<\Lambda_1>$ that are accurate to about 3%.

Figure 3-3 A 88 Subunit Discrete Wormlike Chain.

The persistence length,P, is 65 nm and the bead radius,a, is 1.207 nm. Different configurations are generated at random as discussed in the text.

There are two model parameters that need to be determined and they are the persistence length of the DNA, P, and the average gel fiber radius, r_f (see Equation (3-3)). P can be determined by varying this quantity in modeling until Λ_1^{exp} and $<\Lambda_1>$ match (94). In the absence of a gel, Λ_1^{exp} is best fit by setting P = 65 nm in modeling. This value is in good agreement with experiment when the comparatively low salt conditions of the experiment are factored in [123]. Under physiological salt conditions, a value of P of around 50 nm is expected.

Figure 4 summarizes our comparison of Λ_1^{exp} and model Λ_1. Filled squares denote experimental values and the solid, dotted, and dashed lines represent r_g = 1.52, 2.0, and 2.5 nm, respectively. X-ray diffraction studies of agarose indicate a significant population of fibers with r_g of about 1.52 nm, but a fraction of significantly thicker fibers [126]. This motivated the choice of 1.52 nm. The choice of the higher values comes from fitting the electrophoretic mobility of Au nanoparticles in agarose gels [75]. From Figure 4, a gel fiber radius of about 2.5 nm appears to be most consistent with experiment. Although this r_g value along with P = 65 nm for DNA appears to describe well the rotational relaxation behavior of DNA in dilute gels ($M \leq 0.10$ gm "dry" gel/mL), it substantially underestimates the rotational lifetimes in more concentrated gels.

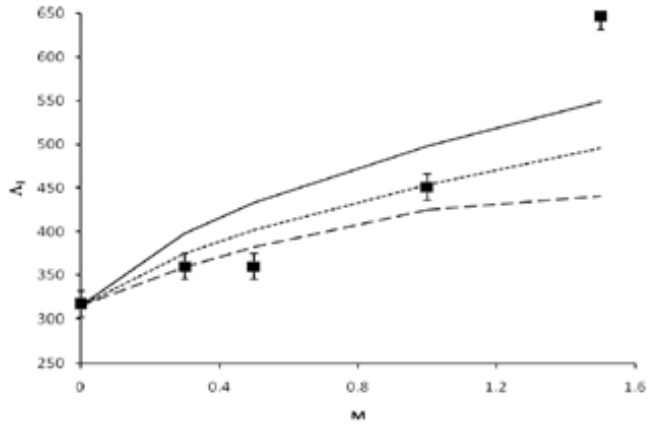

Figure 3.4 Model and Experimental Λ_1 Values for 622 bp DNA as a Function of Gel Concentration. Experimental values are denoted by the filled squares. Solid, dotted, and dashed lines denote model studies with P = 65 nm and rg = 1.52, 2.0, and 2.5 nm, respectively. The temperature is 20 ºC.

Experimental values are denoted by the filled squares. Solid, dotted, and dashed lines denote model studies with P = 65 nm and r_g = 1.52, 2.0, and 2.5 nm, respectively. The temperature is 20 °C.

The EM model that we have used accounts for long range hydrodynamic interactions, HI, but ignores direct interactions. If a characteristic length of our macromolecule is much smaller than the average spacing between gel fibers, *A*, then direct interactions would not be expected to significantly retard the random rotational motion of our macromolecule. For flexible duplex DNA modeled as a wormlike chain, we can set this "characteristic length" equal to the persistence length, *P*. If a dilute gel is modeled as a simple cubic lattice of gel fibers, then [127]

$$A \cong r_g \sqrt{\frac{3\pi\rho_g\omega_s}{M}} \qquad (3-44)$$

See the discussion following Equation (3-3) for the definitions of ρ_g and ω_s and their values for agarose. If we set r_g equal to 2.5 nm, then A = 142, 110, 78, and 63 nm for M = 0.003, 0.005, 0.010, and 0.015 gm/mL, respectively. It is important to note that A decreases with increasing M and becomes comparable to P for M in the 0.010 to 0.015 range. For $M \leq 0.010$ gm/mL, the gel fiber spacing is comparatively large and long range hydrodynamic interaction is the dominant interaction. For $M > 0.010$ gm/mL, however, direct interactions become important.

3.4 Conclusions

The objective of the present study is to apply the Effective Medium (EM) model to the rotational motion of a macromolecule modeled as an array of non-overlapping beads and then apply it to several cases including duplex DNA in agarose gels. This is an extension of earlier work which focused on the translational motion of similar model macromolecules in an EM [97]. The presence of a gel retards the rotational motion of a particle in a gel and this retardation is due

to both long range hydrodynamic interaction, HI, and (short range) direct interactions. EM modeling accounts for long range HI, but not direct interactions. The EM modeling procedure is used to examine the electric birefringence decay of a 622 base pair DNA fragments in an agarose gel [94]. At low gel concentration ($M \leq 0.010$ gm/mL) where long range interactions dominate, good agreement between theory and experiment is achieved if the persistence length, P, of DNA is taken to be 65 nm and the gel fiber radius, r_g, of agarose is taken to be 2.5 nm. A persistence length of this magnitude is consistent with independent studies [123]. Also, a gel fiber radius of 2.5 nm is consistent with earlier modeling studies of DNA diffusion [97] as well as the electrophoresis of Au nanoparticles [75] in agarose gels. At higher gel concentrations, the EM model substantially underestimates the rotational relaxation time of DNA. By means of simple modeling, we have shown that short range interactions become important when the average gel fiber spacing, A, becomes comparable to P.

It has been recognized for some time that the behavior of macromolecules in gel electrophoresis fall into well defined "regimes" [128], and the findings of the present study are consistent with this view. At low gel concentration where long range HI dominates, the EM model is adequate, but this breaks down at high gel concentration where reptation theories are undoubtedly more appropriate [129]. In the case of rotational motion, it appears as though the transition between "long range" and "short range" regimes occurs over a narrow interval of gel concentration and that the nature of this rotational motion could be very different in the two regimes. More experimental and modeling studies are required to address this issue. It would also be possible to extend these studies to circular duplex DNA in gels as a function of linking number [130]. Conformations could be generated using established Brownian dynamics

procedures [109,124,130] followed by application of the methodology of the present work to account for the long range hydrodynamic effect of the gel.

CHAPTER 4

MODELING THE ELECTROPHORESIS OF HIGHLY CHARGED PEPTIDES: APPLICATION TO OLIGOLYSINES

4.1 Introduction

Capillary electrophoresis provides a powerful means of separating and characterizing peptides in aqueous solution as discussed in a number of reviews [12-15,131]. Over the last few years, we have developed and applied a coarse grained bead modeling methodology, BMM, to a range of peptide systems in an attempt to characterize them with respect to charge, conformation, and possibly specific interactions with components of the background electrolyte, BGE [42-44, 54,132]. This is a structure based methodology grounded on fundamental continuum electro hydrodynamic theory. A peptide made up of n amino acids is modeled as 2n non-overlapping beads and account can be taken of both peptide primary and secondary structure [44]. Until now, electrostatics in the BMM approach, with the exception of the "large ion" relaxation correction [133], have been treated at the level of the linear Poisson-Boltzmann, LPB, equation. Provided the peptides are weakly charged, this is expected to be a reasonable approximation of electrostatics. This would include, for example, oligoglycines and oligoalanines [53]. For more highly charged peptides such as oligoglutamic acids or oligolysines, on the other hand, a more accurate treatment of electrostatics involves the nonlinear PB, NLPB, equation.

Considerable interest in using solutions of the NLPB equation to describe the electrostatics around highly charged macroions developed in the 1980s when a number of groups investigating ionic distributions around high molecular mass duplex DNA showed that the NLPB equation gives accurate electrostatic potentials and ion distributions provided that co and counterions are univalent and small compared to the diameter of DNA [134-136]. Both

"Cartesian mesh" [137-139] and boundary element, BE, numerical procedures [110,140] have been developed and applied to rigid model macroions in general. Recently, an approximate numerical procedure was developed and applied to arrays of non-overlapping beads [141]. In the present work, we improve upon this procedure in order to obtain more accurate potentials. Furthermore, we modify the BMM procedure to include this more accurate treatment of electrostatics.

In section 2, we give a brief outline of the BMM. The refinements made due to the more accurate treatment of electrostatics are discussed at some length in subsection 2.2. The new procedure shall be called NLPB-BMM. In section 3, the NLPB-BMM is used to characterize the electrophoretic mobility of low molecular mass oligolysines in aqueous Li-phosphate buffer at pH = 2.5 over a range of different ionic strengths, I, and absolute temperatures, T. At low ionic strength and temperature, good agreement between modeling and experiment is achieved. However, as I and T increase, agreement gets worse. One possible explanation for this is the onset of specific binding between the oligolysines and phosphate counterions. Section 4 summarizes the principle conclusions of this work.

4.2 Materials and Methods

4.2.1 Experiments and Modeling Background

The experimental mobilities of oligolysines in lithium phosphate BGE at different temperatures have been reported previously [10] and this data shall be used in the present analysis. Experimental mobilities have been corrected for electroosmotic flow as well as Joule heating. Modeling of weakly charged peptides has been described in detail previously [42-44,54,132], and much of that development can also be applied to highly charged peptides. In the

present work, the underlying modeling is only briefly described. Modifications in the methodology to deal with the problem of highly charged peptides are discussed at length in section 2.2.

In the bead modeling methodology, BMM, each amino acid of a peptide is modeled as 2 beads with one bead of constant radius (0.19 nm representing the backbone connecting neighboring alfa carbons which are separated by a distance 0.38 nm) and a side bead of variable radius. The side bead radii are parameterized on the basis of the translational diffusion constant of the corresponding amino acid [142]. Random numbers are used to generate phi-psi angles over restricted ranges in order to account for local secondary structure of the model peptides [44]. In the present work, it is assumed that the oligolysines are in a "random" secondary structure. In each modeling study (of a particular oligolysine at a particular temperature and ionic strength), 50 independent conformations are generated and the mobilities of individual conformations are averaged. To compute the correction for the "relaxation effect", we employ the "large ion" approach described in Section 2.5 of our earlier work. However, we use the reduced "zeta" potential averaged over the surface of all beads making up the model peptide at the level of the nonlinear PB rather than the linear PB equation.

4.2.2 Accounting for Electrostatics at the Level of the Nonlinear PB Equation

Previously, a preliminary algorithm was developed to numerically solve the full Poisson Boltzmann equation within the Boundary Element formalism [141]. In the present work, a major objective is to expand upon this in two ways. First of all, solve for the equilibrium potential more accurately by avoiding the "pre averaging" approximations made earlier. Second, incorporate these charges in the BEM with regards to calculating the electrophoretic mobility of model

structures. In the course of implementing the second objective above, we found it necessary to obtain accurate electrostatic potentials.

It shall be assumed that our macroion, modeled as an array of nonoverlapping beads, is present in sufficient dilution so that macroion-macroion interactions can be neglected. The medium surrounding the macroion is modeled as an electrodynamic and hydrodynamic continuum and macroion-wall interactions are neglected. In the present work, a gel, modeled as an effective medium, EM, can also be included [143]. However, application in the present work shall be restricted to "free solution". In addition to the dilute macroions, background electrolyte, BGE, of ionic strength I (in $moles/L$) is also present. Furthermore, let z_α and $c_{\alpha 0}$ denote the valence charge and ambient concentration (in $moles/L$ of species α of the BGE. Also, let $\Lambda_0(s)$ denote the local equilibrium electrostatic potential at point $\underline{s}$ in the fluid domain exterior to the bead array.

Let $\underline{\phi}(s) = e\Lambda_0(s)/k_BT$ denote the corresponding dimensionless electrostatic potential where e is the fundamental charge, k_B is the Boltzmann constant, and T is absolute temperature. From Eq. (26) of I,

$$\phi(\underline{s}) = -\kappa^2 \int_{V_e} f(\underline{x},\underline{s})\, g(\underline{x})\, dV_x + \frac{1}{2}\sum_{k=1}^{N} \phi_k s(\kappa a_k)\, k_0(\kappa r_k) + \omega \sum_{k=1}^{N} z_k i_0(\kappa a_k) k_0(\kappa r_k) \qquad (4-1)$$

In Eq. (4-1), N is the number of beads in the array, a_k is the radius of bead k, z_k is the valence charge of bead k located at its center (point $\underline{x}_k$ in some convenient reference frame),

ϕ_k is the dimensionless potential averaged over the surface of bead k, V_e is the fluid volume exterior to the bead array,

$$\kappa = F\sqrt{\frac{2I}{\varepsilon_0 \varepsilon_r RT}} = 5.028\times 10^{11}\sqrt{\frac{I}{\varepsilon_r T}} \qquad (4-2)$$

$$I = \frac{1}{2}\sum_{\alpha} c_{\alpha 0} z_{\alpha}^2 \qquad (4-3)$$

$$r_k = \left|\underline{s} - \underline{x}_k\right| \qquad (4-4)$$

$$f(\underline{x},\underline{s}) = \frac{e^{-\kappa\left|\underline{x}-\underline{s}\right|}}{4\pi\left|\underline{x}-\underline{s}\right|} \qquad (4-5)$$

$$g(x) = -(\phi(x) + \sum_{\alpha} m_{\alpha} z_{\alpha} e^{-z_{\alpha}\phi(x)}) \qquad (4-6)$$

$$m_{\alpha} = \frac{c_{\alpha 0}}{2I} \qquad (4-7)$$

$$\omega = \frac{\kappa e^2}{4\pi\varepsilon_0 \varepsilon_r k_B T} \qquad (4-8)$$

$$i_0(z) = \frac{\sinh(z)}{z} \qquad (4-9)$$

$$k_0(z) = \frac{e^{-z}}{z} \qquad (4-10)$$

$$s(z) = e^{z}(z-1) + e^{-z}(z+1) \qquad (4-11)$$

In the above equations, F is the Faraday constant, κ is the Debye-Huckel screening parameter (in 1/cm), ε_0 is the permittivity of free space, ε_r is the relative permittivity of the solvent, R is the ideal gas constant, m_a is a dimensionless mobile ion concentration, and ω is a dimensionless constant that depends on temperature, solvent, and properties of the BGE.

As in reference [141], V_e is subdivided into N domains and let V_{ej} denote the fluid domain closer to bead j than any other bead. This is illustrated in Figure 4-1. Choosing the origin to be centered at $\underline{x}_j$ (center of bead j), we can define the average potential a distance s from j by

$$\phi_j(s) = \frac{1}{\Omega_j(s)} \int d\Omega_s \, \phi(\underline{s}) \, \theta'_j(\underline{s}) \qquad (4-12)$$

The integration in Eq. (4-12) is over 4π steradians and $\theta'_j(\underline{s})$ equals 1 if $\underline{s}$ lies within V_{ej} and 0 otherwise. Also

$$\Omega_j(s) = \int d\Omega_s \, \theta'_j(\underline{s}) \qquad (4-13)$$

For a particular $\underline{s}$, it is numerically straightforward to evaluate $\theta'_j(\underline{s})$ for all j by simply evaluating distance between $\underline{s}$ and all the beads. The quantity $\Omega_j(s)$ can vary from 4π at s=a_j (all points are chosen to bead j than any other bead) and 0. The latter possibly arises when bead j has many neighboring beads and these exists a certain critical distance, s_j^*, beyond which $\Omega_j(s)$ equals zero. Under these conditions, we are free to set $\phi_j(s) = 0$ in Eq. (4-12) since such points do not ultimately enter into the calculation.

The first term on the rhs of Eq. (4-1) can be written

$$-\kappa^2 \int_{V_e} f(\underline{x},\underline{s})\, g(\underline{x})\, dV_x = -\frac{\kappa^3}{4\pi} \sum_{k=1}^{N} \int_{a_k}^{\infty} x^2 dx\; g_k(x) \int d\Omega_x \theta_k^{'}(\underline{x}) k_0(x) \left| \underline{x} + \underline{x}_{kj} - \underline{s} \right| \qquad (4-14)$$

$$g_k(x) = -(\phi_k(x) + \sum_{\alpha} m_\alpha z_\alpha e^{-z_\alpha \phi_k(x)}) \qquad (4-15)$$

$$\underline{x}_{kj} = \underline{x}_k - \underline{x}_j \qquad (4-16)$$

Next, define the following terms

$$a_{kj}(s) = \frac{1}{\Omega_j(s)} \int k_0(\kappa \left| \underline{s} - \underline{x}_{kj} \right|)\, \theta_j^{'}(\underline{s})\, d\Omega_s \qquad (4-17)$$

$$b_{kj}(x,s) = \frac{1}{4\pi\Omega_j(s)} \iint d\Omega_x\, d\Omega_s \theta_k^{'}(\underline{x}) \theta_j^{'}(s) k_0(\kappa \left| \underline{x} + \underline{x}_{kj} - \underline{s} \right|) \qquad (4-18)$$

$$H_{kj}^{'}(s) = \kappa^3 \int_{a_k}^{\infty} x^2 dx\; g_k(x) b_{kj}(x,s) \qquad (4-19)$$

$$d_k = \frac{1}{2} \phi_k s(\kappa a_k) + \omega z_k i_0(\kappa a_k) \qquad (4-20)$$

With these definitions and Eq. (4-14) multiply Eq.(4-1) by $\theta_j^{'}(\underline{s})$, integrate over $d\Omega_s$ and divide by $\Omega\ (s)$ (subject to the condition $\Omega_j(s) > 0$). This yield

$$\phi_j(s) = \sum_{k=1}^{N} [d_k\, a_{kj}(s) - H_{kj}^{'}(s)] \qquad (4-21)$$

In the limit $s \to a_j$, $\phi_j(s) \to \phi_j$ and $a_{kj}(s) \to k_0(ka_j)$ for j=k and $i_0(ka_j)k_0(kx_{jk})$ for $j \neq k$ $x_{jk} = |\underline{x}_j - \underline{x}_k|$)

Let

$$A_{jk} = \begin{cases} 1 - \frac{1}{2} s(ka_j) k_0(ka_j) & (j = k) \\ -\frac{1}{2} s(ka_k) i_0(ka_j) k_0(kx_{jk}) & (j \neq k) \end{cases} \qquad (4-22)$$

$$\gamma_j^0 = \omega z_j i_0(\kappa a_j) k_0(\kappa a_j) + \omega \sum_k z_k i_0(\kappa a_k) i_0(\kappa a_j) k_0(\kappa x_{jk}) \qquad (4-23)$$

$$\gamma_j = \gamma_j^0 - \sum_{k=1}^{N} H_{kj}^{'}(a_j) \qquad (4-24)$$

With these definitions and taking the limit $s \to a_j$, Eq. (4-21) can be written

$$\sum_{k=1}^{N} A_{jk} \phi_k = \gamma_j \qquad (4-25)$$

This can be put in matrix form. Let $\underline{\underline{A}}$ denote the N by N matrix with $(\underline{\underline{A}})_{jk} = A_{jk}$. Also, let ϕ and γ_j denote N by 1 column vectors. The matrix, $\underline{\underline{A}}$, is invertible and let $\underline{\underline{A}}^{-1}$ denote this inverse. Then Eq. (4-25) can be written

$$\underline{\phi} = \underline{\underline{A}}^{-1} \cdot \underline{\gamma} \qquad (4-26)$$

As in reference [141], this must be solved iteratively. Since the $\{\phi_k\}$ and $\{\phi_k(x)\}$ appear implicitly in the γ_k terms (see Eq.(4-15),(4-19), (4-20) and (4-24)) . The exponential in Eq. (4-15) is expanded

$$g_k(x) = \sum_{p=2}^{\infty} e_p (\phi_k(x))^p \qquad (4-27)$$

$$e_p = \sum_{\alpha} \frac{m_\alpha (-z_\alpha)^p}{p!} \qquad (4-28)$$

If $|\phi_k(x)|$ is small, then $g_k(x)$ is small and $H'_{kj}(s)$ can be ignored (see Eq. (4-19)) and $r_j \cong r_j^0$. We shall follow the approach of initially ignoring $g_k(x)$ and approximate r_j with r_j^0 . For successive iteration we use previous estimates of $\{\phi_k\}$ and $\{\phi_k(x)\}$ and approximate Eq. (4-27) with

$$g_k(x) = \sum_{p=2}^{p_{\max}} e_p (\phi_k(x))^p \qquad (4-29)$$

Initially, $p_{\max}$ is set to 3. For a particular $p_{\max}$, Eq. (4-26) is solved iteratively for $\{\phi_k\}$ until they converge. Once this is achieved, $p_{\max}$ is raised by 1 (or 2) and the process is repeated. When $p_{\max}$ exceeds a certain value (typically 15), converged $\{\phi_k\}$ becomes independent of $p_{\max}$ and at that point, the calculation is stopped.

Since this iterative procedure initially starts with $\{\phi_k\}$ that are far from these full converged values, it is necessary to slightly modify the procedure just described in order to prevent unphysical divergence of the reduced potentials. Let $H'^{(n)}_{kj}(s)$ denote the value of $H'_{kj}(s)$ given by Eq.(4-19) after the n-th iteration. Also let using $g_k^n(x)$ be given by Eq.(4-29) using potentials from the n-th iteration. For iteration n+1, we compute

$$H'^{*}_{kj}(s) = \kappa^3 \int_{a_k}^{\infty} x^2 dx \, g_k{}^{(n)}(x) b_{kj}(x,s) \qquad (4-30)$$

To avoid divergence, we set

$$H_{kj}^{'(n+1)}(s)=H_{kj}^{'(n)}(x)+\theta(H_{kj}^{'*}(s)-H_{kj}^{'(n)}(s)) \qquad (4-31)$$

In Eq.(4-31), θ is a relaxation parameter that is typically set in the 0.10 to 0.25 range. With little difficulty, it can be adjusted automatically in the program to be just small enough to avoid divergence.

The algorithm described above is a generalization of the procedure described in reference [141]. The "pre averaging" approximations of this earlier work are avoided.

Nonlinear charge effect also influence the external force/volume $s_e(x)$, at point $\underline{x}$ in the fluid. In the present work, it shall be assumed: (1) external force arises from the interaction of a valence external electric field, $\underline{e}_0$, with the local (equilibrium) charge density in the fluid, $\rho_0(x)$; (2) the equilibrium charge distribution in the fluid is treated as a continuum and is adequately described by the nonlinear Poisson-Boltzmann equation. Under these conditions, the external force/volume is given by

$$s_e(\underline{x})=\rho_0(\underline{x})\underline{e}_0=2IF\underline{e}_0\sum_\alpha z_\alpha m_\alpha e^{-z_\alpha\phi(\underline{x})}=\frac{\kappa^2\varepsilon_0\varepsilon_r k_B T}{e}\underline{e}_0\sum_\alpha z_\alpha m_\alpha e^{-z_\alpha\phi(\underline{x})} \qquad (4-32)$$

In evaluating the "force balance" of a bead away in an effective medium, EM, characterized by gel screening parameter, λ, the Brinkmann equation can be written [104]

$$\underline{\nabla}\cdot\underline{\underline{\sigma}}_H(\underline{x})=-\underline{s}_e(\underline{x})+\eta\lambda^2\underline{v}(\underline{x}) \qquad (4-33)$$

In Eq.(4-33), $\underline{\underline{\sigma}}_H$ is the hydrodynamic stress tensor, η is the solvent velocity, and $\underline{v}$ is the local fluid velocity in a reference frame where $\underline{v}=0$ far from the particle.

Starting from the Lorentz Reciprocal Theorem [74,75] combined with the singular solution of the Brinkman equation [74,75],it can be shown,

$$[22](\underline{\underline{\chi}}_k - \frac{1}{2}\sum_{j=1}^{N}\underline{\underline{W}}_{kj}^{(3)} \cdot \underline{\underline{d}}_j^{'}) \cdot \underline{\underline{\mu}} = \frac{e\kappa}{6\pi\eta}\sum_{j=1}^{N}[\underline{\underline{W}}_{kj}^{(1)} \cdot \underline{g}_j - \frac{d_j}{2\omega}\underline{\underline{W}}_{kj}^{(2)} - \underline{\underline{T}}_{kj}] \qquad (4-34)$$

The term of ultimate interest in modeling is the electrophoretic mobility tensor of our bead array, μ. Most of the terms in Eq. (4-34) have been described in detail previously [22] and for the sake of brevity, shall not be described again here. What is new in Eq. (4-34) is the term $\underline{\underline{T}}_{kj}$ on the far right hand side of the equation. This represents the contribution of nonlinear charge effects in Eq. (4-32). It can be written

$$\underline{\underline{T}}_{kj} = \frac{\kappa^3}{4\pi\omega}\int_{V_{ej}} dV_x \underline{\underline{U}}^{'}(\underline{r}_{kj}^{'})(g_j(x) + \phi_j^{near}(x)) \qquad (4-35)$$

$$\underline{r}_{kj}^{'} = \underline{x} + \underline{x}_j - \underline{x}_k \qquad (4-36)$$

$$\underline{\underline{U}}^{'}(\underline{r}) = \frac{[\kappa^3 k_0(\kappa r) - \lambda^3 k_0(\lambda r)]}{\kappa(\kappa^2 - \lambda^2)}\underline{\underline{I}} - \frac{3\kappa^2}{2(\kappa^2 - \lambda^2)}[(\frac{3}{\kappa^3}\omega_3 + \frac{3}{\kappa^2}\omega_2 + \frac{1}{\kappa}\omega_1) - \frac{\lambda^3}{\kappa^3}(\frac{3}{\lambda^3}\omega_3^{'} - \frac{3}{\lambda^2}\omega_2^{'} + \frac{1}{\lambda}\omega_1^{'})\underline{\underline{N}} \qquad (4-37)$$

$$\omega_n = e^{-\kappa r}/r^n \qquad (4-38)$$

$$\omega_n^{'} = e^{-\lambda r}/r^n \qquad (4-39)$$

$$\underline{\underline{N}} = \underline{r}\underline{r}/r^2 \qquad (4-40)$$

$$\phi_j^{near}(x) = \sum_k d_k(a_{kj}(x) - k_0(\kappa r_k^{'})) - \sum_k H_{kj}^{'}(x) \qquad (4-41)$$

In Eq. (4-37), $\underline{\underline{I}}$ is the 3 by 3 identity matrix.

With the exception of $\underline{\underline{\mu}}$ and $\underline{g}_j$, all other terms in Eq. (4-34) can be computed once a structure is defined and the equilibrium electrostatic potential is determined. Straightforward procedures can then be followed to determine $\underline{g}_j$ and then $\underline{\underline{\mu}}$. Recently, (in the appendix of reference [54]), a matrix inversion approach was developed that avoids the calculation of $\underline{g}_j$ altogether.

4.2.3 Charge State, the Relaxation Correction, and the IISM Binding Model

The charge state of any peptide depends on the pH of the BGE and the pK_a values of the potentially charged groups. For oligolysines at low pH, the only potentially charged group that is sensitive to the buffer conditions is the C-terminal since the N-terminal and also the side groups of lysine bear a +1 charge. From the apparent pK_a of dilysine (no activity correction) which equals 3.01 in aqueous media at I = 0.10 M at 298.15 K [144], we must set an "intrinsic" pK_a value, pK_a^0, equal to 3.91 using a "charge regulation" procedure described in detail previously [44]. This charge regulation procedure accounts for the influence of neighboring charge groups as well as ionic strength. This value of 3.91 is slightly different from the value of 3.83 used previously [133] due to differences in the way the electrostatics are treated. This value is used throughout the present work for all of the oligolysines and it is also assumed to be independent of temperature. For the monomer, lysine, we simply use the apparent pK_a of 2.16 at I = 0.10 M at 298.15 K [144] and assume the thermodynamic pK_a is independent of ionic strength and temperature. (The apparent pK_a of lysine at I = 0.01 and 0.05 M will be slightly different from 2.16 and are estimated using the extended Debye-Huckel model [54].)

The relaxation effect concerns the distortion of the ion atmosphere around a macroion in response to an external electric or flow field. In most cases, it reduces the model electrophoretic mobility relative to the "unrelaxed" mobility that is obtained when equilibrium ion distributions are assumed. In the present work, we shall use a minor variation of the "large ion" procedure described previously [133]. The "relaxed" mobility, μ_r, is related to the "unrelaxed" mobility, μ_{nr}, that is obtained through modeling, by

$$\mu_r = \mu_{nr}(1-\xi) \qquad (4-42)$$

The correction factor, ξ, will depend on T, properties of BGE, and also the average electrostatic potential averaged over the surface of the macroion, ζ, ("zeta" potential). In the "large ion" approach,

$$\xi = 1000\, y^2(b_1 + b_2 y) \qquad (4-43)$$

Where b_1 and b_2 are constants (depending on the size of the macroion as well as the properties of the BGE) and $y = e\zeta/k_BT$ is a reduced (dimensionless) zeta potential. The coefficients b_1 and b_2 can be written

$$b_j = \sum_{k=0}^{2} d_{jk} R^k \qquad (4-44)$$

The d_{jk} terms depend on T as well as the conditions of the BGE, including pH, but are independent of the physico-chemical properties of the macroion. They can be determined using the O'Brien and White procedure on spheres over a range of charge (zeta potential) and size values appropriate for the peptides of interest [30]. Table 1 summarizes the d_{jk} terms for the buffer conditions of interest in the present work. Since the hydrodynamic radius and "zeta"

potential are readily in the course of the NLPB-BMM determination of mobility of a particular peptide conformation, it is straightforward to use the d_{jk} coefficients given in Table 1, along with y, R, and μ_{nr}, to determine μ_r using Eqs. (4-42 - 4-44) above.

In the next section, it is shown that μ_{exp} and μ_r are not in perfect agreement with each other and that the discrepancy increases with increasing temperature and ionic strength. It is proposed that association that goes beyond classical electrostatic interactions between oligolysines and components of the BGE, $H_2PO_4^-$ in the present case, is responsible for this discrepancy. Previously, a binding model was developed [133] which reduces to the Identical Independent Site Model, IISM [145] and that model shall be used here to interpret the specific binding of phosphate to oligolysine. It is assumed that the principle ions comprising the background electrolyte are monovalent, the macroion is cationic, A^- denotes the principle counterion ($H_2PO_4^-$ in the present case), and X^+ denodes the principle coion (Li^+ in the present case). From Eq. (A25) of reference [133], the average number of bound anions, <m>, per oligolysine molecule of degree of polymerization n is given by

$$< m > \quad = \quad \frac{n\alpha}{(1+\alpha)} \qquad (4-45)$$

$$\alpha \quad = \quad \frac{[A^-]}{K_0(n)} \gamma(X^+)\gamma(A^-)e^{+y(n)} \qquad (4-46)$$

In Eq. (4-46), $[A^-]$ is the bulk concentration of the principle counterion, the γ terms are finite ion Debye-Huckel activity coefficients for counterion and a single cationic binding site, X^+ (see reference [133] for details), y(n) is equated to the reduced zeta potential of an oligomer of degree of polymerization n when a single site of the oligomer has a bound counterion, and $K_0(n)$ is an intrinsic dissociation constant. Physically, $K_0(n)$ represents the dissociation of a single

bound anion from a single cationic site over the n sites of an otherwise discharged oligopeptide in the limit of zero ionic strength [133]. The model mobility of an oligomer of degree of polymerization n with <m> specifically bound anions, $\mu_{mod}(n)$, is related to the model mobility in the absence of any bound anions, $\mu_r(X_n)$, and the mobility of a model with one bound anion, $\mu_r(X_nA)$, by Eq. (4-A28) of reference [10],

$$\mu_{\text{mod}}(n) \quad \cong \quad \mu_r(X_n) + < m > [\mu_r(X_nA) - \mu_r(X_n)] \qquad (4-47)$$

The procedure used in this work to determine $K_0(n)$ is as follows. Experimental measurements yield $\mu_{exp}(n)$ for peptides of different length, temperature, and anion concentration. Modeling allows us to determine the average mobilities, $\mu_r(X_n)$ and $\mu_r(X_nA)$, and Eq. (4-A28) then gives the average number of bound anions, <m>, under the conditions of the experiment. From Eq. (4-45), <m> is related to α, which is defined by Eq. (4-46). Modeling gives us all quantities making up α except, the thermodynamic equilibrium constant, $K_0(n)$. For each n and T we have experimental mobilities for two or three different ionic strength values. This allows us to determine $K_0(n)$ for each n and T values as discussed previously [133].

4.3 Results

In the application of the NLPB-BMM approach to peptides, there are basically no adjustable parameters once the peptide and its assumed secondary structure has been defined along with the solvent, temperature, and conditions of the BGE. In modeling, we shall first ignore the possibility of specific binding of phosphate to the oligolysines. It should be emphasized, however, that electrostatic interactions between the oligolysine and ions of the BGE are included at the continuum (nonlinear PB) level. Shown in Figure 4-2 is the variation of μ with n at 25, 38 and 50 ºC and I = 0.01, 0.05, and 0.10 M. Symbols denote experimental

mobilities (filled squares, filled diamonds, and filled triangles correspond to I = 0.01, 0.05, and 0.10 M, respectively) and lines denote model mobilities (solid, dashed, and dotted correspond to to I = 0.01, 0.05, and 0.10 M, respectively). At 25 ºC, agreement between modeling and experiment is quite good at all ionic strengths. However, at 38 and 50 ºC, absolute model mobilities exceed experimental values. Also, this discrepancy increases with increasing ionic strength or equivalently, the phosphate (counterion) concentration, $[H_2PO_4^-]$. This behavior is indicative of specific binding of phosphate.

For a particular n and T, it is straightforward to use Eqs. (4-44 - 4-47) in an Excel spreadsheet and determine what intrinsic dissociation constant, $K_0(n)$, yields best agreement between modeling and experiment as shown in Figure 4-3. Table 4-2 summarizes all of the pK_0 values for n = 1 to 8 at T = 25, 38, and 50 °C. In addition, average number of bound phosphates, <m>, as well as experimental and model mobilities are displayed for the different n and T values studied.

4.4 Discussions

The following conclusions can be made concerning the binding of phosphate to oligolysines. First of all, binding tends to increase with increasing n, I, and T with little evident binding at 25 ºC. Longer oligos are more highly charged (attract phosphate anions more strongly) and also have more binding sites. Since phosphate concentration varies in direct proportion to I, more binding occurs at higher ionic strength. The temperature dependence is consistent with an endothermic enthalpy change of binding. Also, the intrinsic $pK_0(n)$ values increase with increasing T. For $n \geq 4$ and T > 25 º, the $pK_0(n)$ values show little variation with n at constant temperature. For $n \geq 4$ and T > 25 º, $pK_0(n)$ varies over a range of about 0.1. In terms of

interaction stoichiometry, for oligolysines with n≥5, the average number of phosphate counterion bound per lysine residue is lower than 0.04 at 25°C and about 0.35 at 50°C.

4.5 Concluding Remarks

In this study, we have reported electrophoretic mobilities of highly charged oligolysines at *pH* = 2.5 over a range of temperatures and ionic strengths, and attempted to model them using the NLPB-BMM procedure [42-44, 54,132]. Account is also taken of specific binding of counterions, $H_2PO_4^-$ in this case, to the oligolysines. This study parallels our earlier one [133], but accounts more accurately for equilibrium electrostatics, which is solved at the level of the non linear Poisson Boltzmann equation, NLPB. In a quantitative sense, the results of the present study should be more accurate. Qualitatively, the conclusions remain the same in the two studies. For the same n and T, however, pK_0 values are slightly lower when electrostatics are solved and the NLPB level.

In future work, we will investigate the mobility of oligolysines as a function of pH and also consider the influence of different co and counterions. At low pH in phosphate buffer, the counterion is primarily $H_2PO_4^-$, but divalent phosphate, HPO_4^{-2}, will become increasingly important as the pH is raised.

T(°C)	I(mM)	$d_{1,0}$	$d_{1,1}$	$d_{1,2}$	$d_{2,0}$	$d_{2,1}$	$d_{2,2}$
25	10	-3.465	2.039	0.000	0.365	0.041	-0.013
“	50	-1.502	3.494	0.074	-0.304	0.347	-0.077
“	100	1.333	4.518	0.064	-0.983	0.485	-0.112

38	10	-1.988	1.398	0.050	0.372	0.040	-0.013
“	50	-1.420	3.498	0.072	-0.247	0.314	-0.073
“	100	-1.275	5.292	0.007	-0.301	0.266	-0.094
50	10	-3.418	2.008	0.004	0.360	0.047	-0.013
“	50	-1.466	3.582	0.060	-0.181	0.274	-0.068
“	100	-1.125	5.312	-0.001	-0.250	0.225	-0.088

Table 4-1: “Large Ion” Relaxation Coefficients [(a)]

(a) See Eqs. (4-5) and (4-6).

			I = 0.010 M			I = 0.050 M			I = 0.100 M		
n	*T(°C)*	$pK_0(n)$	$\langle m \rangle$	μ_{mod}	μ_{exp}	$\langle m \rangle$	μ_{mod}	μ_{exp}	$\langle m \rangle$	μ_{mod}	μ_{exp}
1	25	+0.61	.045	2.98	2.89	.151	2.42	2.36	.231	2.09	2.22
“	38	+0.85	.075	3.82	3.76	.235	2.95	2.89	.340	2.46	2.57
“	50	+0.96	.095	4.63	4.52	.283	3.45	3.34	.396	2.84	3.02
2	25	-0.40	.026	3.92	3.89	.085	3.08	3.08	.117	2.83	2.85
“	38	+0.27	.137	5.01	4.73	.335	3.75	3.82	.416	3.23	3.36
“	50	+0.28	.137	6.02	5.92	.343	4.58	4.51	.487	3.93	4.06
3	25	-1.05	.015	4.14	4.21	.039	3.22	3.12	.053	2.87	2.91
“	38	-0.01	.152	5.37	5.08	.364	3.93	4.00	.510	3.38	3.50

“	50	+0.04	.191	6.41	6.29	.346	4.46	4.51	.549	4.14	4.19
4	25	(-10)	0	4.30	4.42	0	3.29	3.24	0	2.87	2.90
“	38	-0.30	.224	5.42	5.35	.438	4.02	4.00	.468	3.46	3.52
“	50	-0.02	.457	6.40	6.51	.807	4.71	4.50	.894	4.04	4.18
5	25	(-10)	0	4.34	4.42	0	3.25	3.21	0	2.86	2.86
“	38	-0.29	.400	5.42	5.34	.764	3.96	3.96	.841	3.44	3.50
“	50	+0.07				1.50	4.57	4.47	1.61	3.98	4.08
6	25	-1.30				.141	3.21	3.19	.145	2.83	2.85
“	38	-0.34				1.16	3.97	3.93	.963	3.45	3.48
“	50	-0.19				1.45	4.66	4.42	2.08	3.81	4.04
7	25	-1.16				.255	3.18	3.17	.255	2.82	2.83
“	38	-0.37				1.24	3.90	3.90	1.21	3.45	3.45
“	50	+0.07				2.74	4.52	4.39	2.60	3.89	4.01
8	25	-1.26				.318	3.16	3.14	.252	2.80	2.81
“	38	-0.44				1.44	3.88	3.87	1.42	3.41	3.43
“	50	-0.09				2.84	4.48	4.36	2.68	3.88	3.98

Table 4-2: Mobility and Model Data for Oligolysines[(1)].

(1) all μ values are in 10^{-4} cm^2 V^{-1} s^{-1}. $K_0(n)$ is the dissociation constant of a single bound anion from a single cationic site averaged over the n sites of an otherwise discharged oligopeptide in the limit of zero ionic strength, <m> is the number of bound anions per oligolysine molecule. μ_{mod} and μ_{exp} are respectively the model and experimental effective mobilities.

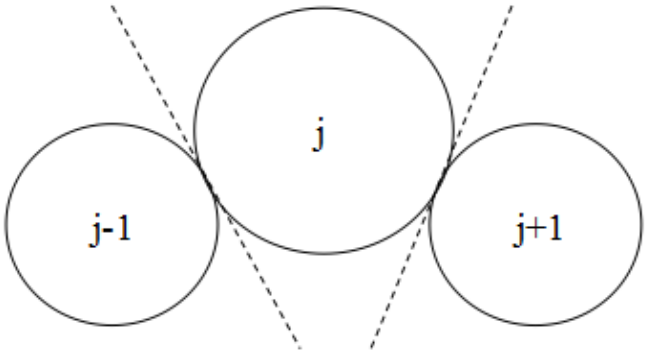

Figure 4-1 Subdivision of space exterior to the bead array.

This is a 2 dimensional rendition and is illustrated with a central, j, and two neighboring, j ± 1, beads. The lines between beads j and j ± 1 denote planes that separate V_{ej} from $V_{e\ j\pm1}$. The external volume, V_{ej}, lies closer to the center of bead j than to any other bead.

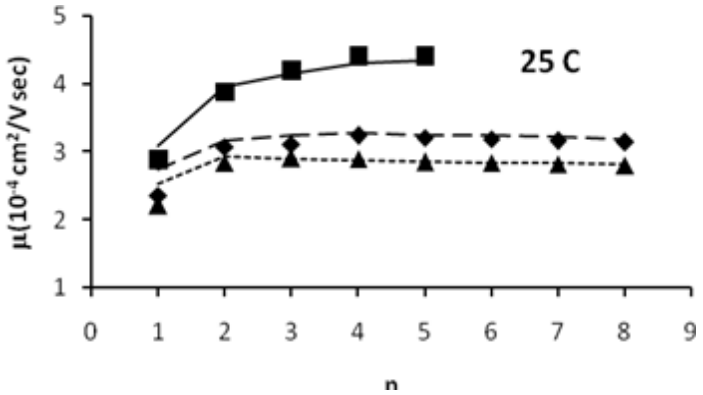

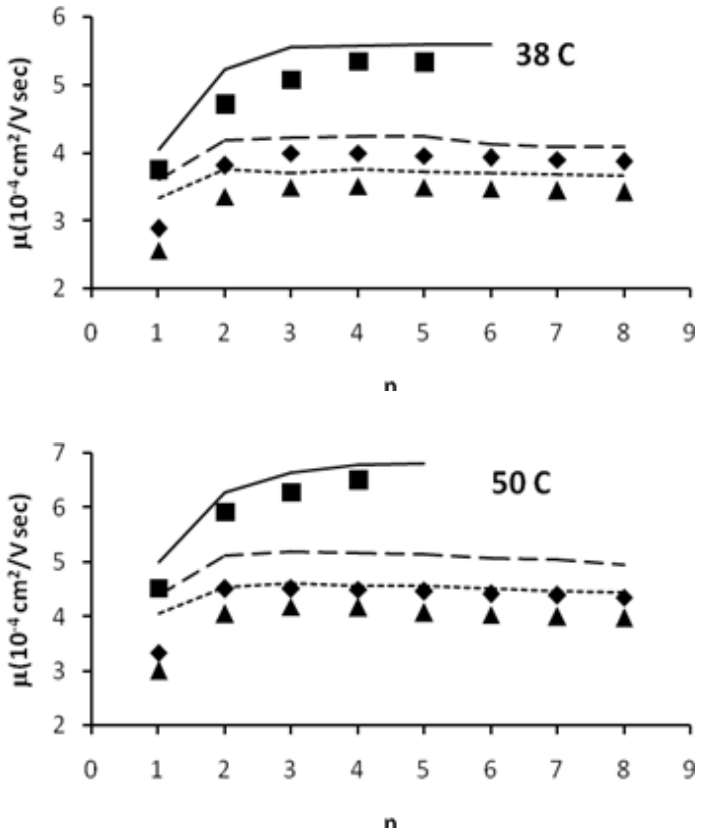

Figure 4-2 Dependence of μ on n for experiment and "nonbinding models" of oligolysines.

The pH equals 2.5 and T = 25, 38, and 50 ◦C. Filled squares, diamonds, and triangles correspond to experimental mobilities at I = 10 mM, 50 mM, and 100 mM, respectively. Solid, dashed, and dotted lines are the corresponding model fits at I = 10 mM, 50 mM, and 100 mM, respectively. Mobilities are in 10^{-4} cm^2 V^{-1} sec^{-1}.

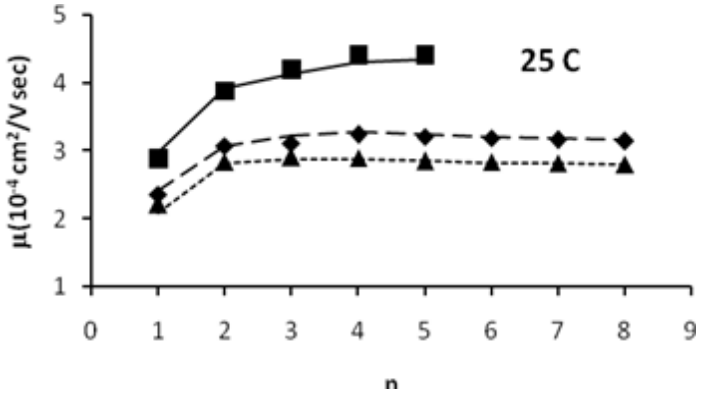

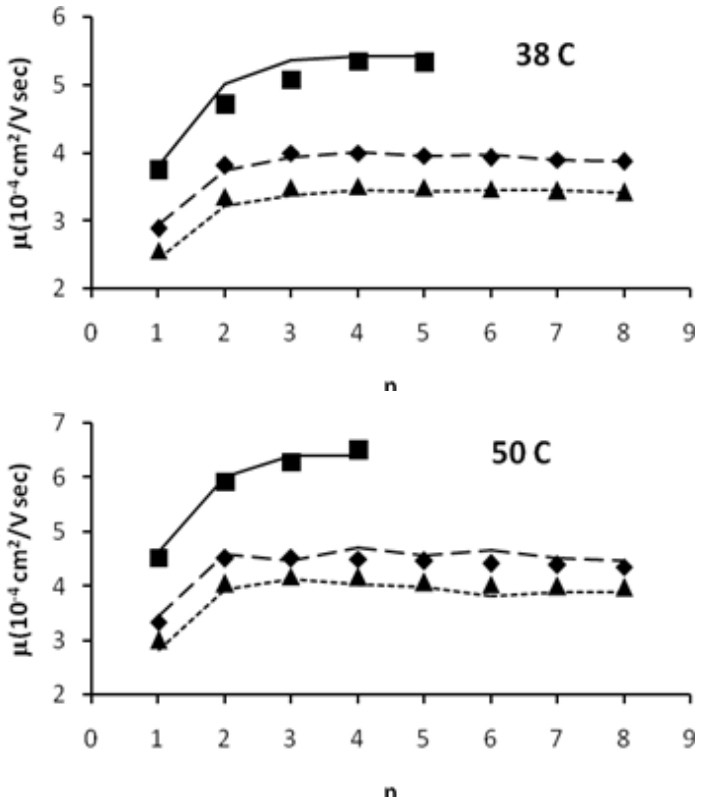

Figure 4-3) Dependence of on n for experiment and IISM binding models of oligolysines.

The pH equals 2.5 and T = 25, 38, and 50 □C. Filled squares, diamonds, and triangles correspond to experimental mobilities at I = 10 mM, 50 mM, and 100 mM, respectively. Solid, dashed, and dotted lines are the corresponding model fits at I = 10 mM, 50 mM, and 100 mM, respectively. Mobilities are in 10^{-4} cm^2 V^{-1} sec^{-1}.

CHAPTER 5

COARSE GRAINED MODELING OF THE TITRATION AND CONDUCTANCE BEHAVIOR OF AQUEOUS FULLERENE HEXA MALONIC ACID (FHMA) SOLUTIONS

5.1 Introduction

Conductance measurements of aqueous solutions containing ionic species are comparatively simple to carry out and are capable of providing valuable information about ions and their interaction with solvent [65]. One of the early successes of continuum modeling of transport concerned the electrical conductance of dilute aqueous solutions of strong electrolytes [3,5,25,146]. Initially limited to very dilute solutions of ions modeled as point charges, the theory was subsequently extended to higher concentrations, and generalized to account, to lowest order, for the finite size of the ions of arbitrary valence [5-8,66,69,70,147]. Recently, progress has been made in extending this theoretical modeling strategy to highly charged nanoparticles [148] and it is an application of this approach that is the focus of the present study.

Since its discovery in 1985 [149], Buckminsterfullerene, $C_{60,}$ has stimulated great interest due to its possible applications in biomedicine [150,151], electronics [152], and optics [153]. The fundamental structure of C_{60} is well characterized [154] and in benzene, it has a hydrodynamic radius of 0.41 nm which comes from measurement of its self diffusion constant by ^{13}C pulsed-field gradient NMR [155]. The poor water solubility of C_{60} can be dealt with by attaching hydrophilic side groups to its surface as is done in the case of fullerene hexa malonic acid, FHMA, $C_{60}(C(COOH)_2)_6$ [156]. An atomic model of FHMA is shown in Figure 1. The development of water soluble fullerene derivatives is essential in their applications to biological systems.

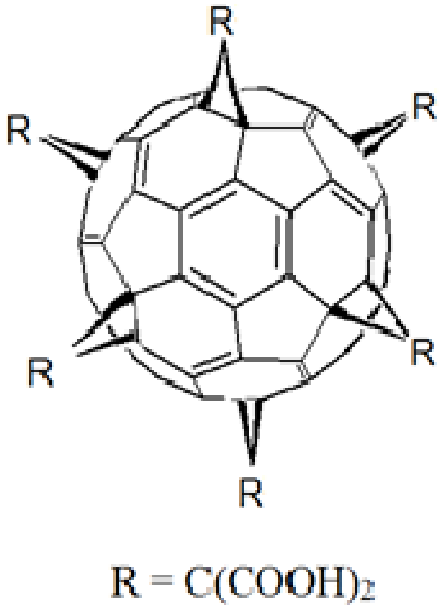

Figure 5-1: Structure of FHMA.

FHMA contains 6 malonic acid substituents ($C(COOH)_2$) covalently attached to the C_{60} fullerene core. Partial deprotonation of FHMA renders it water soluble. The radius of the fullerene core is 0.35 nm [154].

Physico-chemical studies of FHMA have been carried out [156-158] and these are important for a number of reasons. FHMA nanoparticles are comparatively small and have simple, symmetric structures that make them ideal for model studies. At the same time, they are highly charged and can be regarded as prototypical polyelectrolytes. However, this high charge as well the variability in the degree of deprotonation/charge presents challenges from the standpoint of modeling. On a theoretical level, the free solution electrophoretic mobility of charged spherical particles modeled within the framework of the continuum primitive model is well established [26-30]. Once the electrophoretic mobilities of the charged species comprising an aqueous solution are known, it is also straightforward to compute the electrical conductivity

of model solutions [148]. In addition to the mobility of the different possible FHMA species, however, we also need to know their concentrations.

The primary objective of the present work is to carry out a detailed modeling study of the pH titration and conductance behavior of FHMA particles within the framework of the continuum primitive model and compare the model studies with experiment [156-158]. This modeling is coarse grained. The FHMA particle is modeled as a sphere with hydrodynamic radius a with a centrosymmetric charge distribution that arises from deprotonation of malonic acid groups on its surface. These fixed charges are assumed to reside at distance b from the center of the sphere. The surrounding media is modeled as a continuum Newtonian fluid. The ion atmosphere arising from the presence of small ions (H^+, OH^-, and cation A^{+z}) and the various charge states resulting from variable deprotonation of FHMA is treated as a continuum in determining the electrostatic potential around the different charged states of the model FHMA. This involves numerical solution of the non linear Poisson-Boltzmann equation for all possible charge states of the "host" model FHMA particle. The fixed charge is assumed to reside at a fixed distance from the center of the host particle. Also, other (FHMA) particles can contribute to the ionic environment of the host particle, but cannot approach the host within a distance of twice the hydrodynamic radius. Account shall also be taken of specific cation binding to the more highly deprotonated particle forms. Electrophoretic mobilities of the different charge states of FHMA are numerically computed using the O'Brien-White procedure [29]. As discussed in Appendix A, the electrophoretic mobilities of H^+, OH^-, and A^{+z} are computed using a "small ion" model. The total solution conductance is related in a simple way to the concentrations and mobilities of all ions present. This methodology is applied the titration and conductance behavior of FHMA aqueous solutions counterion Na^+ and to a more limited extent

Ca^{+2}. In the present work, it is necessary to include specific counterion binding of both Na^{+} and Ca^{+2} in order to obtain good agreement between modeling and experiment [156-158]. We would like to emphasized, however, that specific counterion binding is only one possible explanation for the observed conductance behavior. We shall return to this point at the end of this work. Since modeling also requires knowledge of the concentrations of deprotonated FHMA species as well as specifically bound counterion-FHMA complexes, we also examine these distributions.

5.2 Methods

The particle is modeled as a sphere with hydrodynamic radius a containing a centro-symmetric fixed charge distribution located at distance b ($b \geq a$) from the distance of the sphere. This charge arises from the deprotonation of an even number, n, of titratable proton sites. It is assumed that there are two distinct classes of sites with intrinsic acid dissociation constants, K_1 and K_2. In the case of FHMA, these sites correspond to 6 malonic acid groups, $C(COOH)_2$, covalently attached to the fullerence core. We start with c_x moles/liter of FHMA particles in a water solvent at temperature T at initial pH equal to pH_0. The initial solution will be fairly acidic resulting from (partial) deprotonation of FHMA. This solution is titrated with concentrated base, $A(OH)_z$ where A is the cation (valence charge z). As base is added to the solution, OH^- from the base combines with H^+ and the pH rises. Define α_n as the moles of added $A(OH)_z/(zc)$ so that the beginning of the titration correspond to $\alpha_n = 0$ and $\alpha_n = 1$ corresponds to adding just enough base to neutralize all of the titration sites of FHMA. In order to account for the conductance, κ, observed experimentally, it is necessary to include specific binding A^{+z} to (partially) deprotonated states FHMA. We introduce an intrinsic binding constant, K_B, to account for this and binding of A shall only be considered to occur to doubly deprotonated groups (over half of the titratable sites of FHMA are deprotonated). In order to calculate the titration profile, α_n

versus pH, of FHMA, we need to determine the concentration of the various deprotonated species, $[XH_{n-j}]$ (j ranges from 0 to n), as well as the concentration of the various cation bound complexes, $[XH_{n-j}A_k]$ with as few input parameters as possible. The details of the modeling procedure both with regard to the calculation of the concentration of the various FHMA species as well as the conductance are placed in Appendix A. Since this important, but of interest to a limited audience. To summarize, input parameters to determine the titration curve include pK_1, pK_2, pK_B, a, b, T, c_x, and the relative permittivity of the solvent, ε_r. As discussed at some length in Appendix A, account is taken of multiple configurations as well as how the charge state and ionic screening influence deprotonation/binding. One requirement is knowledge of the electrostatic potential in the vicinity of the model FHMA for all possible charge states and this requires an iterative numerical procedure to solve the non linear Poisson Boltzmann equation [148]. In order to calculate the conductivity, κ, "small ion" theory is [3, 5 8, 25, 63, 65, 66, 69, 70, 146, 147] is used to compute the contribution of H^+, OH^-, and A^{+z}; and the O'Brien White procedure [30] is used to calculate the contribution of the various FHMA states as discussed in Appendix A.

The hydrodynamic radius of C_{60} in benzene has been measured to be 0.41 nm [155], but the presence of six malonic acid groups, $(C(COOH)_2)$, attached to the core sphere is expected to result in a substantially larger hydrodynamic radius for FHMA. As far as we are aware, however, there have been no direct measurements of a from diffusion measurements by NMR [155] or boundary spreading techniques [159]. A value of 0.77 nm has been used for FHMA, but this is based on an analysis of density data, not transport [156]. We shall estimate a for FHMA using the "volume increment" method of Edward [160]. Assuming a core radius of 0.4 nm, we then add the appropriate volume increments tabulated in reference 31 for six malonic acid

groups. A simple calculation yields a volume corresponding to a sphere of 0.6 nm in radius. In "Model A", we shall set a = b (the distance of fixed charges from the center of the sphere) equal to 0.6 nm. To illustrate the sensitivity of the results on a (and b), we shall also consider two other models which correspond to smaller (Model B: a = 0.45 nm, b = 0.60 nm), and larger (Model C: a = b = 0.77 nm) model FHMA particles than Model A. We shall ignore the variation of a with state of deprotonation or binding of A^{+z} ions. The particle size, on the basis of a, increases in the order Model B, Model A, Model C.

5.3 Results

5.3.1 pK1 and pK$_2$ for Models A, B, C (no counterion binding)

The most straightforward way of determining pK_1 and pK_2 for our FHMA models is to adjust them until a good match is obtained between experimental titration (pH versus α_n) and conductance (κ versus α_n) behavior and modeling. For the moment, we shall not consider counterion binding and will set $pK_B = +5$ which insures this condition. We shall analyze the titration data of FHMA with NaOH at 25 °C reported by Cerar et al. [156]. The concentration of FHMA, c_x, is 1.15 x 10^{-4} M. At the beginning of the titration ($\alpha_n = 0.0$), the pH is expected to depend primarily on the dissociation of most acidic protons of FHMA, or pK_1. In addition, the conductance at the beginning of the titration is expected to be very sensitive to pK_1 as well. The way the program is structured, the pH is read in as an input parameter (along with pK_1, pK_2, pK_B, and a number of other parameters) and α_n is calculated (Eq. (20) of Appendix A).

The pH corresponding to $\alpha_n = 0$, pH_0, can be determined by testing a range of initial pH values, determining their corresponding α_n values, and then interpolating what pH value yields $\alpha_n = 0$. It turns out that the initial pH is fairly insensitive to pK_1, but the conductivity, κ, is quite

sensitive to pK_1. Consequently, the κ value corresponding to $\alpha_n = 0$ is also useful in matching experimental and model data for $\alpha_n = 0$. From experiment pH_0 is about 3.25 and κ equals 222 (in 10^{-4} ohm^{-1} m^{-1}). The appropriate pK_2 value can be determined by matching the experimental and model titration curves in the range $0.5 < \alpha_n < 1.0$. Good model fits to experimental titration curves for Models A, B, and C assuming no binding of Na^+ can be found by suitable adjustment of pK_1 and pK_2. However, if we compare the corresponding model conductivity, κ (in 10^{-4} 1/(ohm m)), versus α_n behavior with experiment, substantial differences are apparent as shown in Figure 2. For α_n less than about 0.2, model and experimental κ values are in excellent agreement, but at higher α_n, model conductivities exceed experiment. However, better agreement with experiment is achieved by choosing larger a values (Models A and C). We interpret the discrepancy between model and experiment at large α_n to be indicative of specific binding of Na^+ to fullerene that goes above and beyond simple electrostatic interactions between the deprotonated carboxylic acid sites of FHMA and the principle counterion, Na^+. In the next subsection, we shall address this question for Models A and C. We shall not pursue Model B any further since a is too small on structural grounds to be realistic. It has been included here simply to illustrate how it is possible to fit the titration curve for a broad range of particle sizes by appropriate adjustment of just two parameters, pK_1 and pK_2.

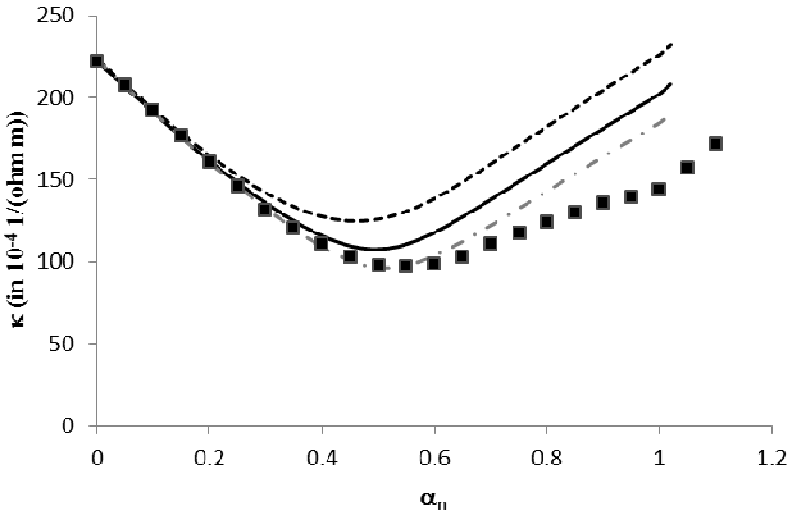

Figure 5.2 Conductivity, κ (in 10^{-4} 1/(ohm m)), versus α_n of FHMA and Models A, B, and C with no counterion binding at 25 °C, $c_x = 1.15 \times 10^{-4}$ M.
Squares represent experimental values and darked dashed, solid, and light dashed lines correspond to Models A, B, and C, respectively. See the text for details regarding the values of pK_1 and pK_2 appropriate for each model ($pK_B = +5.0$).

5.3.2 Inclusion of Na^+ specific binding for Models A and C

Call the procedure outlined in Section 3.1 to obtain pK_1 and an initial estimate pK_2 "Step 1". To account for the possibility of counterion binding, set pK_1 and pK_2 to the values obtained in Step 1 and consider a range of pK_B values and attempt to match model and experimental κ and this is called "Step 2". A complicating feature of the model is that counterion binding, holding pK_2 constant, induces the release of protons at large α_n. In other words, the titration curve is influenced by pK_B as well as pK_1 and pK_2. Once a pK_B value is found that matches the experimental κ versus α_n curve, it is necessary to make further adjustments in pK_2 (call this "Step 3") to match model and experimental titration curves. It may be possible to iterate Steps 2 and 3 to obtain ultimate convergence. The results of this procedure applied to Model A are shown in Figures 5.3 and 5.4. In these figures, the optimal parameters for pK_1, pK_2, and pK_B

are: 1.8, 4.2, and -1.4, respectively. A similar analysis applied to Model C leads to optimal parameters for pK_1, pK_2, and pK_B yields 1.9, 4.5, and -1.5.

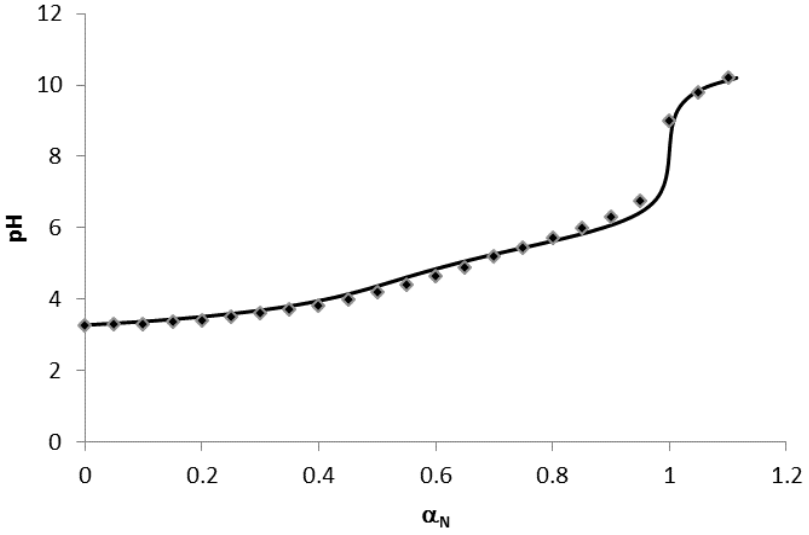

Figure 5.3 Titration curve (pH versus α_n) of FHMA and Model A with pK_1 = 1.8, pK_2 = 4.2, and pK_B = -1.4 at 25 °C $c_x = 1.15 \times 10^{-4}$ M. Squares represent experimental values and the solid line the corresponding model values.

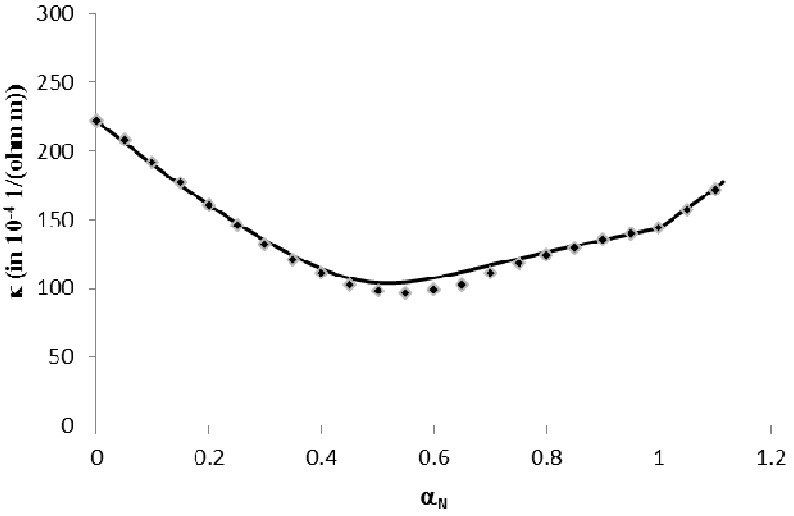

Figure 5.4 Conductivity, κ (in 10^{-4} 1/(ohm m)), versus α_n of FHMA and Model A with pK_1 = 1.8, pK_2 = 4.2, and pK_B = -1.4 at 25 °C, $c_x = 1.15 \times 10^{-4}$ M. Squares represent experimental values and the solid line the corresponding model values.

5.3.3 Conductance of FHMA in the presence of Ca^{+2} at 25 °C

The principle counterion in the previous two subjections is Na^+ and it is also worthwhile to consider how well the procedure works for divalent ions which provide a more severe test of the continuum primitive model. There is limited conductance data of FHMA in the presence of Ca^{+2} principle counterion from the work of Vrhovsek et al. [158] and we shall analyze some of their results here using Model A. The values of pK_1 and pK_2 should be unchanged from before (1.8 and 4.2, respectively), but pK_B is expected to be different. In the experiment, FHMA samples of variable concentration are titrated with $Ca(OH)_2$ until the pH reaches 6.0 and the molar conductance ($\Lambda = \kappa/c = \kappa/(12c_x)$) is plotted versus $c^{1/2}$. The experimental curve (diamonds) and Model A results (lines) for variable pK_B are plotted in Figure 5 at T = 25 °C. Good fit to experimental data is achieved for pK_B = -2. As in the case of Na^+, it is necessary to include some degree of counterion binding in order to reconcile experimental and model conductances. Similar fits are also achieved at 5, 15, and 35 °C.

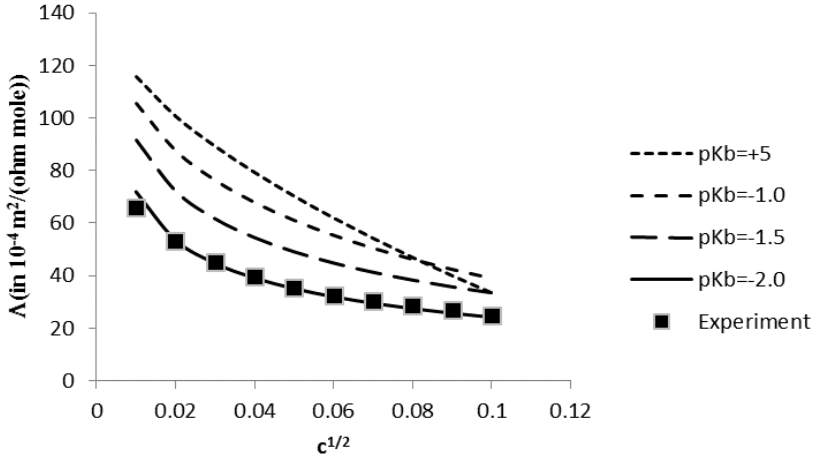

Figure 5.5 Equivalent Conductance, Λ (in 10^{-4} m^2/(ohm mole)) of FHMA versus c for Model A and experiment at pH = 6 and 25 °C where the counterion is Ca^{+2}. Experimental data comes from Vrhovsek et al. (158). Lines are the result of modeling with pK_1 = 1.8, pK_2 = 4.2, and variable pKB.

5.3.4 Distributions of FHMA Species with pH

Although the conductance and titration behavior measured experimentally does not provide direct evidence of the charge state of the FHMA particles and details about specific counterion binding, the model developed in this work allows us to investigate this issue and we shall illustrate this with Model A in the presence of Na^+ (principal counterion) at 25 °C with pK_1 = 1.8, pK_2 = 4.2, pK_B = -1.4. These parameters were deduced in subsection 3.2. In the absence of counterion binding (pK_B = +5), the distribution of valence charge of FHMA versus pH exhibits the behavior expected of a polyprotic acid. However, specific binding alters this distribution. Shown in Figure 6 are the fractional distributions of FHMA model particles with valence charges of -6 through -10. Other species may also be present, but in lower concentration. At high pH, the dominant species carries a valence charge of -9 with lesser quantities of -7, -8, and -10 species. It should be emphasized, however, that the model predicts a range of different charge species present at a particular pH and this distribution changes with pH. Also shown on Fig. 6 is the average number of bound Na^+ divided by 3.243 (the average number bound at pH = 9.85). Below a pH of 4, very little Na^+ is bound. However, the fraction of bound sodium rises sigmoidally with pH and reaches a plateau value at a pH of about 7.

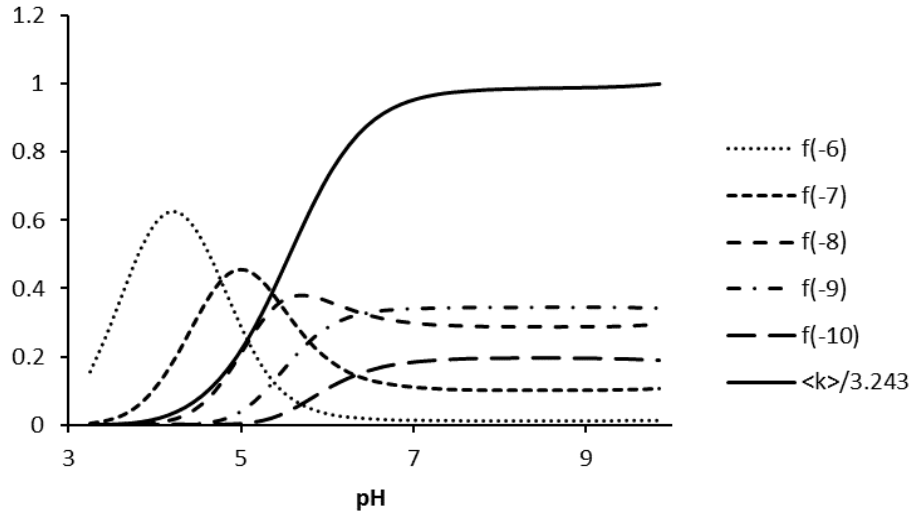

Figure 5.6 Ion Charge Distributions and Extent of Counterion Binding in Model FHMA. The model is Model A described in the text with pK_1, pK_2, and pK_B equal to 1.8, 4.2, and -1.4, respectively at 25 °C, $c_x = 1.15 \times 10^{-4}$ M. The various dotted curves give the fraction of FHMA particles in the designated net charge states of -6 through -10 as a function of pH. Other charge states are present, but in only small amount. The solid line represents the average number of bound Na^+ ions divided by 3.243. The average number of bound Na^+ ions is 3.243 at pH = 9.85.

The distributions shown in Figure 6 do not provide information about the number of bound Na^+ in the different valence charge states. For example, a valence charge of -9 could be due to XH_3^{-9}, XH_2Na^{-9}, $XHNa_2^{-9}$, and/or XNa_3^{-9}. Define X(z,k) as the fraction of FHMA model species with a valence charge of z that have k specifically bound Na^+ ions. For example X(-9,1) is the fraction of the -9 species (due to XH_3^{-9}, XH_2Na^{-9}, $XHNa_2^{-9}$, and XNa_3^{-9}) present as XH_2Na^{-9}. Up to a pH of about 5, all -9 charged species are present as XH_3^{-9} and above a pH of about 7, as XNa_3^{-9}. In the mid pH range of 5 to 7, substantial fractions of XH_2Na^{-9} and $XHNa_2^{-9}$ are also present.

5.4 Discussion

The overall objective of the present work is to determine how well the coarse grained continuum primitive model can account for the titration and conductance behavior of a small,

well characterized, prototypical polyelectrolyte. The system we chose to analyze is a derivative of fullerene containing six malonic acid residues covalently attached to the C_{60} core, FHMA. As discussed in Section 2 and Appendix A, the principal input parameters are the intrinsic pK's of the two carboxylic acid groups of malonic acid, pK_1 and pK_2, the net number of charge sites present, n, the specific binding constant of a principle counterion, pK_B, the hydrodynamic radius of the particle, a, the distance of the fixed charges of the particle from its center, b, temperature, T, solvent viscosity, η, dielectric properties of the particle and fluid, and properties of the principal counterion, A^{+z}. Electrostatics are solved numerically at the level of the non-linear Poisson-Boltzmann equation and account is also taken of the influence electrostatics has on the various dissociation states of the particle. From these input parameters, the concentrations of various charge states and binding states (of A^{+z}), are determined and this allows us to construct the titration curve (α_n versus pH) of the model particle and compare it with experiment. In order to predict the electrical conductance [148], it is necessary to determine the electrophoretic mobilities of the various charge states of the model FHMA particle and this is done using the O'Brien and White procedure [30]. The contribution to the conductance of the small ions is estimated using a procedure based on the Onsager-Fuoss procedure [3,148].

5.5 Concluding Remarks

For reasonable choices of input parameters, we have been able to obtain good agreement between modeling and experiment for both titration and conductance data. However, it is necessary to include specific binding of the principal counterion in order to achieve this and this necessity is quite striking. This is true not only for Na^+, but for Ca^{+2} as well. It should be emphasized that other explanations are possible. Cerar and Skerjanc [161] interpreted the conductance/titration data of FHMA in alkali and calcium salts in terms of a widely used two

state model developed many years ago by Wall and coworkers [162]. On the basis of this model, it was determined that the fraction of "free" and "bound" counterions in the presence of FHMA is roughly the same for Li^+, Na^+, and Cs^+ and concluded that counterion association with FHMA is largely electrostatic in nature. In the modeling carried out in the present work, electrostatic association at the level of the (nonlinear) Poisson-Boltzmann equation is not regarded as "binding" so the terms have different meanings in different modeling strategies. Nonetheless, the work of Cerar and Skerjanc [161] indicates that our modeling would reveal comparable "specific binding" of all alkali ions and that indeed is the case. In light of this, we are currently exploring alternative explanations to specific binding. One possibility is that the mobility of counterions that are in close proximity to FHMA are lower than bulk values due to hydrodynamic interaction, HI [97] and the results of that study will hopefully be reported in future work. We believe that the results presented here will stimulate new interest in applying coarse grained modeling strategies to more complicated systems in chemical engineering, chemistry, nano-science, and molecular biology. In addition to modeling experimental observables such as titration behavior and electrical conductance, it is possible to also use modeling to investigate other issues such as the distribution of charge and binding states of the model particles.

REFERENCES

[1] P. Debye, E. Huckel, Phys. Z. 24 (1923) 305.

[2] L. Onsager, Phys. Z. 28 (1927) 277.

[3] L. Onsager, R.M. Fuoss, J. Phys. Chem. 36 (1932) 2689.

[4] P. Debye, E. Huckel, Phys. Z. 24 (1923) 185.

[5] E. Pitts, Proc. R. Soc. London, Ser. A 217 (1953) 43.

[6] R.M. Fuoss, L. Onsager, Proc. Natl. Acad. Sci. USA 41 (1955) 273. 1010.

[7] R.M. Fuoss, L. Onsager, J. Phys. Chem. 61 (1957) 668.

[8] J. Quint, A. Viallard, J. Solution Chem. 7 (1978) 137. 525, 533.

[9] Adamson, N. J., Reynolds, E. C., J. Chromatogr. B 1997, 699, 133–147.

[10] Messana, I., Rossetti, D. V., Cassiano, L., Misiti, F.,Giardina, B., Castagnola, M., J.Chromatogr. B 1997, 699, 149–171.

[11] Cifuentes, A., Poppe, H., Electrophoresis 1997, 18, 2362–2376.

[12] Kasicka, V., Electrophoresis 2006, 27, 142–175.

[13] Kasicka, V., Electrophoresis 2008, 29, 179–206.

[14] Foret, F., Electrophoresis 2009, 30, 534–539.

[15] Kasicka, V., Electrophoresis 2010, 31, 1–25

[16] Grossman, P. D., Colburn, H. H., Lauer, H. H., Anal. Biochem. 1989, 179, 28–33.

[17] Rickard, E. C., Strohl, M. M., Nielsen, R. G., Anal. Biochem. 1991, 197, 197–207.

[18] Cifuentes, A., Poppe, H., J. Chromatogr. A 1994, 680, 321–341.

[19] Castagnola, M., Cassiano, L., Messana, I., Nocca, G., Rabino, R., Rossetti, D. V., Giardina, B., J. Chromatogr. B 1994, 656, 87–97.

[20] Survay, M. A., Goodall, D. M., Wren, S. A. C., Rowe, R. C., J. Chromatogr. A 1996, 741,

99–113.

[21] Janini, G. M., Metral, C. J., Issaq, H. J., Muschik, G. M., J. Chromatogr. A 1999,848, 417–433.

[22] Offord, R. E., Nature (Lond.) 1966, 211, 591–593.

[23] Sitaram, B.R., Keah, H.H., and Hearn, T.W., J. Chromatogr. A, 1999, 857, 263.

[24] Debye, P., Huckel, E., Physik. Zeitschr. 1924, 25, 49–52.

[25] Huckel, E., Physik. Zeitschr. 1924, 25, 204–210

[26] Henry, D. C., Proc. R. Soc. Lond. 1931, 133A, 106–140.

[27] Overbeek, J. Th. G., Kolloid Beih. 1943, 54, 287–364.

[28] Booth, F., Proc. R. Soc. Lond. 1950, 203A, 514–551.

[29] Wiersema, P. H., Loeb, A. L., Overbeek, J. Th. G., J. Colloid Interface Sci. 1966, 22,78–99.

[30] O'Brien, R. W., White, L. R., J. Chem Soc. Faraday Trans. 2 1978, 74, 1607–1626.

[31] G.M. Janini, C.J. Metral, H.J. Issaq, J. Chromatogr. A 924 (2001) 291.

[32] M. Jalali-Heravi, Y. Shen, M. Hassanisadi, M.G. Khaledi, J. Chromatogr. A 1096 (2005) 58

[33] Stigter, D., J. Phys. Chem. 1978, 82, 1417–1423, 1424–1429.

[34] Allison, S. A., Chen, C., Stigter, D., Biophys. J. 2001, 81, 2558–2568.

[35] Yoon, B. J., Kim, S., J. Colloid Interface Sci. 1989, 128, 275–288.

[36] Allison, S. A., J. Coll. Interface Sci. 2005, 282, 231–237.

[37] Kim, J. Y., Ahn, S. H., Kang, S. T., Yoon, B. J., J. Colloid Interface Sci. 2006, 299, 486–492.

[38] Allison, S. A., Macromolecules 1996, 29, 7391–7401.

[39] Mazur, S., Chen, C., Allison, S. A., J. Phys. Chem. B 2001, 105, 1100–1108.

[40] Allison, S. A., Carbeck, J. D., Chen, C., Burkes, F., J. Phys. Chem. B 2004, 108, 4516–

4524.

[41] Allison, S. A., Xin, Y., Mitchell, H., in: Pandali, S. G. (Ed.), Recent Developments in Macromolecules, Vol. 8, Research Signpost, Kerali, India 2005, pp. 25–46.

[42] Xin, Y., Mitchell, H., Cameron, H., Allison, S. A., J. Phys. Chem. B 2006, 110, 1038–1045.

[43] Xin, Y., Hess, R., Ho, N., Allison, S. A., J. Phys. Chem. B 2006, 110, 25033–25044.

[44] Pei, H., Xin, Y., Allison, S. A., J. Sep. Sci. 2008, 31, 555–564.

[45] Pei, H., Allison, S. A., J. Chromatogr. A 2009, 1216, 1908–1916.

[46] Hunter, R. J. Introduction to Modern Colloid Science; Oxford University Press: Oxford, UK, 2002; Chapter 7.

[47] Allison, S. A.; Carbeck, J. D.; Chen, C.; Burkes, F. J. Phys. Chem. B 2004, 108,4516.

[48] P.H. Wiersema, Ph.D. Thesis, Utrecht University, The Netherlands, 1964.

[49] W.H. Lee, R.J. Wheaton, J. Chem. Soc., Faraday Trans. 2 (74) (1978) 743. 1456.

[50] W.H. Lee, R.J. Wheaton, J. Chem. Soc., Faraday Trans. 2 (75) (1979) 1128.

[51] V. Solinova, V. Kasicka, D. Koval, J. Hlavacek, Electrophoresis 25 (2004) 2299.

[52] R. Plasson, H. Cottet, Anal. Chem. 77 (2005) 6047.

[53] S.A. Allison, H. Pei, U.T. Twahir, H. Wu, H. Cottet, J. Sep. Sci. 33 (2010) 2430.

[54] D. Li, S. Fu, C.A. Lucy, Anal. Chem. 71 (1999) 687.

[55] D. Koval, V. Kasicka, I. Zuskova, Electrophoresis 26 (2005) 3221.

[56] J.D. Carbeck, I.J. Colton, J.R. Anderson, J.M. Deutch, G.M. Whitesides, J. Am.Chem. Soc. 121 (1999) 10671.

[57] J.D. Carbeck, R.S. Negin, J. Am. Chem Soc. 123 (2001) 1252.

[58] M. Pamera, J. Wang, E. Grushka, R. Polsky, Anal. Chem. 73 (2001) 5625.

[59] W.-M. Hwang, C.-Y. Lee, D.W. Boo, J.-G. Choi, Bull. Korean Chem. Soc. 24 (2003) 684.

[60] M. Jaros, K. Vcelakova, I. Zuskova, B. Gas, Electrophoresis 23 (2002) 2667.

[61] M. Stedry, M. Jaros, V. Hruska, B. Gas, Electrophoresis 25 (2004) 3071.

[62] S.A. Allison, J. Colloid Interface Sci. 332 (2009) 1.

[63] R.M. Fuoss, K.-L. Hsia, Proc. Natl. Acad. Sci. USA 57 (1967) 1550.

[64] R.M. Fuoss, J. Phys. Chem. 79 (1975) 525.

[65] R.M. Fuoss, J. Phys. Chem. 82 (1978) 2427.

[66] H. Bianchi, R. Fernandez-Prini, J. Solution Chem. 22 (1993) 557.

[67] R.M. Fuoss, J. Phys. Chem. 63 (1959) 633.

[68] J.M.G. Barthel, H. Krienke, W. Kunz, Physical Chemistry of Electrolyte Solutions– Modern Aspects, Steinkopff, Springer, Darmstadt, New York, 1998.

[69] M. Tomsic, M. Bester-Rogac, A. Jamnik, R. Neueder, J. Barthel, J. Solution Chem.31 (2002) 19.

[70] M. Bester Rogac, V. Babic, T.M. Perger, R. Neueder, J. Barthel, J. Mol. Liq. 118 (2005) 111.

[71] C.-M. Hu, R. Zwanzig, J. Chem. Phys. 60 (1974) 4354.

[72] S.A. Allison, Macromolecules 32 (1999) 5304.

[73] J. Happel, H. Brenner, Low Reynolds Number Hydrodynamics, Martinus Nijhoff, The Hague, 1983.

[74] S. Kim, S.J. Karilla, Microhydrodynamics, Butterworth-Heinemann, Boston, 1991.

[75] S.A. Allison, Y. Xin, H. Pei, J. Colloid Interface Sci. 313 (2007) 328.

[76] C.R. Cantor, P.R. Schimmel, Biophysical Chemistry, Part II, W.H. Freeman & Co.,San Francisco, CA, 1980.

[77] M. von Smoluchowski, Phys. Z. 17 (1916) 557, 585.

[78] S. Chandrasekhar, Rev. Mod. Phys. 15 (1943) 1.

[79] D.F. Calef, J.M. Deutch, Annu. Rev. Phys. Chem. 34 (1983) 493.

[80] D.R. Lide (Ed.), CRC Handbook of Chemistry and Physics, 74th ed., CRC Press,Boca Raton, FL, 1993.

[81] G.C. Benson, A.R. Gordon, J. Chem. Phys. 113 (1945) 473.

[82] A.L. Loeb, J.Th.G. Overbeek, P.H. Wiersema, The Electric Double Layer Around a Spherical Colloid Particle, MIT Press, Cambridge, MA, 1961.

[83] Zimmerman, S.B.; Minton, A. *Annu. Rev. Biophys. Biomol. Struct*. 1993, *22*, 27-65.

[84] Dwyer, J.D.; Bloomfield, V.A. *Biophys. J*. 1993, *65*, 1810-1816.

[85] Johnson, E.M.; Berk, D.A.; Jain, R.K.; Deen, W.M. *Biophys. J*. 1996, *70*, 1017-1026.

[86] Pluen, A.; Netti, P.A.; Jain, R.K.; Deen, W.M. *Biophys. J. 1999*, *77*, 542-552.

[87] Pernodet, N.; Tinland, B.; Sturm, J.; Weil, G. *Biopolymers* 1999, *50*, 45-59.

[88] Sass, H.J.; Musco, G.; Stahl, S.J.; Wingfield, P.T.; Grzesiek, S *J. Biomol. NMR* 2000, *18*, 303-309.

[89] Fatin-Rouge, N.; Starchev, K.; Buffle, J. *Biophys. J*. 2004, *86*, 2710-2719.

[90] Tatarkova, S.A.; Berk, D.A *Phys. Rev. E* 2005, *71*, 41913-1-41913-5.

[91] Hirota, N.; Kumaki, Y.; Narita, T.; Gong, J.P.; Osada, Y *J. Phys. Chem. B* 2000, *104*, 9898-9903.

[92] Fatin-Rouge, N.; Milon, A.; Buffle, J *J. Phys. Chem. B* 2003, *107*, 12126-12137.

[93] Wijmenga, S.S.; Maxwell, A. *Biopolymers* 1986, *25*, 2173-2186.

[94] Stellwagen, N.C *Colloids Surf. A* 2002, *209*, 107-122.

[95] Hungerford, G.; Rei, A.; Ferreira, M.I.C.; Suhling, K.; Tregido, K. *J. Phys. Chem. B* 2007, *111*, 3558-3562.

[96] Shen, H.; Hu, Y.; Saltzman, W.M. *Biophys. J*. 2006, *91*, 639-644.

[97] Allison, S.A.; Pei, H.; Haynes, B.M.H.; Xin, Y.; Law, L.; Labrun, J.; Augustin, D. *J. Phys. Chem. B* 2008, *112*, 5858-5866.

[98] Pei, H.; Allison, S.A.; Haynes, B.M.H.; Augustin, D *J. Phys. Chem. B* 2009, *113*, 2564-2571.

[99] Brinkman, H.C. *Appl. Sci. Res. A* 1947, *1*, 27-34.

[100] Debye, P.; Bueche, A.M. *J. Chem. Phys*. 1948, *16*, 573-579.

[101] Felderhof, B.U.; Deutch, J.M. *J. Chem. Phys*. 1975, *62*, 2391-2397.

[102] Felderhof, B.U. *Physica* 1975, *80A*, 63-75.

[103] Allison, S.A.; Pei, Y.; Xin, Y. *Biopolymers* 2007, *87*, 102-114.

[104] Stigter, D. *Macromolecules* 2000, *33*, 8878-8889.

[105] Ferree, S.; Blanch, H.W. *Biophys. J*. 2004, *87*, 468-475.

[106] Jackson, G.W.; James, D.G. *Can. J. Chem*. 1986, *64*, 362-374.

[107] Laurent, T.C. *Biochim. Biophys. Acta* 1967, *136*, 199-205.

[108] Johnson, E.M.; Berk, D.A.; Jain, R.K. *Biophys. J*. 1995, *68*, 1561-1568.

[109] Allison, S.A. *Biophys. Chem*. 2001, *93*, 197-213.

[110] Garcia de la Torre, J.; Rodes, *J. Chem. Phys*. 1983, *79*, 2454-2460.

[111] Garcia de la Torre, J.; Bloomfield, V.A. *Quart. Rev. Biophys*. 1981, *14*, 81-139.

[112] Garcia de la Torre, J.; Huertas, M.L.; Carrasco, B. *Biophys. J*. 2000, *78*, 719-730.

[113] Aragon, S.R. *J. Comput. Chem*. 2004, *25*, 1191-1205.

[114] Garcia Bernal, J.M.; Garcia de la Torre, J. *Biopolymers* 1980, *19*, 751-766.

[115] Garcia de la Torre, J.; Jimeniz, A.; Freire, J.J. *Macromolecules* 1982, *15*, 148-154.

[116] Elias, J.G.; Eden, D. *Macromolecules* 1981, *14*, 410-419.

[117] Hagerman, P.J *Biopolymers* 1981, *20*, 1503-1535.

[118] Diekmann, S.; Hillen, W.; Morgeneyer, B.; Wells, R.D.; Porschke, D. *Biophys. Chem.* 1982, *15*, 263-270.

[119] Tirado, M.M.; Martinez, C.M.; Garcia de la Torre, J. *J. Chem. Phys*. 1984, *81*, 2047-2052.

[120] Eimer, W.; Williamson, J.R.; Boxer, S.G.; Pecora, R. *Biochemistry* 1990, *29*, 799-811.

[121] Hagerman, P.J.; Zimm, B.H. *Biopolymers* 1981, *20*, 1481-1502.

[122] Schellman, J.A.; Harvey, S.C. *Biophys. Chem.* 1995, *55*, 95-114.

[123] Geggier, S.; Kotlyar, A.; Vologodskii, A. *Nucl. Acids Res*. 2010, *39*, 1419-1426.

[124] Allison, S.A.; Schurr, J.M. *Macromolecules* 1997, *30*, 7131-7142.

[125] Lewis, R.J.; Allison, S.A.; Eden, D.; Pecora, R. *J. Chem. Phys*. 1988, *89*, 2490-2503.

[126] Djabourov, M.; Clark, A.H.; Rowlands, D.W.; Murphy, S.B. *Macromolecules* 1989, *22*, 180-188.

[127] Allison, S.A.; Li, Z.; Reed, D.; Stellwagen, N.C. *Electrophoresis* 2002, *23*, 2678-2689.

[128] Calladine, C.R.; Collis, C.M.; Drew, H.R.; Mott, M.R. *J. Mol. Biol*. 1991, *221*, 981-1005.

[129] Zimm, B.H.; Levene, S.D. *Quart. Rev. Biophys*. 1992, *25*, 171-204.

[130] Chirico, G.; Langowski, J. Biophys.J. 1996, 71(2), 955-971

[131] Kasicka, V., *J. Sep Sci*., 2010, *33*, 2383-2384.

[132] Pei, H., Allison, S.A., *J. Chromatogr. A* 2009, *1216*, 1908-1916.

[133] Allison, S.A., Perrin, C., Cottet, H., *Electrophorsis*, 2011, 32(20), 2788-96.

[134] Fixman, M., *J. Chem. Phys.* 1979, *70*, 4995-5005.

[135] LeBret, M., Zimm, B.H., *Biopolymers* 1984, *23*, 270-285.

[136] Murthy, C.S., Bacquet, R.J., Rossky, P.J., *J. Phys. Chem.* 1985, *89*, 701-710.

[137] Jayaram, B., Sharp, K.A., Honig, B., *Biopolymers*, 1989, *28*, 975-993.

[138] Holst, M.J., Saied, F., *J. Comput. Chem.* 1995, *16*, 337-364.

[139] Baker, N.A., Sept, D., Simpson, J., Holst, M.J., McCammon, J.A., *Proc. Natl. Acad. Sci. USA* 2001, *98*, 10037-10041.

[140] Zhou, H.-X., *J. Chem. Phys.* 1994, *100*, 3152-3162.

[141] Allison, S.A., *J. Phys. Chem. B* 2011, *115*, 4872-4879.

[142] Germann, M.W., Turner, T., Allison, S.A., *J. Phys. Chem. B* 2007, *111*, 1452-1455.

[143] Allison, S.A., Pei, H., in *Progress in Nanoparticles Research*, C.T. Frisiras, Ed., Nova Science Publishers, Inc., New York, N.Y., 2008, Chapter 12.

[144] Perrin, D.O., In *Dissociation Constants of Organic Bases in Aqueous Solution*, Butterworths, London, 1965.

[145] Cantor, C.R., Schimmel, P.R. *Biophysical Chemistry: Part III*, W.H. Freeman, San Francisco, 1980, Chapter 15.

[146] Onsager, L., The Theory of Electrolytes. *Phys. Z.* 1926, *26*, 382-392.

[147] Justice, J.-C.; Ebeling, W., Ionic *J. Sol. Chem.* 1979, *8*, 809-833.

[148] Allison, S.A.; Wu, H.; Twahir, U.; Pei, H., *J. Coll. Interface Sci.* 2010, *352*, 1-10.

[149]: Kroto, H.W.; Heath, J.R.; Obrien, S.C.; Curl, R.F.; Smalley, R.E., C_{60}: Buckminsterfullerene. *Nature* 1985, *318*, 162-163.

[150]: Noon, W.H.; Kong, Y.F.; Ma, J.P., *Proc. Natl. Acad. Sci. USA* 2002, *99*, 6466-6470.

[151]: Zakharian, T.Y.; Seryshev, A.; Sitharaman, B.; Gilbert, B.E.; Knight, V.; Wilson, L. J *J. Am. Chem. Soc.* 2005, *127*, 12508-12509.

[152]: King, R.B., Chemical Structure and Superconductivity. *J. Chem. Inf. Comp. Sci.* 1999, *39*,

180-191.

[153]: Sun, Y.P.; Riggs, J.E.; Liu, B., *Chem. Mater.* 1997, *9,* 1268-1272.

[154]: Haddon, R.C *J. Am. Chem. Soc.* 1997, *119,* 1797-1798.

[155]: Kato, T.; Kikuchi, K.; Achiba, Y., *J. Phys. Chem.* 1993, *97*, 10251-10253.

[156]: Cerar, J.; Cerkovnik, J.; Skerjanc, J., *J. Phys. Chem. B* 1998, *102*, 7377-7381.

[157]: Cerar, J.; Skerjanc, J., *J. Phys. Chem. B* 2000, *104,* 727-730.

[158]: Vrhovsek, A.; Cerar, J.; Bester-Rogac, M.; Skerjanc, J., *Phys. Chem. Chem. Phys.* 2001, *3*, 2650-2654.

[159]: Ma, Y., Zhu, C., Ma, P., Yu, K.T., *J. Chem. Eng. Data* 2005, *50*, 1192-1196.

[160]: Edward, J.T., *J. Chem. Ed.* 1970, *47*, 261-270.

[161]: Cerar, J., Skerjanc, J., *J. Phys. Chem. B* 2008, *112*, 892-895.

[162]: Huizenga, J., Grieger, P., Wall, F., *J. Am. Chem. Soc.* 1950, *72*, 2636-2642.

[163] Kirkwood, J.G., *J. Chem. Phys.* 1934, *2*, 351-360.

[164] Kirkwood, J.G.; Westheimer, F.H., *J. Chem. Phys.* 1938, *6*, 506-512.

[165] Yang, A.-S.; Gunner, M.R.; Sampogna, R.; Sharp, K.; Honig, B., *Proteins* 1993, *15*, 252-265.

[166] Antosiewicz, J.; Briggs, J.M.; Elcock, A.H.; Gilson, M.K.; McCammon, J. A., *J. Comp. Chem.* 1996, *17*, 1633-1644.

[167] Grycuk, J. *J. Phys. Chem. B* 2002, *106*, 1434-1445.

[168] Lee, L.K.; Fitch, C.A.; Garcia-Moreno, B.E., *Protein Sci.* 2002, *11*, 1004-1016.

[169] Allison, S.A.; Xin, Y., *J. Coll. Interface Sci.* 2006, *299*, 977-988.

[170] McQuarrie, D.A. *Statistical Mechanics* Harper and Row, New York 1976, Chapter 15.

[171] Tanford, C. *Physical Chemistry of Macromolecules,* John Wiley, New York 1961, Chapter 7.

[172] Hunter, R.J. *Introduction to Modern Colloid Science,* Oxford University Press, New York 1993, Chapter 7.

[173] Parsons, R. *Handbook of Electrochemical Constants,* Butterworths Scientific Publications, London 1959.

APPENDICES

Appendix A

A) Preliminary Model and Conservancy Relations.

Consider a particle made up of a spherical core of hydrodynamic radius, a, containing an even number of titratable proton sites, n, located a distance, b, from the center of the particle. It shall be assumed that these sites consist of two fundamental types with distinct intrinsic acid dissociation constants, K_1 and K_2. To simplify matters, we shall ignore activity corrections in this work so that these dissociation constants (as well as the cation binding association constant, K_B, discussed later) are practical dissociation/association constants rather than thermodynamic dissociation/association constants. In the case of FHMA, the fullerene core has 6 malonic acid, $C(COOH)_2$ groups attached. K_1 and K_2 would correspond to the intrinsic dissociation constant of the first and second carboxylic acid groups, respectively. There will be a total of n acid dissociation reactions indicated by (j ranges from 0 to n-1)

$$XH'_{n-j} \quad \xleftrightarrow{K_D^{j+1}} \quad XH'_{n-j-1} + H^+ \qquad (A-1)$$

Structurally, multiple species are possible when j or j+1 sites are deprotonated. The primes in Eq. (A-1) indicate specific species. It shall be assumed we start by adding c_x moles of particle per liter of water and let $c = nc_x$ denote the concentration of titratable protons coming from the particle. We then proceed to titrate this solution with concentrated $A(OH)_z$ where A is the cation (of valence charge z). As $A(OH)_z$ is added, the OH^- combines with H^+ from deprotonation of the particle to form water and the pH rises. Define α_N as the moles of added $A(OH)_z$ per liter/(zc) so that the beginning of the titration (no added $A(OH)_z$) corresponds to $\alpha_n = 0$, and $\alpha_n = 1$ corresponds to the case where just enough $A(OH)_z$ has been added to neutralize all

the titratable protons on the particle. In addition to the deprotonation reactions, specific binding of A^{+z} to the particle is also considered.

$$XH_{n-j}A_k^{'} + A^{+z} \quad \xleftrightarrow{K_A^{j,k}} \quad XH_{n-j}A_{k+1}^{'} \qquad (A-2)$$

One again, primes denote a particular species consisting of j well defined deprotonated sites with k or k+1 A^{+z} ions bound to specific sites. Binding of A^{z} shall only be considered to occur to doubly deprotonated groups which occurs when j > n/2.

There are a number of "conservancy relations" that will be useful to identify. The first involves the total concentration of particle species,

$$c_x \quad = \quad \frac{c}{n} \quad = \quad \sum_{j=0}^{n}[XH_{n-j}] + \sum_{j=\frac{n}{2}+1}^{n}\sum_{k=1}^{j-\frac{n}{2}}[XH_{n-j}A_k] \qquad (A-3)$$

The concentrations denoted by brackets in Eq. ($A-3$) represent all species containing j deprotonated sites ($[XH_{n-j}]$) or j deprotonated sites and k bound A^{+z} ions ($[XH_{n-j}A_k]$). The second concerns the amount of added $A(OH)_z$ and the distribution of A between free ions and bound complexes.

$$c\,\alpha_n \quad = \quad z[A^{+z}] + \sum_{j=\frac{n}{2}+1}^{n}\sum_{k=1}^{j-\frac{n}{2}} z\,k\,[XH_{n-j}A_k] \qquad (A-4)$$

The third involves charge neutrality

$$z[A^{+z}] + [H^{+}] \quad = \quad [OH^{-}] + \sum_{j=1}^{n} j[XH_{n-j}] + \sum_{j=\frac{n}{2}+1}^{n}\sum_{k=1}^{j-\frac{n}{2}}(j - z\,k)[XH_{n-j}A_k] \qquad (A-5)$$

A fourth relation that will be useful involves the ionic strength, I, in moles/liter,

$$I = \frac{1}{2}\left([H^+]+[OH^-]+z^2[A^{+z}]+\sum_{j=1}^{n} j^2[XH_{n-j}]+\sum_{j=\frac{n}{2}+1}^{n}\sum_{k=1}^{j-\frac{n}{2}}(j-zk)^2[XH_{n-j}A_k] \right) \qquad (A-6)$$

Using Eq. ($A-5$) to eliminate [A^{+z}] from Eqs. ($A-4$) and ($A-6$),

$$\alpha_n = \frac{[OH^-]}{c}-\frac{[H^+]}{c}+\frac{1}{c}\sum_{j=0}^{n}[XH_{n-j}]+\frac{1}{c}\sum_{j=\frac{n}{2}+1}^{n}\sum_{k=1}^{j-\frac{n}{2}} j[XH_{n-j}A_k] \qquad (A-7)$$

$$I = \frac{1}{2}\left\{ (1+z)[OH^-]+(1-z)[H^+]+\sum_{j=0}^{n} j(j+z)[XH_{n-j}]+\sum_{j=\frac{n}{2}+1}^{n}\sum_{k=1}^{j-\frac{n}{2}}(zj-z^2k+(j-zk)^2)[XH_{n-j}A_k] \right\} \qquad (A-8)$$

The concentrations of the various particle species present shall be considered next.

B) Concentrations of particle species.

We shall focus first on the deprotonation reaction defined by Eq. ($A-1$). Under equilibrium or steady state conditions,

$$K_D^{j+1} = \frac{[XH'_{n-j-1}][H^+]}{[XH'_{n-j}]} \qquad (A-9)$$

The dissociation constants, K_D^{j+1}, change with j just as they would for any polyprotic acid and also depend on solvent (assumed to be water in the present work), temperature, as well as the properties of the background electrolyte, BGE. The physical basis for these changes is varied and complex. First of all, there are intrinsic differences in the various protonation sites which accounts, for example, for the pK_A differences between a strong acid such as HCl and a weaker acid such as acetic acid. In the case of FHMA, we have two fundamentally different classes of

protons (n/2 each) characterized by "intrinsic" acid dissociation constants, K_1 and K_2. They correspond to the dissociation constants of malonic acid losing its first and then second protons under "high salt" conditions where electrostatic interactions between neighboring charge sites are effectively screened. These two constants or equivalently their corresponding pK's, pK_1 and pK_2, shall be left as adjustable parameters. As demonstrated later, the titration curve (pH vs α_n) can be used to determine these parameters. Provided the differences in these pK values is sufficiently large (as it is in the case of FHMA), it is safe to assume that the second class sites deprotonate only after all of the first class sites are deprotonated. The second effect concerns the influence of the electrostatic environment of the fluid and BGE in the immediate vicinity of a charge site and how this affects K_D^{j+1}. Consider the case of a particle with a number of identical protons. Although they all have the same intrinsic acid dissociation constant, K_D^{j+1} decreases with increasing j due to the increasing absolute electrostatic potential produced by neighboring deprotonated sites. The composition of the BGE will also enter since at higher ionic strength, I, the electrostatic interactions will be more effectively screened. Theoretical studies of this problem can be traced to the pioneering work of Kirkwood and coworkers [163,164] and continue to this day. In the last 20 years, numerical methods have been developed [44, 165-168] and applied to peptides, proteins, and highly charged latex particles [169]. Let Λ_j^0 denote the average equilibrium electrostatic potential at a proton site given that j sites have already deprotonated and let $y_j = e\Lambda_j^0/k_BT$ denote a corresponding reduced (dimensionless) potential where e is the fundamental charge (1.602×10^{-19} Coul), k_B is the Boltzmann constant, and T is absolute temperature. From studies of metal oxide nanoparticles [9], we can approximate (for our FHMA model particles)

$$K_D^{j+1} \cong K_i e^{+y_i} \qquad (A-10)$$

Above, i = 1 or 2 and K_i is an intrinsic dissociation constant discussed previously. How y_j is determined is discussed in subsection D. A third consideration concerns the number of distinct particle configurations corresponding to a particular degree of deprotonation. If there were n_1 equivalent sites and n_2 of those sites are deprotonated, then the number of distinct configurations is

$$\Omega(n_1, n_2) = \frac{n_1!}{n_2!(n_1 - n_2)!} \qquad (A-11)$$

We shall employ the identical independent site model, IISM [145], at this point and assume the different configurations corresponding to a particular (n_1, n_2) case are present in equal concentration. Also, let [XH_{n-j}] denote concentration of all species with j deprotonated sites irrespective of specific configuration (and [XH_{n-j}'] is the concentration of a specific configuration). Remembering that the first n/2 sites have intrinsic dissociation constant K_1 and the remaining n/2 sites K_2,

$$[XH'_{n-j}] = \begin{cases} \dfrac{\left(\frac{n}{2} - j\right)!\, j!}{\left(\frac{n}{2}\right)!}[XH_{n-j}] & j \le \dfrac{n}{2} \qquad (A-12a) \\ \dfrac{(n-j)!\left(j - \frac{n}{2}\right)!}{\left(\frac{n}{2}\right)!}[XH_{n-j}] & \dfrac{n}{2} < j \le n \qquad (A-12b) \end{cases}$$

Using Eqs. ($A-10$) and ($A-12$) in ($A-9$)

$$[XH_{n-j-1}] = P_n^j [XH_{n-j}] \qquad (A-13)$$

$$P_n^j = \begin{cases} \dfrac{\left(\dfrac{n}{2}-j\right)}{(j+1)}\dfrac{K_1 e^{y_j}}{[H^+]} & j<\dfrac{n}{2} \qquad (A-14a) \\ \dfrac{(n-j)}{\left(j+1-\dfrac{n}{2}\right)}\dfrac{K_2 e^{y_j}}{[H^+]} & \dfrac{n}{2}\le j<n \qquad (A-14b) \end{cases}$$

Applying Eq. (A-13) recursively, we can write

$$[XH_{n-j-1}] = [XH_n]T_n^j \qquad (A-15a)$$

$$T_n^j = \prod_{k=0}^{j} P_n^{j-k} \qquad (A-15b)$$

Similar arguments applied above to the deprotonation reactions can be applied to the binding of A^{+z} counterions to the particle. Following arguments similar to those leading up to Eq. (A-10), we define an intrinsic cation binding constant, K_B. Following Eq. ($A-2$), we can write

$$K_A^{j,k} = \frac{[XH_{n-j}A'_{k+1}]}{[XH_{n-j}A'_k][A^{+z}]} = K_B e^{z y_{j-zk}} \qquad (A-16)$$

The quantity, $y_{j\text{-}zk}$, denotes the average reduced electrostatic potential at the charge sites (at r = b) for a particle with j sites deprotonated and k bound cations. (See discussion preceding Eq. ($A-10$).) In the present work, we shall only consider binding to the final n/2 doubly deprotonated malonic acid sites. This strategy would be straightforward to modify if necessary. As in the case of the deprotonation reactions, configuration issues must be addressed in addition electrostatics. It is straightforward to show

$$[XH_{n-j}A_k] = [XH_n]T_n^{j-1}T_{Bn}^{j,k} \qquad (A-17)$$

$$T_{Bn}^{j,k} = \prod_{m=1}^{k} P_{Bn}^{j,m} \qquad (A-18a)$$

$$P_{Bn}^{j.m} = \left(\frac{j+1-m-\frac{n}{2}}{m} \right) K_B [A^{+z}] e^{-z\, y_{j-zk}} \qquad (A-18b)$$

Now using Eqs. ($A-15$a) and ($A-17$) in the conservancy relations defined by Eqs. ($A-3$), ($A-7$), and ($A-8$); it can be shown

$$[XH_n] = \frac{c}{n(1+H_{0n})} \qquad (A-19)$$

$$\alpha_n = \frac{[OH^-]}{c} - \frac{[H^+]}{c} + \frac{H_{1n}}{n(1+H_{0n})} \qquad (A-20)$$

$$I = \frac{1}{2}\left\{ (1+z)[OH^-] + (1-z)[H^+] + \frac{c\,(zH_{1n} + H_{2n})}{n(1+H_{0n})} \right\} \qquad (A-21)$$

$$H_{0n} = \sum_{j=0}^{n-1} T_n^{\,j} + \sum_{j=\frac{n}{2}+1}^{n} \sum_{k=1}^{j-\frac{n}{2}} T_n^{\,j-1} T_{Bn}^{\,j,k} \qquad (A-22)$$

$$H_{1n} = \sum_{j=1}^{n} j T_n^{\,j-1} + \sum_{j=\frac{n}{2}+1}^{n} \sum_{k=1}^{j-\frac{n}{2}} j T_n^{\,j-1} T_{Bn}^{\,j,k} \qquad (A-23)$$

$$H_{2n} = \sum_{j=1}^{n} j^2 T_n^{\,j-1} + \sum_{j=\frac{n}{2}+1}^{n} \sum_{k=1}^{j-\frac{n}{2}} [(j-zk)^2 - k\,z^2] T_n^{\,j-1} T_{Bn}^{\,j,k} \qquad (A-24)$$

The fundamental strategy being followed here is that given a comparatively small number of input parameters that are either known in advance or can be determined by fitting to

experimental data, it is possible, subject to the limitations of the model, to determine the concentrations of all species present along with α_n and I. Before this is possible, however, it is necessary to determine the reduced electrostatic potentials appearing in Eqs. ($A-14$) and ($A-18$b). This shall be discussed next.

C) Poisson-Boltzmann equation and algorithm to determine particle concentrations.

The coarse-grained electrostatics are solved using the continuum primitive model [170]. Figure A-1 illustrates the principle features of our model particle. The hydrodynamic radius, a, separates the particle interior from the fluid. The relative permittivities of the particle interior (r < a) and exterior (r > a) are assumed to equal ε_i and ε_r, respectively. The particle charge is assumed to be uniformly distributed in a thin shell of radius b ($2a > b \geq a$) and this fixed charge density shall be denoted σ (in Coul/m^2). The assumption is made that small ions (H^+, OH^-, and A^{+z}) can approach the particle to within a distance of a, but other FHMA articles of variable charge can only approach within a distance 2a. It is convenient to define three zones: I (r < a), II (a < r < 2a) and III (r > 2a). It is assumed that the charge distribution around the central particle is centrosymmetric.

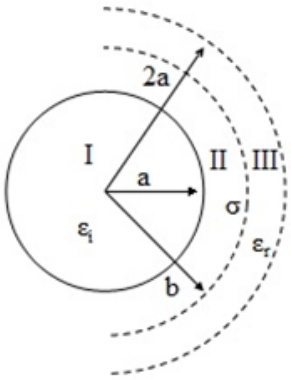

Figure 1) FHMA Continuum Model.

For zones II and III, the Poisson equation can be written

$$\frac{1}{r^2}\frac{d}{dr}\left(r^2\frac{d\,y(r)}{dr}\right) = -\frac{e}{\varepsilon_0\varepsilon_r k_B T}\left[\rho_f(r)+\rho_m(r)\right] \qquad (A-24)$$

Above, y(r) is the reduced electrostatic potential (see definition preceding Eq. (A-10)), ε_0 is the permittivity of free space, ρ_f is the fixed charge density, ρ_m is the (local) mobile ion charge density, and other quantities have been previously defined. It shall be assumed that the mobile ions are distributed as point ions according to the Boltzmann distribution (r > a)

$$\rho_m(r) = F\left\{[H^+]e^{-y(r)}-[OH^-]e^{y(r)}+[A^{+z}]e^{-zy(r)}-\Phi(r)S(r)\right\} \qquad (A-25a)$$

$$S(r) = \sum_{j=1}^{n} j[XH_{n-j}]e^{jy(r)} + \sum_{j=\frac{n}{2}+1}^{n}\sum_{k=1}^{j-\frac{n}{2}}(j-zk)[XH_{n-j}A_k]e^{(j-zk)y(r)} \qquad (A-25b)$$

Above, F is the Faraday constant and Φ(r) is equal to 0 for r < 2a and 1 for r > 2a. The quantity S(r) denotes the contribution of charged FHMA species to the mobile ion atmosphere of the central particle. The concentrations of the various charged species can be reduced further using Eqs. ($A-15$a), ($A-17$), and ($A-19$).

The fixed charge density is dealt with as an electrostatic boundary condition (b^- and b^+ correspond to radial distances slightly smaller and greater that r = b, respectively) [171]

$$\left(\frac{dy}{dr}\right)_{b^+}-\left(\frac{dy}{dr}\right)_{b^-} = -\frac{\sigma e}{\varepsilon_0\varepsilon_r k_B T} \qquad (A-26)$$

The reduced potential is continuous at r=b, but the first derivative is discontinuous. Since there is no charge within the core of the particle, an additional boundary condition is

$$\left(\frac{\partial y}{\partial r}\right)_a = 0 \qquad (A-27)$$

At this point, introduce the reduced length variable

$$x = \frac{1}{\kappa r} \qquad (A-28a)$$

$$\kappa = B\sqrt{I} \qquad (A-28b)$$

$$B = \sqrt{\frac{2Fe}{\varepsilon_0 \varepsilon_r k_B T}} \qquad (A-28c)$$

Above, κ is the Debye-Huckel screening parameter (I is the ionic strength (Eq. ($A-21$)). In terms of the reduced length variable x, Eqs. (A-24), ($A-26$), and ($A-27$) can be written

$$\frac{d^2 y}{dx^2} = -\frac{\rho_m(x)}{2FIx^4} \qquad (A-29a)$$

$$\left(\frac{dy}{dx}\right)_{x=1/\kappa b^+} = \left(\frac{dy}{dx}\right)_{x=1/\kappa b^-} + \frac{\sigma b^2 \kappa}{\varepsilon_0 \varepsilon_r k_B T} \qquad (A-29b)$$

$$\left(\frac{dy}{dx}\right)_{x=1/\kappa a} = 0 \qquad (A-29c)$$

Analytical solutions of the non-linear Poisson Boltzmann, PB, equation are available for only a very limited number of model geometries (172) and these do not include a spherical particle of arbitrary radius with a centro-symmetric charge distribution. However, numerical algorithms for this problem have been available for over 50 years [82], and its solution is now

routine. At large r or small x, Eq. ($A-29$a) reduces to the linear PB equation which does have a known analytical solution [171]. An initial choice of y(x) is made at small (x) and then Eq.(29a) (with Eq.($A-29$b) at the appropriate x-value) is solved numerically. If Eq. ($A-29$c) is not satisfied, the form of y(x) (small x) is adjusted and the process is repeated until it is satisfied to within a prespecified tolerance level.

There is one serious problem with this procedure. In order to carry out the numerical solution of Eqs. ($A-29$a-c), it is necessary to know the mobile ion densities (Eq. ($A-25$)), but this requires knowledge of the ion concentrations (Eqs. ($A-15$a), ($A-17$), and ($A-19$)), but these, in turn, require knowledge of y(r) which is what we are trying to determine. Furthermore, we need to know y at r=b for the various charge states of the particle. For FHMA, the valence charge can vary from -1 to -12. To deal with this difficulty, y_j in Eqs. ($A-14$) and $y_{j\text{-}zk}$ in Eq. ($A-18$b) are initially set to zero and these are then used to compute approximate $\{T_n^j\}$, $\{T_{Bn}^{j,k}\}$, H_{0n}, H_{1n}, H_{2n}, and $\rho_m(r)$ values. These approximate values are then used to compute revised $\{y_j\}$ values. Once we have these, the cycle is repeated until the set, $\{y_j\}$, converges. This is normally achieved in 4 to 6 iterations.

At this stage, we have equilibrium electrostatic potentials and concentrations of all of the charged species present. The procedure followed in this work is to define an initial particle concentration, temperature, titrating counterion, and pH. Then, we numerically solve the non linear PB equation by the method described above. In the process, we also determine the concentration of all species as well as I and α_n (Eq. ($A-20$)). By including an outer loop in the program over different pH values, it is straightforward to determine the titration curve (pH versus α_n) for the model particle subject to a specific set of input parameters (a, b, T, c_X, pK_1,

pK_2, pK_B, and several others). Transport properties such as electrophoretic mobilities and conductances can then be calculated. This shall be discussed next.

D) Electrophoretic mobility and conductance of complex aqueous solutions.

The conductance of aqueous solutions made up of small ions has received considerable attention for almost one hundred years [12,14,15, 42-45,53,54,131-135]. This "small ion" theory is in excellent agreement with experiment although most studies have been confined to binary electrolytes, and a single "ion exclusion radius" is left as an adjustable parameter in modeling. Also, it is appropriate for small ions, and not for large, highly charged ions [136]. Furthermore, the electrostatics are treated at the level of the linear PB equation which limits it to weakly charged particles. For "large ions", that can also bear arbitrary charges, it is important to account in more detail for the finite particle size as well as treat the electrostatics at the level of the non linear Poisson Boltzmann equation. For this purpose, the method of O'Brien and White [30] is appropriate to first calculate electrophoretic mobilities. Once these are determined, it is straightforward to determine the electrical conductivity [136]

For a complex suspension of ions, the electrical conductivity, κ (in 1/(ohm m)) can be written (ref. [14] of main manuscript)

$$\kappa = \kappa' + \kappa'' = 1000F\sum_{\alpha=1}^{3} c_\alpha z_\alpha \mu_\alpha + 1000F\sum_{\alpha>3} c_\alpha z_\alpha \mu_\alpha \qquad (A-30)$$

Above, F is the Faraday (96,485 Coul/mole) the sum extends over all ions present in solution, c_α denotes the molar concentration (M = moles/liter) of ion α, z_α is its valence charge, and μ_α is its electrophoretic mobility (in $m^2/(V\ sec) = m^2/(Coul\ ohm)$). The factor of 1000 converts moles/liter to moles/m^3. We shall follow the convention of labeling the small ions, H^+,

OH^-, and A^{+z} as ions 1 through 3, respectively, and the large ions due to deprotonation of FHMA as ions, 4, 5, etc.. This explains why Eq. ($A-30$) is subdivided into sums over small ions, κ', and large ions, κ''. For the large ions, the O'brien-White procedure is used to compute mobilities.

For the small ions, the mobilities are calculated using Eqs. ($A-33$- $A-35$) of reference [133] that, in turn, has its origins in Onsager-Fuoss theory [6]. The small ion mobility is written

$$\mu_\alpha = (1-B_1 S_\alpha \sqrt{I})\left(\mu_{\alpha 0} - \frac{B_2 z_\alpha \sqrt{I}}{1+B A_\alpha \sqrt{I}}\right) \qquad (A-31)$$

$$B_1\ (in\ M^{-1/2}) = \frac{\sqrt{2}F^3}{12\pi N_{Av}(\varepsilon_0\varepsilon_r RT)^{3/2}} = \frac{2.806\,x10^6}{(\varepsilon_r T)^{3/2}} \qquad (A-32a)$$

$$B_2\ (in\ \frac{m^2}{V\sec M^{1/2}}) = \frac{\sqrt{2}F^2}{6\pi\eta N_{Av}(\varepsilon_0\varepsilon_r RT)^{1/2}} = \frac{4.275\,x10^{-6}}{\eta(\varepsilon_r T)^{1/2}} \qquad (A-32b)$$

$$B\left(in\ \frac{1}{nm\ M^{1/2}}\right) = \frac{\sqrt{2}F}{\sqrt{\varepsilon_0\varepsilon_r RT}} = \frac{502.8}{\sqrt{\varepsilon_r T}} \qquad (A-32c)$$

$$|\mu_{\alpha 0}|(in\ \frac{m^2}{V\sec} = \frac{m^2}{Coul\ ohm}) = \frac{\Lambda_{\alpha 0}}{F} \qquad (A-32d)$$

The physical basis of the first term on the right hand side of Eq. ($A-31$) (containing S_α) is the ion relaxation effect. The S_α term shall be discussed later. The mobility of ion α in the limit of zero ionic strength, μ_α, is related to the equivalent ionic conductance in the limit of zero ionic strength, $\Lambda_{\alpha 0}$, by Eq. ($A-32$d). These are tabulated in handbooks [137, 138] for many

common ions. The quantity η appearing in Eq. ($A-32b$) is the solvent viscosity and for the right hand side to be valid, η should be in centipoise. The quantities, A_α, can be thought of as an "ion exclusion radii" and have units of length. In the present work they are determined from the concentration dependence of the equivalent conductances of simple binary electrolyte of two ions of valence z_+ and z_-

$$\Lambda = F(|\mu_+| + |\mu_-|) = (1 - B_1 S\sqrt{I})\left(\Lambda_0 - B_3\sqrt{I}\left(\frac{|z_+|}{1+BA_+\sqrt{I}} + \frac{|z_-|}{1+BA_-\sqrt{I}}\right)\right) \qquad (A-33)$$

$$\Lambda_0 = \Lambda_{+0} + \Lambda_{-0} \qquad (A-34a)$$

$$B_3 = F B_2 \qquad (A-34b)$$

$$S = \frac{|z_+||z_-|q}{1+\sqrt{q}} \qquad (A-34c)$$

$$q = \frac{|z_+ z_-|}{|z_+| + |z_-|}\left(\frac{\Lambda_{+0} + \Lambda_{-0}}{|z_-|\Lambda_{+0} + |z_+|\Lambda_{-0}}\right) \qquad (A-34d)$$

For a simple binary electrolyte, the relaxation term, $S_{\pm}$, is identical for both + and – ions and the subscript is dropped. It is given by Eqs. ($A-34c$) and ($A-34d$) [131, 136]. Expanding Eq. ($A-33$) in powers of $\sqrt{I}$ and retaining terms to order I,

$$\Lambda = \Lambda_0(1 - C_1\sqrt{I} + C_2 I) \qquad (A-35)$$

$$C_1 = \frac{B_3}{\Lambda_0}(|z_+| + |z_-|) + B_1 S \qquad (A-36a)$$

$$C_2 = \frac{B_3}{\Lambda_0}\left[B\left(|z_+|A_+ + |z_-|A_-\right) + B_1 S\left(|z_+| + |z_-|\right)\right] \qquad (A-36b)$$

Extensive tables of Λ versus concentration derived from experiment, along with fitting polynomials of the form given by Eq. ($A-35$), are available in the literature [137]. (In reference 137, Table 76 gives these coefficients. However, the concentration they employ, c, equals $2I/(|z_+|+|z_-|)$.) Ion exclusion radii, $A_{\pm}$, are the only unknowns in Eq. ($A-36b$) and can be extracted from the coefficient corresponding to C_2. One problem with this approach is that Eq. ($A-36b$) contains two unknowns, A_+ and A_-. We handle this by assuming A_+ is equal to A_- for KCl and the physical basis of this assumption is that the limiting molar conductivities, $\Lambda_{\pm 0}$, (and hence their hydrodynamic radii) are about the same for K^+ and Cl^-. From the C_2 coefficient for KCl, we determine A_{K^+} and A_{Cl^-}. Then from the C_2 of HCl, we can determine A_{H^+}, etc. The results of this procedure are: $A_{K^+} = A_{Cl^-} = 0.412$ nm, $A_{H^+} = 1.075$ nm, $A_{OH^-} = 0.539$ nm, $A_{Na^+} = 0.388$, and $A_{Ca^{+2}} = 0.428$ nm. It should be emphasized that these radii should not be equated to hydrodynamic radii, but rather as effective radii that yield good empirical fits to Eqs. ($A-35$) and ($A-36$).

In calculating κ' in FHMA modeling using Eq. ($A-30$), Eq. ($A-31$) can now be used to calculate μ_α. However, since the solution is no longer a binary electrolyte, the relaxation correction term, S_α, is more complicated than given be Eq. ($A-34c$). In this case, a straightforward iterative solution is employed following the procedure of Onsager and Fuoss [6]. We write

$$S_\alpha = z_\alpha \sum_{m=0}^{\infty} d_m r_\alpha^m \qquad (A-37)$$

Above, the coefficients d_m and r_α^m have been defined in earlier publications [131, 136] By this procedure, the relaxation correction, which is small for weakly charged ions, is approximated using the original "point ion" theory of Onsager and Fuoss [6]. Although this is expected to work well for small ions, it does not work well for large and/or highly charged ions.

FHMA is modeled as a low dielectric sphere with hydrodynamic radius equal to a. Solvent as well as "small" ions (H^+, OH^-, and A^{+z}) can approach the particle within a distance greater than or equal to a. The relative permittivity is ε_i for $r < a$ and ε_r for $r > a$. The fixed particle charge is assumed to be uniformly distributed on a spherical surface of radius b ($b \geq a$) and let σ denote the valence charge/area. Other FHMA ions can contribute to the ionic shielding of the central particle, but can only approach the central particle to within a distance 2a. It is convenient to break space up into zones I ($r < a$), II ($a<r<2a$), and III ($2a<r$).